Computational Elucidation of Molecular Scale Water Within Polymer Hydrates

by

Dominick Filonowich

Bachelor of Science in Chemical Engineering, The New Mexico Institute of Science and

Technology, 2020

Submitted to the Graduate Faculty of

the Swanson School of Engineering in partial fulfillment

of the requirements for the degree of

Master of Science

University of Pittsburgh

2022

UNIVERSITY OF PITTSBURGH

SWANSON SCHOOL OF ENGINEERING

This thesis was presented

by

Dominick Filonowich

It was defended on

July 15th 2022

and approved by

Chris E. Wilmer, Department of Chemical Engineering

Thesis Advisor: Sachin Velankar, Department of Chemical Engineering

Thesis Advisor: John Keith, Department of Chemical Engineering

Computational Elucidation of Molecular Scale Water Within Polymer Hydrates

Dominick Filonowich, M.S.

University of Pittsburgh, 2022

Four polymer hydrates were investigated using multiple computational techniques, including molecular dynamics, geometry optimizations using the Kohn-Sham density functional theory Perdew–Burke-Ernzerhof (DFT PBE) exchange correlation functional, and the Local Energy Decomposition (LED) method of Neese and Bistoni. Molecular dynamics simulations on an infinitely large hydrate using universal classical forcefields did not melt, and a prototype python script to create finitely sized hydrates was developed. LED calculations quantified the degree that these polymer hydrates are formed due to electrostatic and exchange interactions between polymers chains and water molecules. In all cases, exchange interactions were approximately 1/5 the size of the electrostatic interactions, which is possible descriptor for hydrates of this type. New hypothetical hydrates were also modeled by doping oxygen into or fluoridating the PEI hemi and sesquihydrates. By calculating the binding energies of these structures, it was found that as the total binding energy decreases, the melting temperature increases. This analysis also suggested the fluoridated hydrates have may significantly weaker cohesive energies relative to that of the original hydrates, and if these structures are experimentally stable this suggests a viable means to design new hydrates for ion capture.

Table of Contents

List of Tables

List of Figures

Preface

I'd like to thank my advisors, my friends, and my family for all their support and understanding they've provided me whilst I was working on this project.

1.0   Water, Clathrates, and Polymer Hydrates

1.1   Behavior of Water

Water is one of the most important substances in the known universe. It makes up a majority of our planet's surface, and approximately 70% of our own bodies. The overall importance and abundance of water has spurred interest in its behaviors and crystalline structures.

1.1.1   Liquid Water

In its liquid form, water deviates strongly from that of a simple liquid. For instance, only a few liquids (e.g., Gallium melts) have a maximum liquid-phase density. Water is included amongst these liquids, reaching its maximum density of $0.999972 \frac{g}{cm^3}$ at 277K. Continued cooling down to the freezing point of 273K actually causes the density to decrease. This is because as water freezes it expands by about 11%, as opposed to most liquids that become increasingly dense as they solidify[1].

Other anomalous properties include the heat capacity at constant pressure (C_P). Supercooling causes the C_P to rapidly increase, leading water to take more heat to raise the temperature than other substances of the same volume. The behavior of the diffusion constant D is also reversed in liquid water than that of other simple liquids. As pressure increases at constant temperature, D increases in water rather than decreases, and peaks at about 200 MPa before decreasing again. Viscosity deviates in its own way, decreasing as temperature increases at a constant pressure, and does so in a non-linear fashion. This suggests that the activation energy (Ea) for molecular motion increases as temperature decreases. However, when water at 273K is pressurized, it becomes more fluid rather than viscous, which is anomalous in its own right[2].

1.1.2 Ice

At the time of writing, there are 22 crystalline forms of ice, including I_h (h = hexagonal), I_c (c = cubic), I_{sd} (sd = stacking disordered), and ice II - XX. The search for more ice structures continues, which is a testament to the structural versatility of water molecules. However, relative to I_h, these structures occur at lower temperatures and/or higher pressure.

Within I_h itself, the oxygen atoms almost form a tetrahedral structure, and each molecule had four hydrogen bonds with a length of 2.74$\mathring{A}$. The hydrogen bonding also lengthens the R(O-H) bond to 1.01$\mathring{A}$ from 0.9572$\mathring{A}$. The (H-O-H) bond angle also widens from 104.5° to the standard 109.5° of a tetrahedral structure [3].

1.2 Clathrate Hydrates

Due to these hydrogen bonds, water builds a network around nonpolar solutes. This makes room for a guest atom, surrounded by a cage-like structure of water. The water molecules move to strengthen this cage by aligning with three tetrahedral directions tangential to the surface, preserving the maximum number of possible hydrogen bonds, as can be seen in Figure 1. This form ice-like structures, which are only really stable in the presence of a guest molecule[4].

1.2.1 A Brief History of Clathrate Hydrates

Crystalline hydrates in the presence of chlorine gas were first discovered in 1823 by Davy and Faraday, but the actual crystalline structures weren't actually determined until 1952 by Pauling and Marsh[4]. The water molecules would generally from cage Type-I, Type-II, or Type-H clathrate structures, with the typing being determined by the size of the guest molecule, which then stabilizes the cages through repulsive interactions [5].

These clathrate structures primarily form in permafrost, marine environments. Ideal
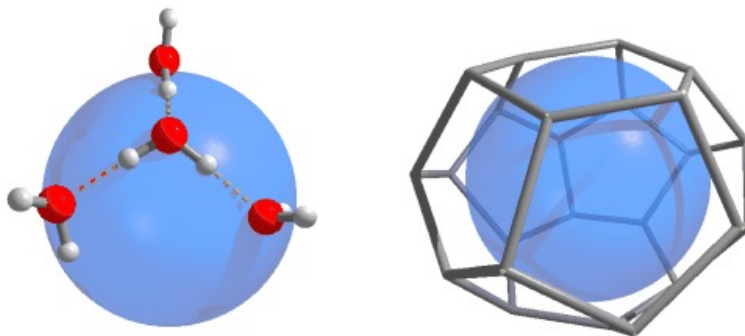
Figure 1: Each water molecule prefers to place its tetrahedral bonding directions in a straddling mode (left). A possible H-bonded network is shown for a clathrate hydrate (right)[2]. Reprinted with permission from Ludwig, R. Angewandte Chemie International Edition 2001, 40, 1808–1827.

conditions for the formation of these structures occur at depths between 500 and 2000 meters, where the surface temperature of the water is no more than $2°C$. The clathrates tend to form around natural gas deposits under these conditions, but much deeper and the temperature will raise too high for formation, and to near the surface the pressure won't be high enough for formation. It should be noted that Type-H clathrates are very rarely found in nature due to their complexity, and therefore, the majority of the clathrates forming in these environments are Type-I or II[6].

Type-I structures consist of 46 water molecules with two small and six large cavities. The smaller cavities are dodecahedral cages with pentagonal faces. The large cavities have 12 pentagonal faces, and two hexagonal faces[6]. Type-II structures consist of 136 water molecules in a unit cell of 16 small and eight large cavities. The small cavities are the same as their Type-I counterparts, while the large cavities have 12 pentagonal faces, and four hexagonal faces[7]. Type-H cages feature three small, two medium, and one large cavity. The small cavities were once again the same as their counterparts, the medium cavities has three tetragonal faces, six pentagonal faces, and three hexagonal faces, while the large cavity

3

has 12 pentagonal face and eight hexagonal faces [8]. These cages are visualized in Figure 2
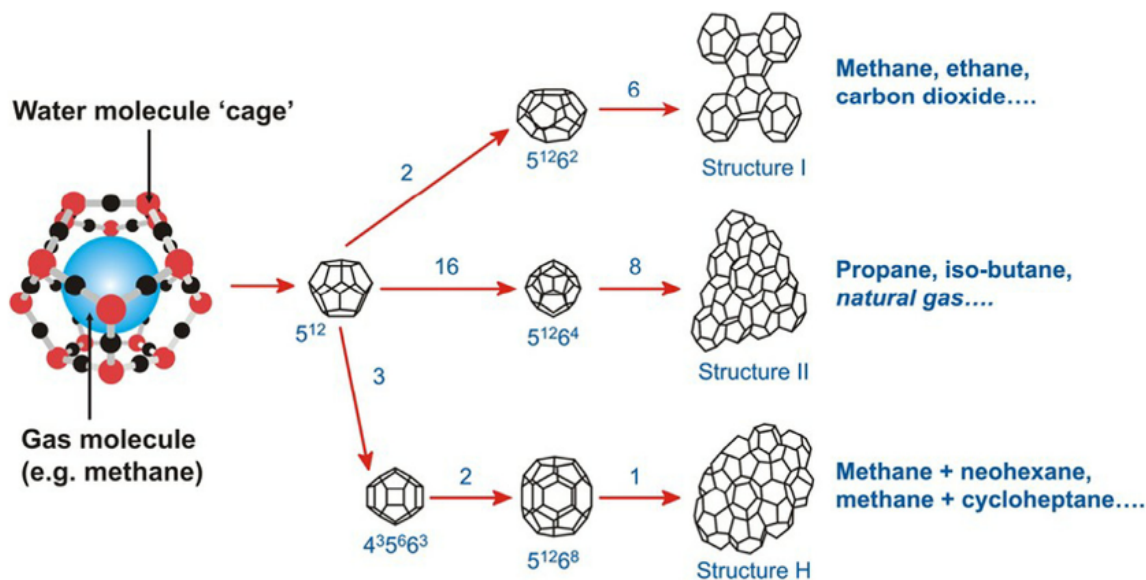
Figure 2: Crystal structure of clathrate hydrate cages[6]. The numbers on the arrows correspond to the number of cavities, starting at the smallest cavity and progressing to the largest. The numbers beneath the structure indicate the number of faces, where $5^{12}6^2$ reads as 12 pentagonal faces and 2 hexagonal faces. Figure is resued with permission from Das, S.; Tadepalli, K. M.; Roy, S.; Kumar, R. A review of clathrate hydrate nucleation, growth and decomposition studied using molecular dynamics simulation. Journal of Molecular Liquids 2022, 348, 118025.

1.2.2 Molecular Clathrates

A large contingent of the available cavities in clathrates are too small to hold large molecules. Only the Type-II and Type-H structures have a cavity large enough for some larger hydrocarbons such as propane. This means most clathrates seem to house low molecular weight gas, such as methane[6]. Multiple occupancy of these cages is also possible for smaller guest molecules in the larger cages, which has been onserved by diffraction for H_2[9],

$He[10]$, $Ne[7]$, $CO[11]$, $N_2[12]$, and $O_2[12]$.

Methane clathrate hydrates are the most extensively studied, most likely due to how common methane clathrates are in nature; in 2011, Boswell and Collett[13] estimated that there is $3*10^{15}m^3$ of methane gas trapped in clathrates across the globe, while Kvenolden[14] estimates more than half of the carbon on the globe is sequestered in clathrates. Studies have focused on methane to discover the mechanism of clathrate formation, and in 2007, Guo et al[15] proposed that the presence of methane molecules increase the relaxation time of water molecules and slow them down. This allows ample time for the hydrogen bonding to arrange the molecules into Type-I structures, which is the primary structure for the majority of methane clathrates[16]. This mechanism has since been supported by molecular dynamics (MD) simulations[6].

1.2.3 Research and Applications of Clathrates

The large amount of methane trapped in clathrate hydrates has sparked many studies in the phenomena. Some researchers suggest caution, studying the possible impact of these clathrates on global climate change. For instance, in 2017 Ruppel et al[17] suggested that if 0.1% of the estimated methane was released due to the clathrates melting, it would raise the amount of methane in the atmosphere by up to 60%, which would be catastrophic according to Bohannon[18], MacDonald[19], and Whiteman[20]. To prevent this, some groups have suggested reinforcing methane sediments by injecting them with chemical promoters, to prevent the hydrates from melting as temperatures increase[21][22].

Other work has focused on clathrates as a method of energy storage. In 1974, Davidson et al[23] estimated that the same volume of methane clathrate hydrates would contain 164 times more methane than the same volume of pure gaseous methane. Clathrates are already being used for temporary storage and transportation of methane, and work is being done using chemical promoters to increase the volume of trapped gas[24].

Marine sequestration of CO_2 has also been theorized. The idea is that, if CO_2 emissions are released deep into the oceans, rather than into the atmosphere, the gas would be trapped in clathrate sediments. For instance, injecting the CO_2 at depths of around 400 meters causes is ideal for clathrate formation, but other depths can also form clathrate hydrates in the right conditions[25]. Injecting the gas at depths between 500 and 900 meters can also form clathrates in CO_2 rich water[26], and the increased pressure and lower temperatures further stabilize the structures[22]. At depths between 1000 and 2000 meters, liquid CO_2 diffuses and disolves into the ocean as well[27], meaning meaning clathrates at appropriate depths and allowing them to sink can also be very beneficial[28]. This is also directly beneficial for other environmental reasons, as some work suggests methane clathrates are further stabilized by the presence of CO_2 clathrates[21][22][29].

1.3   Polyoxacyclobutane (POCB)

1.3.1   POCB as a Polymer

A different class of clathrate falls into that of polymer hydrates. Initially discovered in 1958 by Bunn and Holmes[30], POCB was further characterized in 1967 by Tadokoro[31]. With the base of a polyether, POCB's monomer unit can be seen in Figure 3.
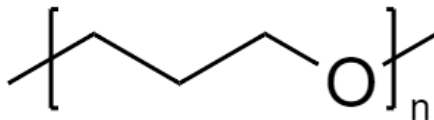
Figure 3: Chemical structure of a linear POCB monomer unit

In Tadokoro's work, it was found that POCB has three crystal modifications of differing characteristics[32]. These modifications are achieved by different treatment methods of the polymer, which can be seen in Figure 4.
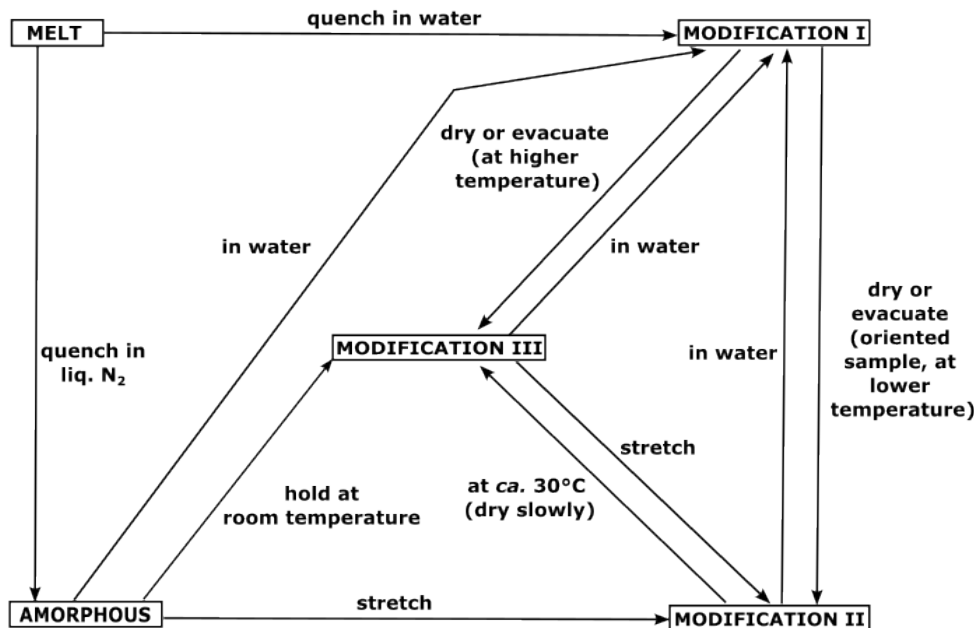
Figure 4: Methods of treatment of the polymer to form the three different modifications of POCB. Adapted from Tadokoro, H. Structure of crystalline polyethers. Journal of Polymer Science: Macromolecular Reviews 1967, 1, 119–172,
eprint: https://onlinelibrary.wiley.com/doi/pdf/10.1002/pol.1967.230010105.

Modification I is in a planar zigzag conformation, over a fiber identity period of 4.80Å. The cell contains four polymer chains and four water molecules, and is a polymer hydrate structure[32]. The crystal structure of Modification I can be seen in Figure 5. Modification I will be discussed in more detail in the next subsection.

Modification II has a fiber identity period of 8.41Å. It also has a trigonal lattice with a space group of $R3c - C_{3v}^6$ and a unit cell $a = 14.13\text{Å}$ and $c = 8.41\text{Å}$, which contains nine molecular chains. Unlike Modification I, these chains are more helical, with some chains forming a screw to the right, and others to the left[32]. The crystal structure of Modification
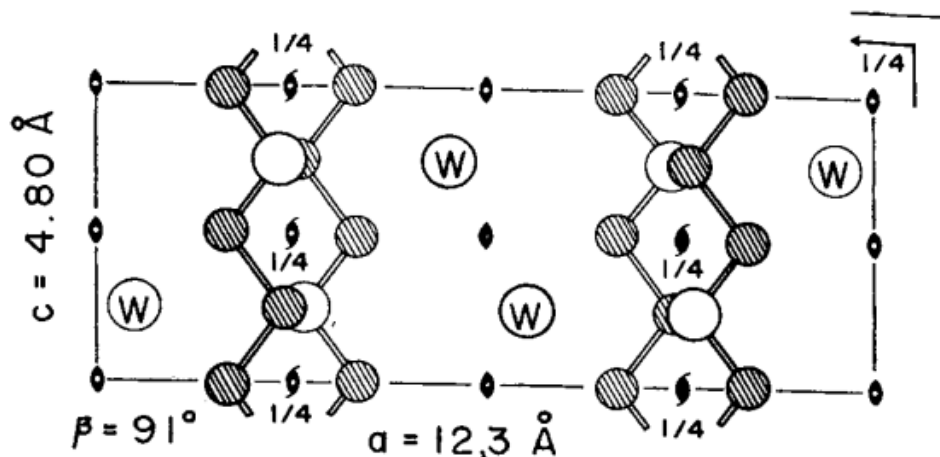
Figure 5: Crystal structure of Modification I of the POCB crystal structure[32]. Reprinted with permission from Tadokoro, H. Structure of crystalline polyethers. Journal of Polymer Science: Macromolecular Reviews 1967, 1, 119–172,

eprint: https://onlinelibrary.wiley.com/doi/pdf/10.1002/pol.1967.230010105.

II can be seen in Figure 6.

Modification III has an orthorhombic unit cell with dimensions of $a = 9.23\mathring{A}$, $b = 4.82\mathring{A}$, and $c = 7.21\mathring{A}$. It has a helical conformation, and the cell contains four chains. This modification is the most stable of the three, which is primarily due to the strong dipole moments of the COC groups that are oriented in an antiparallel fashion. Two unit cell orientations are possible based on the $C222_1 - D_2^5$ space group. The first is shown in Figure 7; the other has the same molecular axis, but the helical axis is twisted 90° from the first orientation, with no clear indication of which unit cell is more correct[32]. Both crystal structures contain two helical chains that turn at the same angle through the center and corners of the unit cell.

The modifications easily transition between one another. As these transitions occur, the orientation of the structure was more difficult to obtain. This behavior is attributed to different lengths of the fiber axis per monomer unit, with a length of $4.80\mathring{A}$ in I, $4.21\mathring{A}$ in
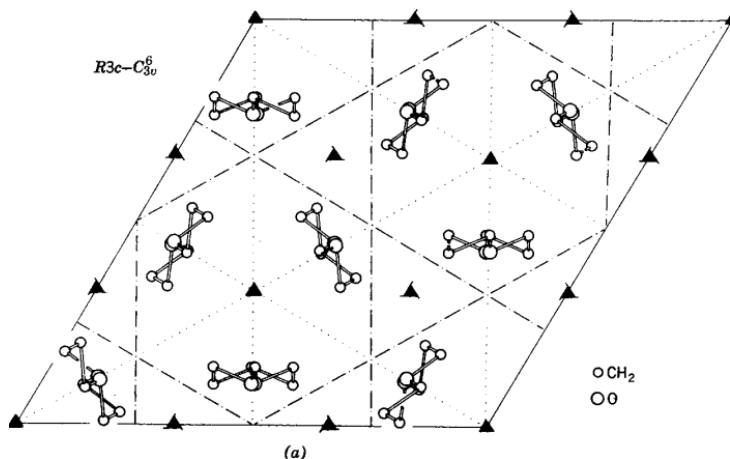
Figure 6: Crystal structure of Modification II of the POCB crystal structure[32]. Reprinted with permission from Tadokoro, H. Structure of crystalline polyethers. Journal of Polymer Science: Macromolecular Reviews 1967, 1, 119–172,

eprint: https://onlinelibrary.wiley.com/doi/pdf/10.1002/pol.1967.230010105.

II, and 3.61Å in III[32]. This may be further explained by further study into the transition mechanism between the three modifications, but this has not been done at this time.

Thermodynamically, Modification III was found to have a glass transition temperature (T_g) of 195K, with a specific heat at constant pressure $\Delta(C_p)$ of 0.895 $\frac{J}{gK}$. The sample began to crystallize at 204K, and melts at 305K[33]. These results leave POCB be the lowest melting point, lowest enthalpy of melting, and lowest random chain size of polymers in the polyoxyalkene series[34].

1.3.2 POCB as a Polymer Hydrate

As previously discussed, Modification I is a POCB hydrate. This structure was analyzed via infrared and x-ray methods. X-ray analysis showed that the distances between oxygen atoms (water-water: 2.68Å, water-polymer:2.70Å) are shorter than twice the van der Waals radius of an oxygen atom (2.80Å). This suggests that there are hydrogen bonds not just

9
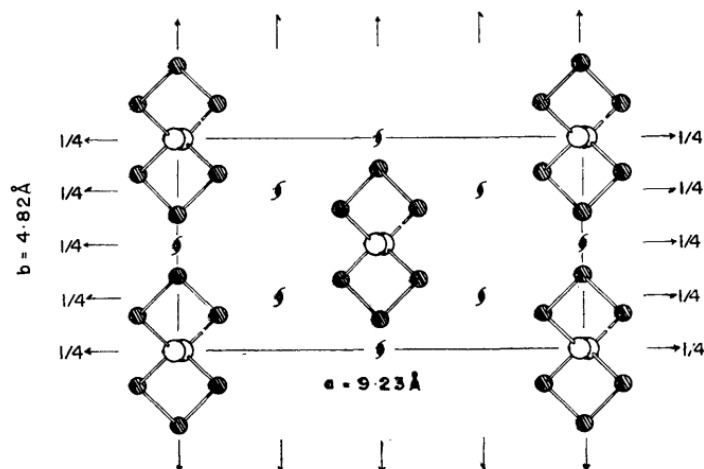
Figure 7: Crystal structure of Modification III of the POCB crystal structure[32]. Reprinted with permission from Tadokoro, H. Structure of crystalline polyethers. Journal of Polymer Science: Macromolecular Reviews 1967, 1, 119–172,

eprint: https://onlinelibrary.wiley.com/doi/pdf/10.1002/pol.1967.230010105.

between water molecules, but also between water and the POCB chains. Infrared analysis shows that OH stretching demonstrates a dichroism 3480-3200 and HOH bending vibrations are approximately $1660 cm^{-1}$, which are comparable to species such as ice VII and oxalic acid dihydrate; both species have hydrogen bonded water molecules. Infrared analysis also discovered the presence of translational or librational modes of the water, which would only be present if the water was bound in a crystal[35].

The planar zigzag orientations of the four POCB chains is the least stable of all the modifications. This is due to the parallel alignment of the dipole moments at the COC groups. Therefore, a stabilizing effect is required, and it can be concluded that the water molecules are providing this effect. The water molecules stabilize the structure by forming a hydrogen bonding network that includes both the water molecules and POCB chains[32].

Isotherms and dissociation pressures were also measured for the hydrate for temperatures

between $-25°C$ to $20°C$. This analysis confirmed that the water molecules were equal in number of moles to the monomer and located within the crystal itself. The dissociation heat was also determined to be $3.25 * 10^3 \frac{J}{mol}$ [35].

1.4 Polyethylenimine (PEI)

1.4.1 PEI as a Polymer

PEI has been in use as an industrial product since 1938, and at the time was primarily used in water-repellent finishing of paper and textiles, conferring dyeability on said paper and textiles, manufacturing reactive dyes, etc. It is primarily obtained via the polymerization of aziridine or the thermal decomposition of 2-oxooxazolidine [36].

The acid polymerization of aziridine forms oligomeric PEI. In this form, PEI is a viscous, colorless resin that forms chains of relatively low molecular weights. These molecular weights do not exceed 1000 - 2200 g. which is the mean molecular weight of the PEI depending in the conditions of the polymerization. For instance, if the concentration of the aziridine is increased and the minimal amount of catalyst is used, the molecular weight of the final product will increase. The same effect can be achieved by raising the temperature during the polymerization, although the temperature effect is more substantial as the initial concentration of aziridine increases [36].

PEI is often a strongly branched polymer. The degree of branching increases as temperature and concentration of the acid catalyst increase. At lower temperatures ($20°C$) the degree of branching falls from 38% to 12% at higher temperatures. Unbranched (linear) PEI is obtained by the polymerization of N-substituted aziridine, and it goes up to a mean molecular weight of 2000 g. The linear PEI crystals melted at $60°C$ a reached a maximum molecular weight of 10^5g [37][38], with a monomer unit as seen in Figure 8.
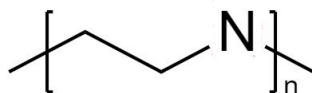
Figure 8: Chemical structure of a linear PEI monomer unit

1.4.2 PEI as Polymer Hydrates

Much like POCB, PEI forms hydrate crystals in the presence of water molecules. Unlike POCB however, PEI forms three different hydrates based on the molar ratio of water to PEI.

1.4.2.1 Hemihydrate

The first of these is the hemihydrate, which has a molar ratio of one mole of PEI to half a mole of water. The crystal structure contains four water molecules and eight monomer units of PEI, but has two different unit cells that differ only in angle β. The first unit cell is: $a = 1.089nm$, $b = 0.952nm$, $c = 0.731nm$, and $\beta = 127.6°$. The second unit cell is: $a = 1.170nm$, $b = 0.952nm$, $c = 0.731nm$, and $\beta = 132.5°$. The cells have equal volume, and a density of $1.14\frac{g}{cm^3}$. By diagonal least square refining of the unit cells, the second cell gave unreasonable bond lengths, suggesting that the first unit cell should be adopted.

The chains in the hydrate are essentially planar zigzag, and parallel to the bc plane. The water molecules however are on a two-fold rotation axis parallel to just the b axis. The water molecules are also tetrahedrally coordinated by their oxygen atoms and the nitrogen atoms of the PEI. There are also two types of hydrogen bonds in this hydrate, the N–H-O and the N-H–O. The first has a bond length of 0.287nm while the second has a bond length of 0.305nm, while the water molecules do not form a network of hydrogen bonds, differing from all other hydrate forms discussed in this thesis. The full crystal structure of the hemihydrate can be seen in Figure 9[39].
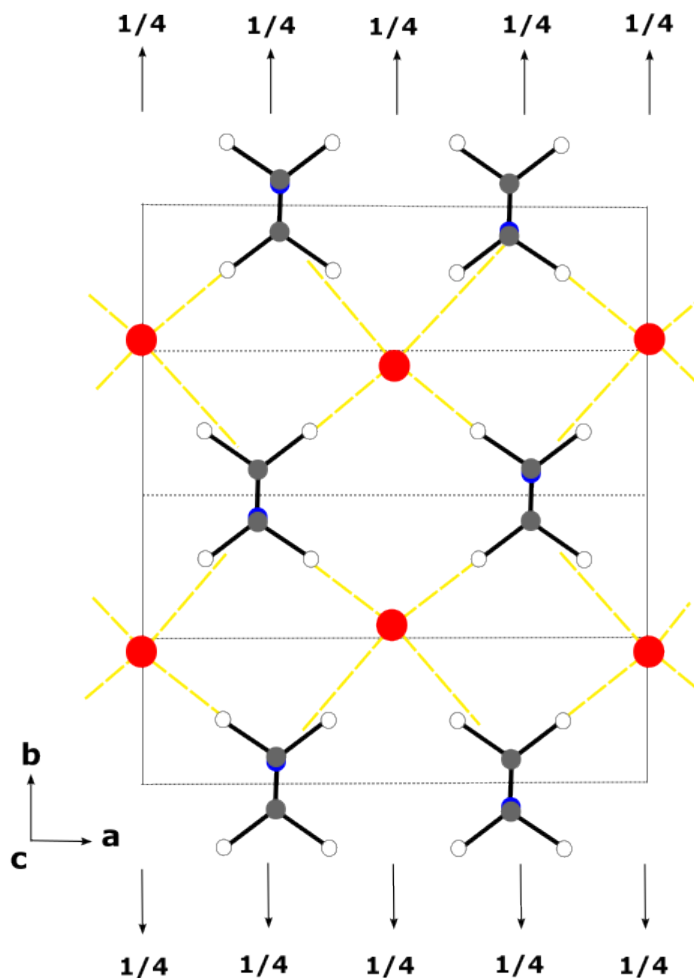
Figure 9: Crystal structure of the PEI hemihydrate. Broken lines indicate hydrogen bonds, but hydrogen atoms of NH groups and of water molecules are omitted[39].

1.4.2.2 Sesquihydrate

The next hydrate formed is the sesquihydrate, which has a molar ratio of two moles of PEI to three moles of water. The PEI is once again in a planar zigzag conformation, but this time the eight monomer units of PEI are accompanied by twelve water molecules. The chains are still parallel to the bc plane, but the water molecules form a more complex network in the crystal. The monoclinic unit cell for this structure is: $a = 11.55 \mathring{A}$, $b = 9.93 \mathring{A}$, $c = 7.36 \mathring{A}$,

and $\beta = 104.5°$ with a space group of C2/c, which can be seen in Figure 10.
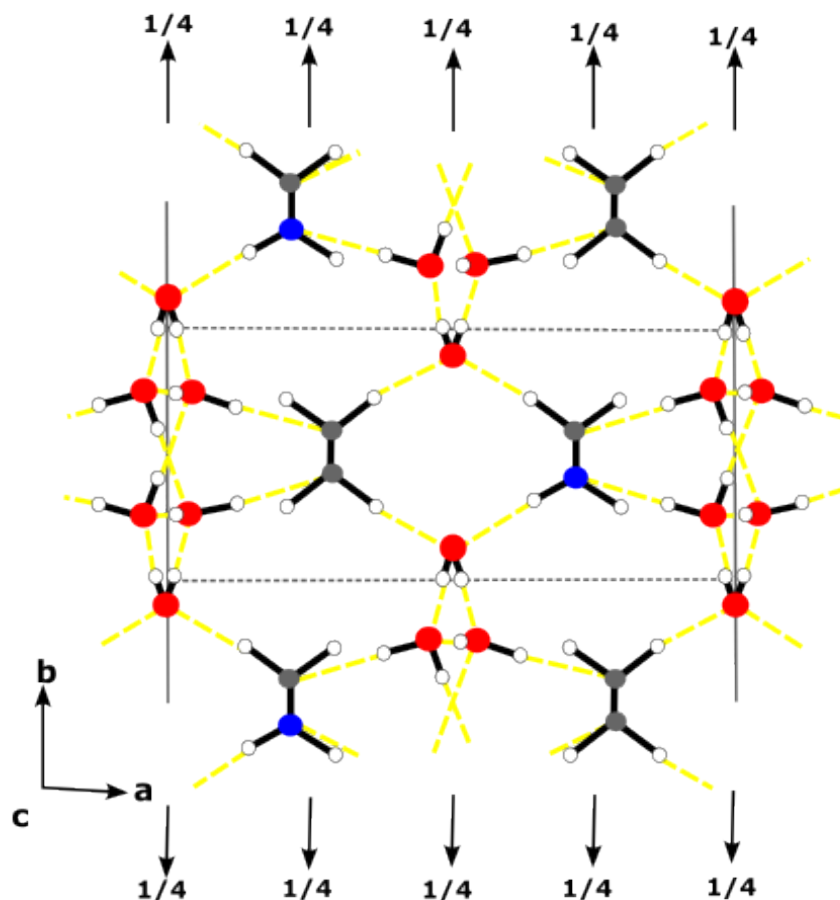
Figure 10: Crystal structure of the PEI sesquihydrate. Broken lines indicate hydrogen bonds[40].

In the water network, each water molecule's oxygen atom is bonded to four hydrogen atoms, two these being covalent bonds and two being hydrogen bonds from other water molecules or NH groups. The water molecules form staggered pentagonal rings, which are similar to that of water cages in clathrate and semiclathrate hydrates. The key difference between the water structure in the hydrate vs clathrates is that the five oxygen atoms are coplanar or almost coplanar. The water structure can be seen in Figure 12. In any case, all the possible hydrogen bonds that are able to participate do participate in this structure[40].

14

1.4.2.3 Dihydrate

The final structure is the dihydrate, which has a molar ratio of one mole of PEI to two moles of water. The PEI chains are in the same configuration as the previous two hydrates, but this time only four monomer units of PEI are present alongside eight water molecules. The monoclinic unit cell of this structure is: $a = 13.26\mathring{A}$, $b = 4.61\mathring{A}$, $c = 7.36\mathring{A}$, and $\beta = 101.0°$ with a space group of C2/c, which can be seen in Figure 11.
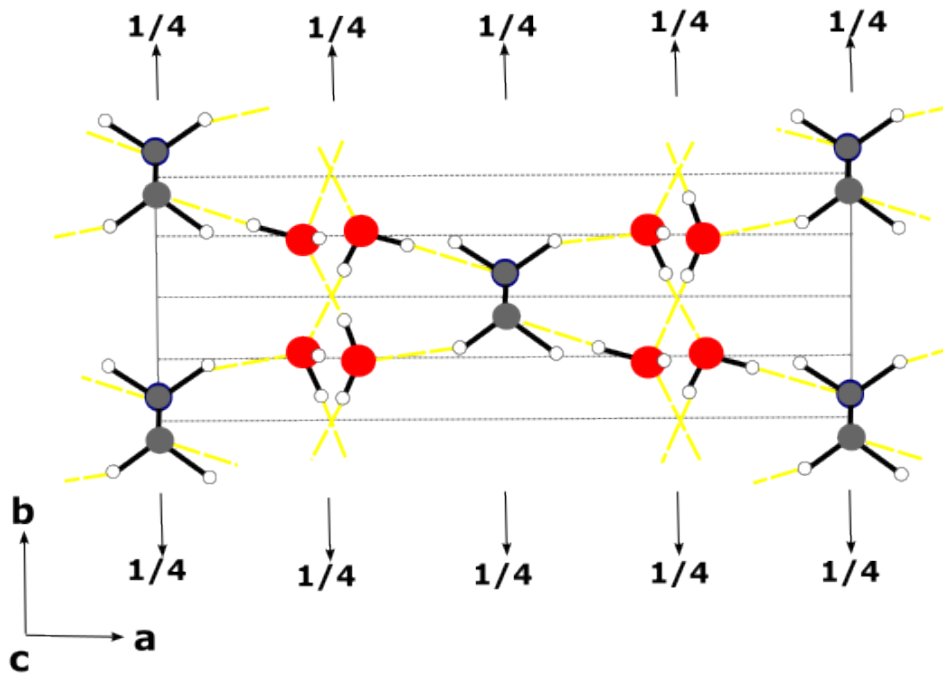
Figure 11: Crystal structure of the PEI dihydrate. Broken lines indicate hydrogen bonds[40].

Once again, each water molecule's oxygen atom is bonded to four hydrogen atoms in the same ways as before. This water network is very similar to that of ice I_h, with the network only being slightly distorted as seen in Figure 12. The network consists of hexagonal stacks of water molecules. These alternate with polymer chains arranged in parallel to the bc plane[40].

1.4.2.4 Thermodynamic Properties

The thermal behaviors of PEI and its hydrates in a water vapor atmosphere was also investigated in order to develop a phase diagram. Dried PEI polymer (anhydrate) was found to melt at about $60°C$ during heating. Once a small amount of water was introduced, the anhydrate began to transition to a mixture of the hemihydrate and sesquihydrate at approximately $40°C$. The hemihydrate transitioned fully into the sesquihydrate at $60°C$, which melted at $80°C$. For a system with substantially more water forming a dihydrate, the system transferred to a sesquihydrate at about $65°C$, with the dihydrate melting about $110°C$ [41]. Differing initial water content did seem to effect the melting points of each hydrate slightly, creating a range of melting points over a phase diagram, which can be seen in Figure 13.

1.5 Goals and Motivations of this Work

The behavior of these polymer hydrates is similar to that of clathrates but are not entirely the same. The conditions under which these hydrates form is seemingly impossible, water simply does not form ice-like structures at ambient pressure and temperatures. It should also be stated that these structures are unlikely to be unique, and there maybe yet undiscovered polymer hydrates.

A goal of this work is to understand the reason for the hydrate formation. On a fundamental basis, it is odd that these hydrates create ice like structures under ambient conditions, so determining the forces holding them together is fundamentally important to understanding them. An additional goal is to use this information to develop characteristics and trends that would allow a screening of chemical space for existing and possible polymer hydrates.

These hydrates seem ideal in applications similar to that of clathrates. The problem with clathrate applications is the expense. Wu et. al[42] shows that clathrate hydrates must

have productions costs reduced before they can be economically viable for gas extraction, and in the best conditions wells utilizing clathrates wouldn't have a net positive effect for approximately 12 years. These polymer hydrates however can form and be stored under ambient conditions, which may lower the overall production expenses associated with their use in similar fields. The primary application in mind is that of water desalination, due to the process not requiring large amounts of electricity, something that may not be readily available around the world.

ICE   1.5-HYDRATE   2-HYDRATE
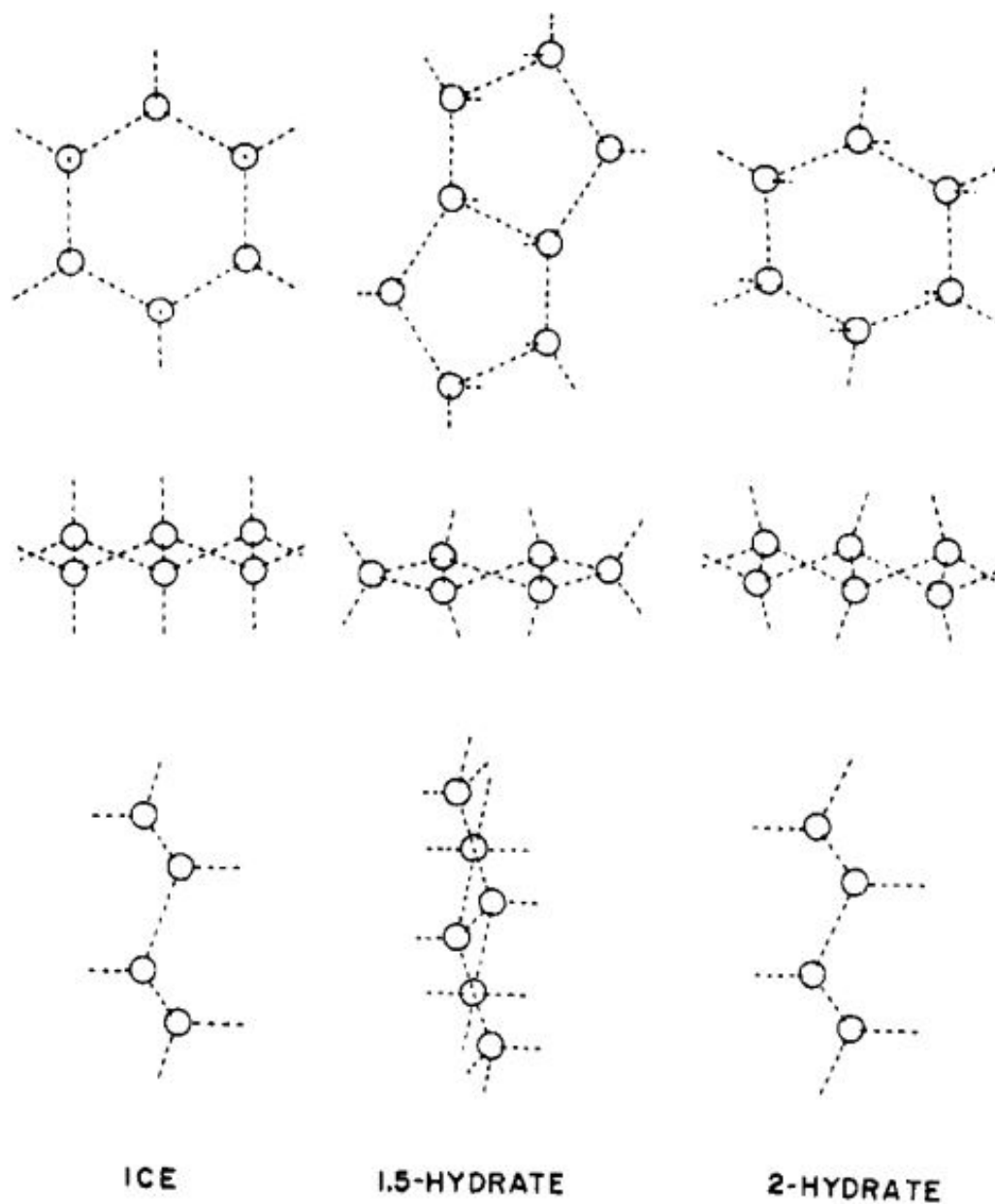
Figure 12: Water networks of ice Ih, the sesquihydrate, and the dihydrate [40]. Reprinted (adapted) with permission from Chatani, Y.; Tadokoro, H.; Saegusa, T.; Ikeda, H. Structural studies of poly(ethylenimine). 1. Structures of two hydrates of poly(ethylenimine): sesquihydrate and dihydrate. Macromolecules 1981, 14, 315–321, Publisher: American Chemical Society. Copyright 2022 American Chemical Society.
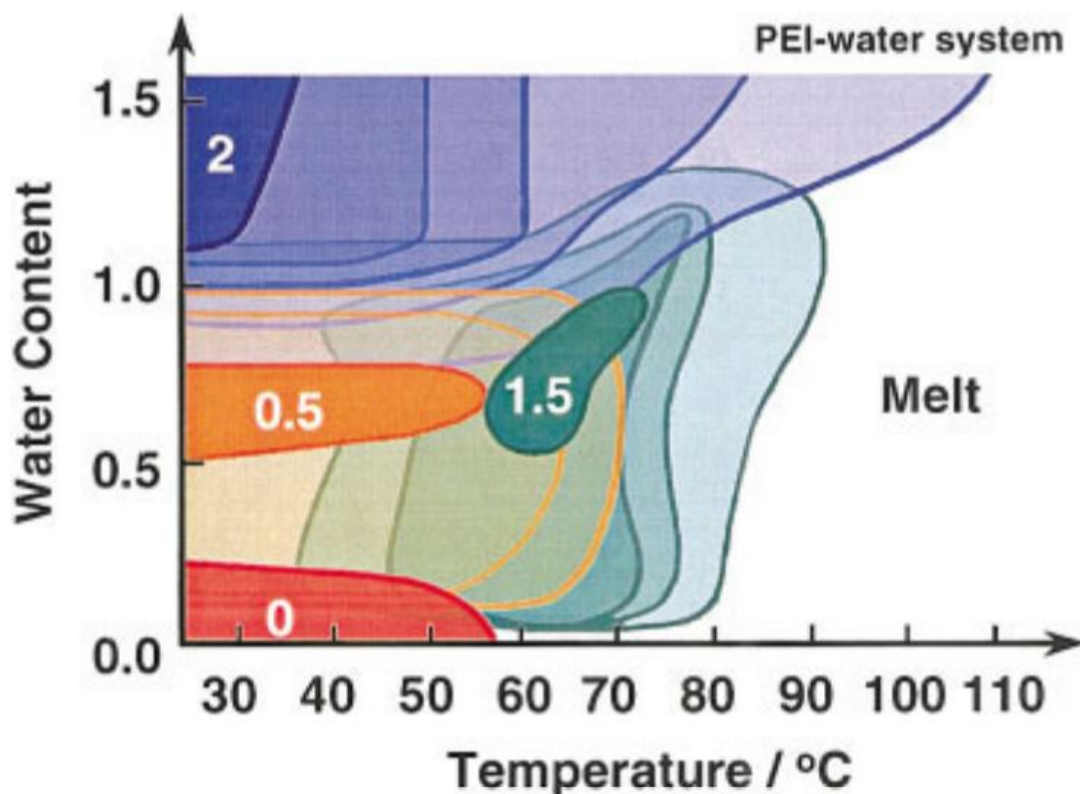
Figure 13: A phase diagram of PEI hydrates as a function of water content and temperature, where the water content is indicated by the relative intensity of the infrared water band reduced by an internal standard band[41]. Reprinted with permission from Hashida, T.; Tashiro, K.; Inaki, Y. Structural investigation of water-induced phase transitions of poly(ethylene imine). III. The thermal behavior of hydrates and the construction of a phase diagram. Journal of Polymer Science Part B: Polymer Physics 2003, 41, 2937–2948, eprint: https://onlinelibrary.wiley.com/doi/pdf/10.1002/polb.10611.

2.0   Classical Dynamics and Physical Properties

2.1   Background

Polymers exhibit differing phenomena over a large range of length scales as small as angstroms to tens of nanometers at the radius of gyration to and larger in melts, and timescales ranging from seconds to years in the most extreme cases. In recent years the advancement of technology has allowed for more simulations to be conducted on these species at a faster rate, which has opened the doors for exploring these phenomena [43]. Atomisitc models were focused on due to their ability to accurately model local interactions and monomer-level (re)arrangements. This is all preferred for modeling a crystal-melt accurately, which requires the understanding of local bond orientation, bond formation and breaking, etc [44]. However these models are not without their flaws. Molecular dynamics models have higher computational expense, leading to limitations of length scales to 1-100$\mathring{A}$ and time scales of 1 fs - 100 ns. These simulations may also take a non-trivial amount of time to complete despite their smaller size, although the trade off in speed is accounted for in higher accuracy. This higher accuracy is heavily dependent on forcefields used, the initial simulation configuration, and the simulation protocol, and being incorrect in any of these categories can lead to incorrect results. To ensure correct results, it is suggested that these models are first used to find a known quantity from experiments, and to test multiple forcefields to get the best possible choice for the simulation[45].

As discussed in the introduction, hydrates store large amounts of resources in nature. The large gas storage potential of hydrates has led to studies that purposefully utilize hydrates as a storage-media for natural gas[46], hydrogen[47], and carbon dioxide[48]. An obstacle to the realization of this technology is the high pressure and low temperatures required for the hydrates to form. Therefore, being able to model thermodynamic properties of these hydrates would alleviate the need to test every hydrate experimentally for storage purposes. Instead, accurate models could be used to predict behaviors that are most ideal

for practical use across all of chemical space[49]. Computational studies have focused on the most prominent of these hydrates, which include those that trap methane, carbon dioxide, and tetrahydrofuran (THF).

In 2010 Tung et. al.[50] used molecular dynamics to identify the key factors that affect the growth of methane hydrates. They found that methane solubility in water, mass transport of methane by diffusion, and the affinity of methane to incomplete water cages at the interface were the dominant factors. The solubility of methane increased with its partial pressures in the vapor phase, which resulted in increased growth at higher pressures. Methane molecules that were absorbed onto the interface ejected water molecules in order to form the cages, which consequently lowers the methane concentration, furthermore, causing the growth rate to be determined by the competition of methane absorption at the interface and the methane diffusion from the bulk to the interface. At the melting point, the affinity of the methane molecules to the interface becomes zero, ceasing the freezing. All of these insights were supported by the fact that the simulations could reproduce the experimental melting point of methane hydrates.

In 2011 Shin et. al.[51] investigated thermodynamic inhibition of the formation of CO_2 clathrates using molecular dynamics. The study determined that ionic liquids did in fact inhibit the formation of these hydrates, decreasing the overall melting temperature by 0-1.75 K at a range of pressures. The main contributors were the anions, with a particular strength being demonstrated by Cl^-. The authors concluded that if an ionic liquid has a negative hydration free energy, then it will produce increased inhibitory effects on the hydrate formation.

In 2019 Naeiji et. al.[52] utilized a cyclopentane (CP) hydrate to coat a THF hydrate at the unit cell level in order to better preserve it. Molecular dynamics was used to simulate the melting temperatures of both the hydrates individually, as well as together. The model produced melting temperatures of the THF and CP hydrates of 270K and 290K respectively, which were not significantly different from the experimental values of 27.5K and 281K. The results showed that the coating does indeed preserve the THF hydrate readily, allowing the

THF to be super-heated when coated. The coating also increased the simulation time from 20 ns to 120 ns before melting would occur.

The lack of available knowledge of polymer hydrates means that the simulations need to be informed by simulations of their small molecular counterparts, as well as the general melting of polymers. Melting of pure polymers is traditionally simulated in one of two ways. The first is a coarse grained approach, and is utilized for longer chain lengths and time scales where the individual molecular interactions are not of interest, but instead the bulk behavior is sought[45]. The atomistic models are used for shorter chain lengths and time scales. Cho et. al.[53] for instance used time scales ranging from 5 to 15 ns to model the melting of linear, untangled polyethylene, with a unit cell of approximately 120 molecules representing the systems. All the previously discussed studies had timescales ranging from picoseconds to nanoseconds, with the Tung and Naeiji studies having time scales of 40 and 20 nanoseconds respectively for the base hydrates. For the hydrate melting, all three hydrates studies first equilibrated the system using NVT at a temperature below the melting point before using NPT to melt the structure.

This lack of knowledge in this field opens the door for many simulations. Predicting physical properties of the polymer hydrates would help to better understand the material, and benchmarking existing forcefields on these unusual structures is a great way to test their generality.

2.2   Molecular Simulation Studies of Hydrates

2.2.1   Classical Forcefield Typing

In molecular dynamics, a forcefield is a method used to estimate the forces between atoms and molecules in a system. The forcefield is a set of functional forms and parameters

used to calculate the potential energy of a system. A general example of a potential energy functional form is:

$$E_{tot} = E_{bonded} + E_{nonbonded} \tag{2.1}$$

where:

$$E_{bonded} = E_{bond} + E_{angle} + E_{dihedral} \tag{2.2}$$

$$E_{nonbonded} = E_{electrostatic} + E_{vdW} \tag{2.3}$$

General forcefields tend to provide this information for all atoms, and the atoms of an individual system must be typed by the user. This means that the user must assign values to each atom type present in a system in accordance with the preferred forcefield.

In this work the General Amber Force Field 2 (GAFF2)[54] and Dreiding[55] forcefields were utilized for their generalizability. GAFF2 utilizes the following harmonic functional form:

$$E_{pair} = \Sigma_{bonds} K_r (r - r_{eq})^2 + \Sigma_{angles} K_\theta (\theta - \theta_{eq})^2 + \Sigma_{dihedral} \frac{V_n}{2} (1 + cos(n\phi - \gamma) + \Sigma_{i<j} (\frac{A_{ij}}{R_{ij}^{12}} - \frac{B_{ij}}{R_{ij}^6} + \frac{q_i q_j}{\epsilon R_{ij}})$$
$$\tag{2.4}$$

where r_{eq} and $q_e q$ are the equilibrium structure parameters; K_r, K_θ, and V_n are force constants; n is the multiplicity and γ is the phase angle for torsional angle parameters.

Dreiding utilizes the functional form:

$$E = E_{bonded} + E_{nonbonded} \tag{2.5}$$

$$E_{bonded} = E_B + E_A + E_T + E_l \tag{2.6}$$

$$E_{nonbonded} = E_{vdW} + E_{electrostatic} + E_{hbond} \qquad (2.7)$$

where E_B is the two-body bond stretch, E_A is the three-body angle bend, E_T is the four-body dihedral angle torsion, E_l is the four-body inversion term, and E_{hbond} is explicit hydrogen bonds. It is apparent that the Dreiding forcefield has very similar properties to that of the general terms shown in Eqs. 2.1, 2.2, and 2.3 with some additional terms, demonstrating that it fits a generic forcefield model.

Rukmani et. al.[56] conducted a molecular dynamics study of water-soluble polymers where Dreieding and GAFF2 were directly compared. In this study, Dreiding showed better agreement with experimental data for radius of gyration, regardless of the water model used. Dreiding also performed the best in general, although the water model was far more important in accurately predicting properties. While both forcefields performed well, Dreiding having an explicit hydrogen bonding term seems to have given it the edge, at least in the presence of water. However, GAFF2 is a newer forcefield, and is more well defined than the older Dreiding. The difference in the data suggests while Dreiding is better overall in this scenario, GAFF2 is still not a bad choice for models of this type.

2.2.2 Annealing Simulations

Using the Large-scale Atomic/Molecular Massively Parallel Simulator (LAMMPS)[57] molecular dynamics software, the melting of the POCB hydrate was studied. The goal was to create a model with generic forcefields that could accurately reproduce the known experimental melting point. Once this was done, the model could be used to predict other, unknown properties of the hydrate to grant greater insight into the behavior of these unknown systems.

The simulations were run according to the following scheme. First, the system was equilibrated using NVE (where temperature and pressure may vary) to relax the system over 1 ns. The system was equilibrated at 100K using NVT to ensure the structure is fully crystalline while finding an equilibrium pressure over 1 ns. Finally, the temperature is raised from 100k

to 400K to melt the crystal at constant pressure over 10 ns. This method was chosen due to similarity to methods previously discussed, and the timescales also come from those previous works.

The GAFF2 results can be seen in Figure 14. As temperature increases, the potential energy of the system continues to increase linearly. There is no significant change over the course of the simulation to indicate melting. The Dreiding results in Figure 15 tell the same story. The POCB hydrate was not at all melting over the course of these simulations. For example, Figure 16 demonstrates a melting simulation plot of a methane clathrate[58]. At the point of melting, there is a large vertical shift in internal energy, something not present in either of the POCB data sets, suggesting that the system is not melting.
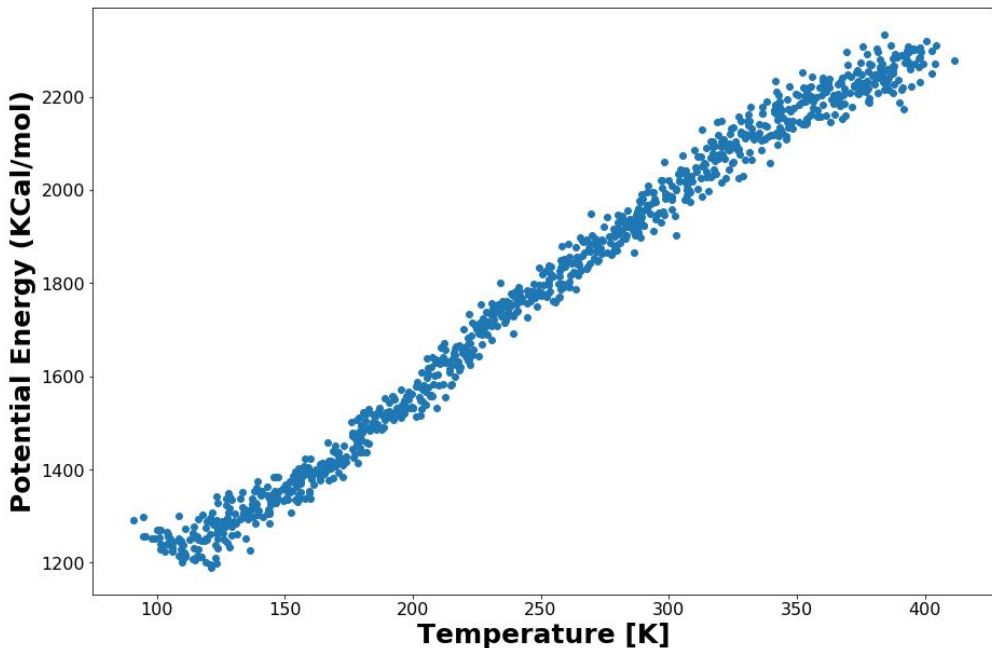
Figure 14: Temperature vs the Potential Energy of the POCB Hydrate during a LAMMPS annealing simulations using the GAFF2 forcefield

It was ultimately concluded that these results are sensible because polymer melting points are proportional to the molecular weight of the polymer. These systems can be represented by an equation taking the form:
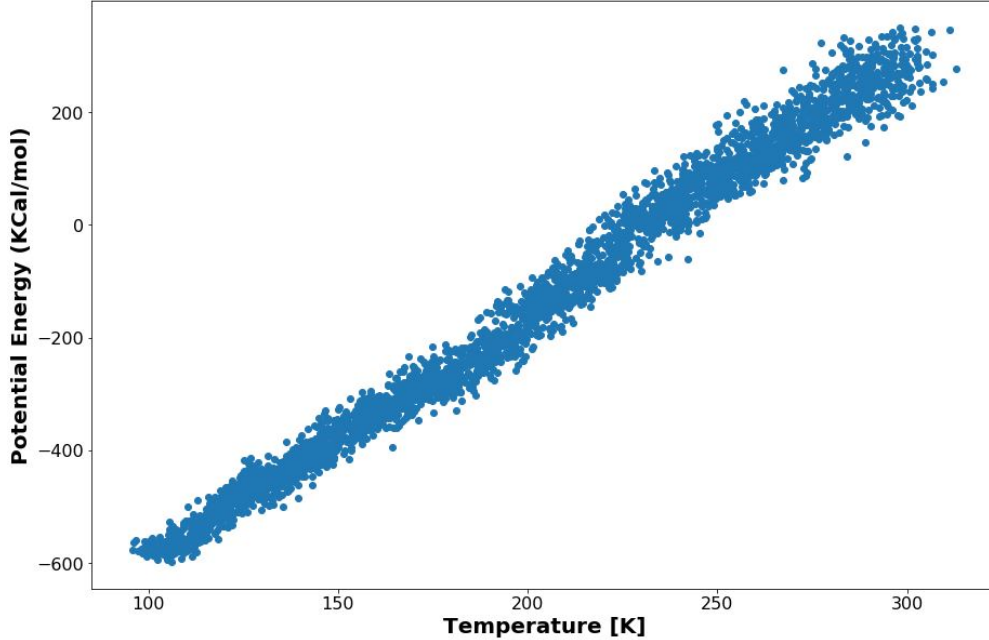
Figure 15: Temperature vs the Potential Energy of the POCB Hydrate during a LAMMPS annealing simulations using the Dreiding forcefield

$$X(M_n) = X_\infty - \frac{B}{M_n} \tag{2.8}$$

where X is the thermodynamic property, X_∞ is the asymptotic value at an infinitely high molecular weight, and B is some related constant. In the model used for this study, the POCB chain was infinitely long, and therefore its molecular weight was infinitely high. Without knowledge of the asymptotic value that the melting point reaches, it is both expensive and time consuming to run simulations searching for this point. It can be easily concluded that the simulations that were run did not approach this point, since the systems did not melt. So, while the simulations did run correctly, the hydrate's melting point was never reached across any simulations. Since the polymer hydrates already have known chain length where the polymers form, creating a unit cell that contains chains of the proper length with appropriate capping agents is necessary to accurately predict the experimental melting point. Therefore, it was concluded that the simulation could properly simulate melting if the structure was
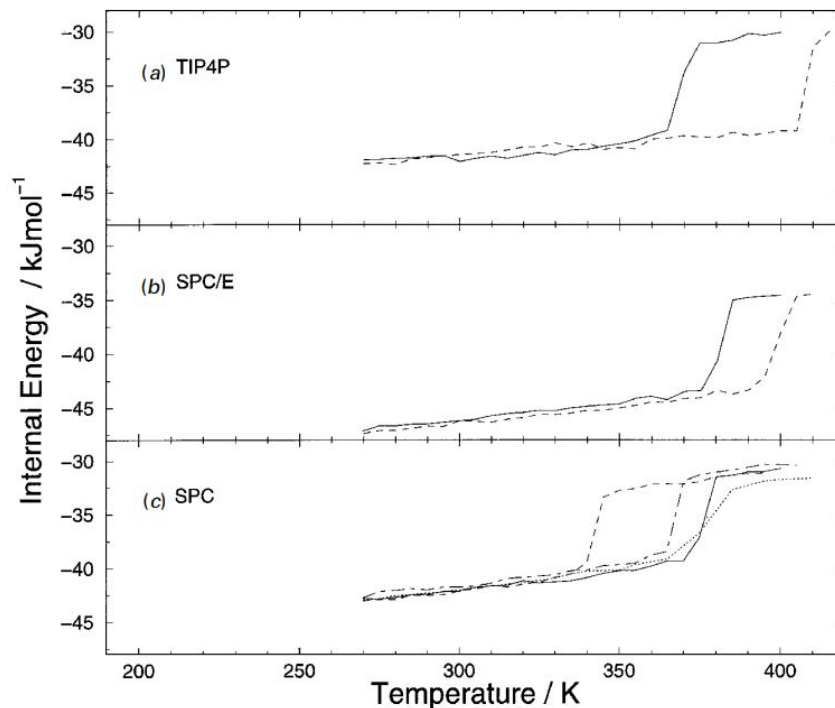
Figure 16: Temperature vs the Internal Energy of a methane clathrate demonstrating the melting point of the system[58]. Reprinted with permission from Forrisdahl, O. K. Molecular Physics 1996, 89, 819–834.

correct, but without this the simulations would not predict a realistic melting point.

2.3   The Finite Polymer Chain Code

To create a proper structure, work began on developing a script that would create finite polymer chains. At the time of writing, no code currently exists that will insert breaks into the hydrate crystals needed to more accurately represent the system. The unit cell that was used was ultimately too rigid, causing a lack of melting. Breaking up the polymer chain substituting in water molecules between the broken-up chains would theoretically decrease rigidity due to the replacement of covalent bonds with non-covalent bonds which allows

greater flexibility. Introducing these finite chains could potentially improve the simulation because this would introduce anisotropies in the crystals. The goal was to create a computational modeling tool that could read in a structure file for a 3D periodic system and insert breaks in the polymer chains of the user's choosing with a placeholder in-between the polymer chains. A full version of this tool was not finalized, but a draft of the code is available in Appendix C.

3.0   Hydrate Models

In order to investigate intermolecular interactions and their effect on the formation of these hydrates, the hydrate unit cells had to be made into cluster models. First however, the unit cells of the hydrates had to be optimized so that hydrogen positions were realistically represented and physically correct.

3.1   Experimental Atomic Structures

All of the analyzed structures were based on experimental structures found in the literature. The full unit cells were generated by the author using this information prior to geometric optimization. The information for all the initial unit cells in below[31][35][39][40][59]:

Table 1: Experimental structure information used to create unit cells for all of the structures in this study.

	a	b	c	α	β	γ	Space Group
POCB	9.23$\mathring{A}$	4.82$\mathring{A}$	7.21$\mathring{A}$	90°	90°	90°	$C222_1 - D_2^5$
POCB Hydrate	12.3$\mathring{A}$	7.27$\mathring{A}$	4.80$\mathring{A}$	90°	91°	90°	$C2/m - C_{2h}^3$
PEI	29.8$\mathring{A}$	17.2$\mathring{A}$	4.79$\mathring{A}$	90°	90°	90°	$D_{2h}^{24} - Fddd$
PEI Hemihydrate	10.89$\mathring{A}$	9.52$\mathring{A}$	7.31$\mathring{A}$	90°	127.6°	90°	$C2/c$
PEI Sesquihydrate	11.55$\mathring{A}$	9.93$\mathring{A}$	7.36$\mathring{A}$	90°	104.5°	90°	$C2/c$
PEI Dihydrate	13.26$\mathring{A}$	4.61$\mathring{A}$	7.36$\mathring{A}$	90°	101°	90°	$C2/c$

Other information, such as initial XYZ coordinates for atoms and full structures are available in Appendix A.

3.2   Periodic Optimization Calculations

For the following calculations, the Vienna Ab initio Simulation (VASP) Package was used to geometrically optimize all the structures used in this work. For all the following calculations, DFT PBE was used with Grimme's DFT-D2 dispersion corrections applied. An ionic relaxation was done, with a maximum number of 100 ionic steps, and 60 electronic self-consistency steps. A blocked Davidson iteration scheme was used, and the calculations were spin polarized. Dipole corrections were not accounted for due to convergence difficulties.

3.2.1   Energy Cutoff Calibrations

During these calculations, the energy cutoff was varied for the same structure until the final energies converged. For the purposes of this thesis, the PEI results will be discussed and compared.

For the hemihydrate, the energy cutoff was varied in the range of 200 to 800 eV in 100 eV iterations. These calculations were all run with KPOINTs set at 111. Figure 17 shows that, outside of an outlier at 300 eV, all the cutoffs for the hemihydrate are nearly identical in terms of energy. Therefore, in theory, a given energy cutoff in this range (with the exception of 300) could be used.

For the sesquihydrate, the same analysis was done. Figure 18 shows that the energy converged almost immediately at 300 eV. The curve is then fairly smooth across all cutoffs, similar to that of the hemihydrate.

This analysis was done again for the dihydrate. Figure 19 shows that at energy cutoffs 300 to 600, the energy seems to converge. Above 600 however, the energy spikes and changes dramatically after each iteration. Therefore, it was concluded that a cutoff of either 500 or 600 eV would be best, since they are the lowest energy and at the point of approximate convergence.

Since all three PEI hydrates seemed to converge over the same energy, an energy cutoff of 600 eV was chosen for all the optimization calculations done in this study.
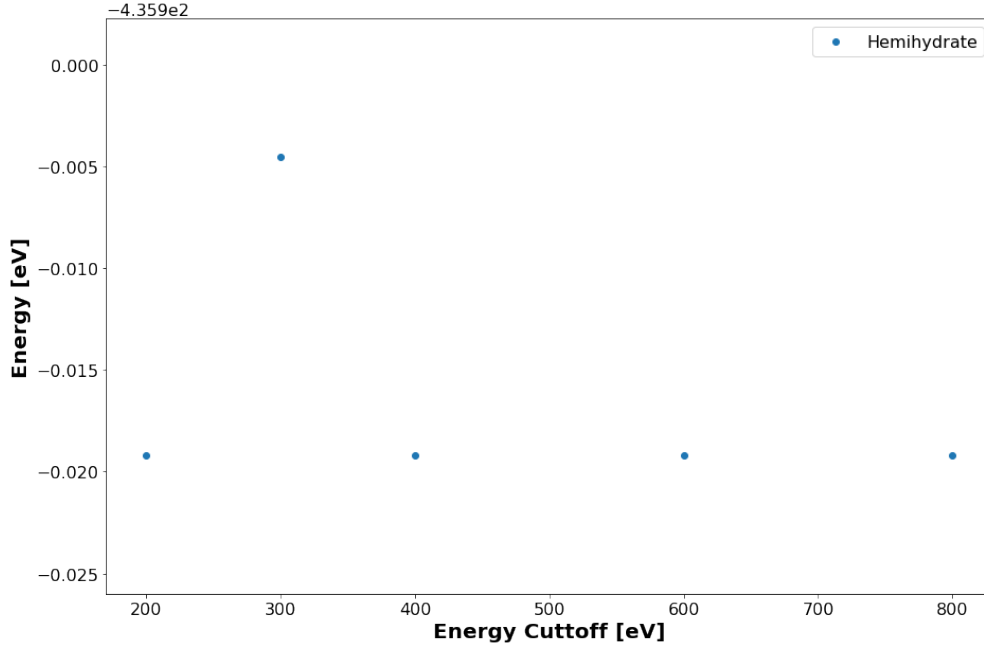
Figure 17: Energy cutoff calibration calculations with respect to energy cutoff and final energy for the PEI hemihydrate

3.2.2 KPOINT Sampling

Using the calibrated energy cutoff, the KPOINTs of each system were varied as well. For all systems the KPOINTs were varied in the range of 111 to 555, increasing all KPOINT dimensions by 1 each iteration. For the hemihydrate, Figure 20 shows that the KPOINTs do not seem to converge at a given point. The lowest energy point is at point 222, while the others had higher energies and significantly longer calculation times. Therefore, KPOINTs of 222 were chosen.

The same behavior can be seen in Figures 21 and 22 for the sesquihydrate and dihydrate respectively. When considering computational cost and time, as well as the lack of any clear convergence, KPOINTs of 222 were used for all systems in this study.

For all the results discussed in this section, much of it is still in need of greater inves-
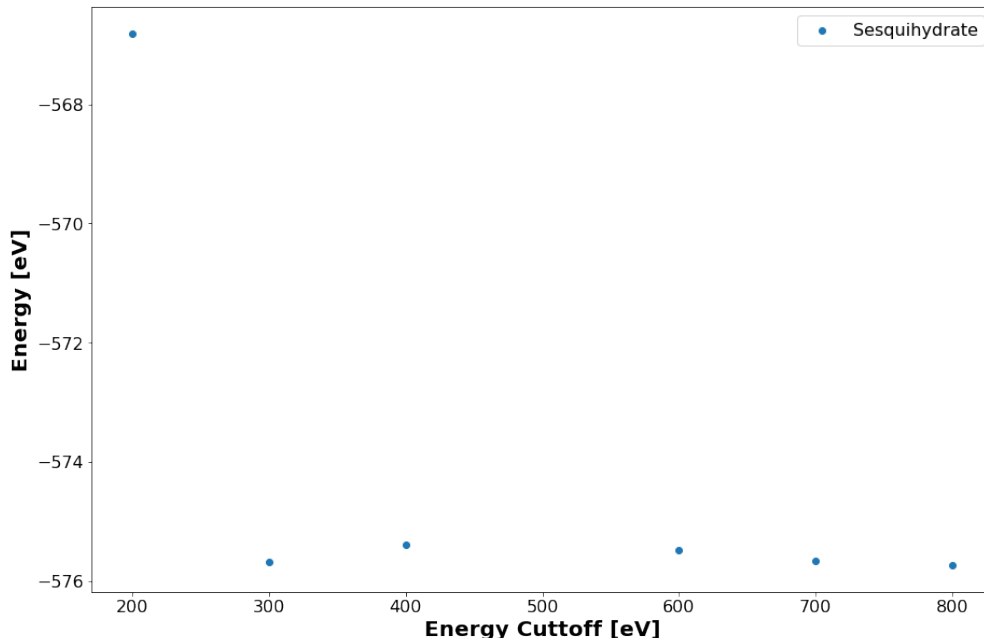
Figure 18: Energy cutoff calibration calculations with respect to energy cutoff and final energy for the PEI sesquihydrate

tigation that is currently underway. The lack of convergence in this calculation is highly concerning, however this does not lessen the following results. The numerical values may be affected if the structures are not perfectly optimized, but the trends presented would still be accurate, and therefore the results are still viable for discussion.

3.3 Molecular Cluster Models

3.3.1 What Makes a Good Cluster Model?

Molecular cluster models are finite system fragments cut out of a full periodic system. The clusters can be treated completely isolated, or even in a field of the surrounding lattice to mimic the crystal environment. The smaller system sizes of the clusters allow for investigating local properties of crystal, rather than just the bulk properties[60].
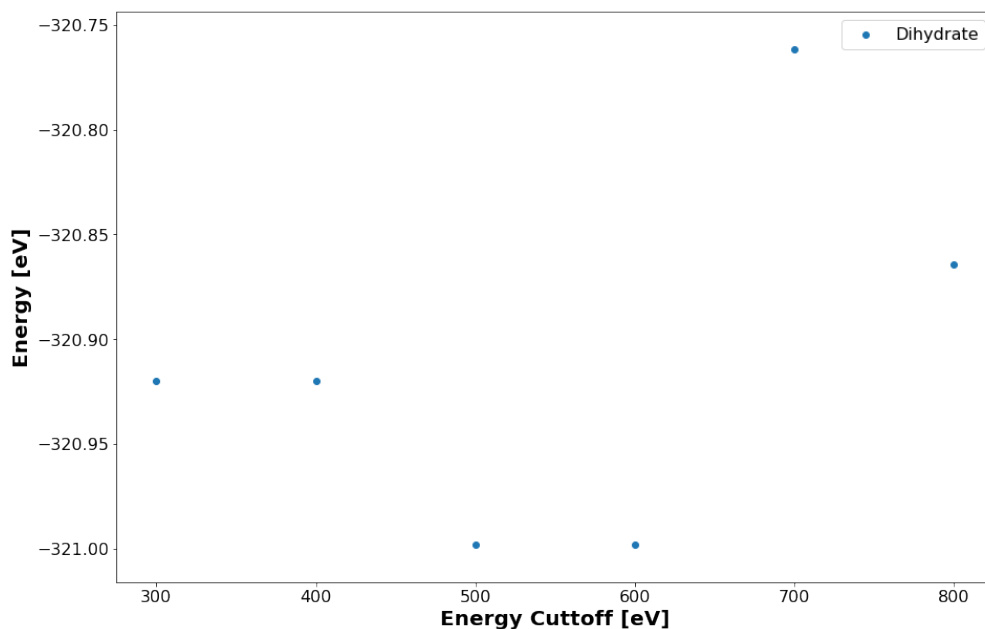
Figure 19: Energy cutoff calibration calculations with respect to energy cutoff and final energy for the PEI dihydrate

The use of cluster models has allowed for the successful DFT investigations of bonding properties, describing surface adsorption, diffusion, as well as heterogeneous catalysis at a lower computational cost. However, care must be taken to ensure the clusters represent the overall system accurately, and that the clusters themselves are not in an unrealistic environment. Poorly representing the system or providing an unrealistic environment can potentially affect the chemical and physical behaviors which may not agree with the real system. Another concern is the underestimation of the binding energies due to the absence of long-range contributions cut out of the cluster, so capturing all major interactions is vital when making a cluster[61].
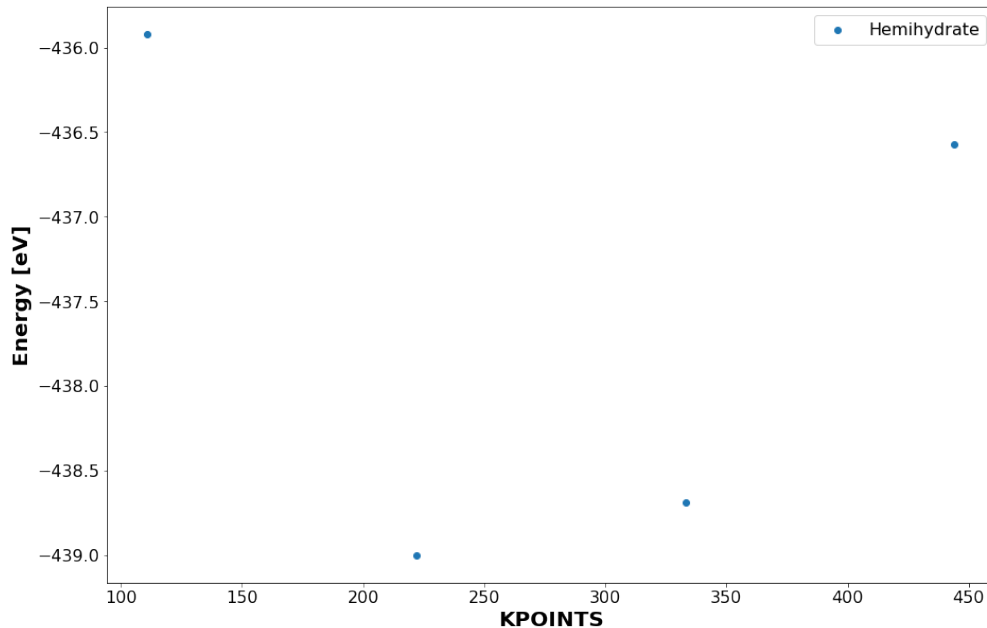
Figure 20: KPOINT sampling calculations with respect to the KPOINTs and final energy for the hemihydrate

3.3.2 Developing Cluster Models

For the sake of this work, cluster models were cut out of VASP optimized crystal structures. Several clusters were made to capture specific intermolecular interactions within the system, and all clusters were considered in order to describe the full system. Clusters were also tested for size dependent interactions by ranging the amount of monomer units in the polymer chains between one and six.

In Figure 23A, the full periodic POCB hydrate unit cell can be seen. In order to transform this into a cluster model, first the periodicity was removed, and capping hydrogens were added to the end groups. Excess atoms were then removed in order to remove duplicate interactions that were already accounted for. The full cluster can be seen in Figure 23B.

Figure 24 shows a further breakdown of the main cluster. All possible major interactions
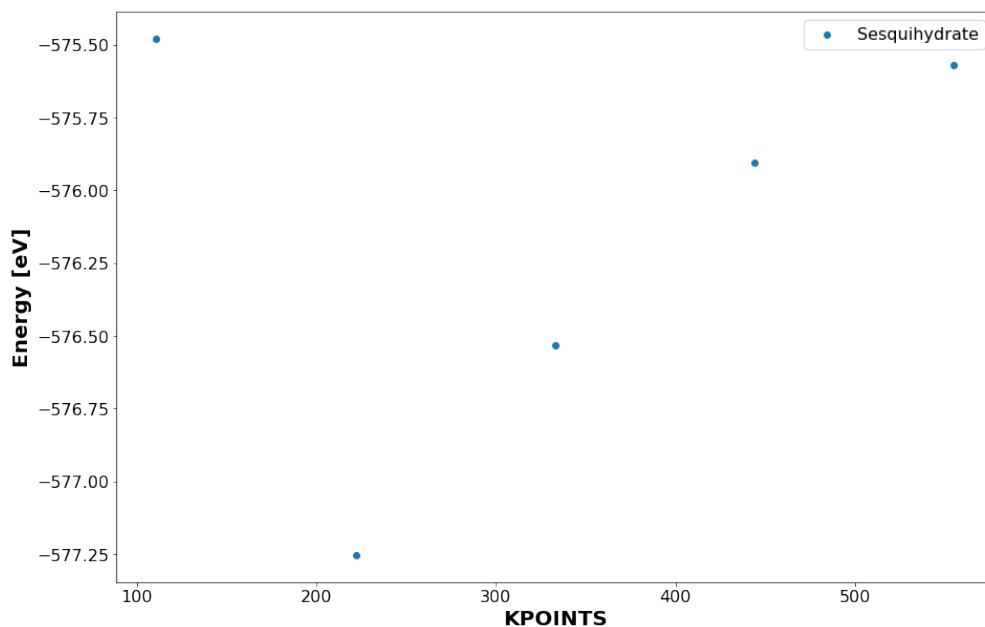
Figure 21: KPOINT sampling calculations with respect to the KPOINTs and final energy for the sesquihydrate

were accounted for in the breakdown to get a full understanding of the system. These clusters were developed with hydrogen bonding and dispersion interactions primarily in mind. This was repeated for all the systems investigated in this work.
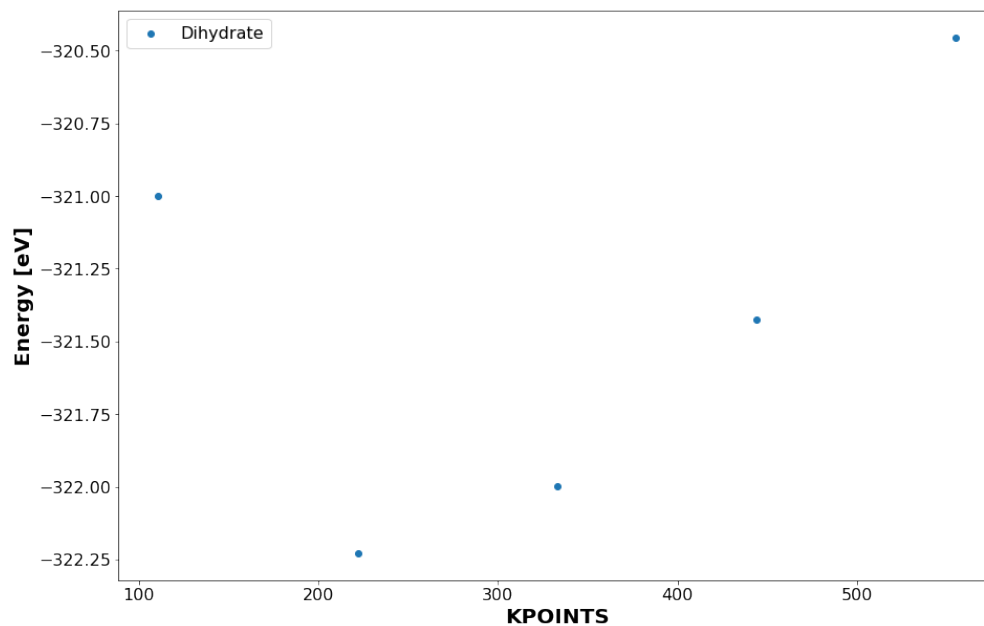
Figure 22: KPOINT sampling calculations with respect to the KPOINTs and final energy for the dihydrate
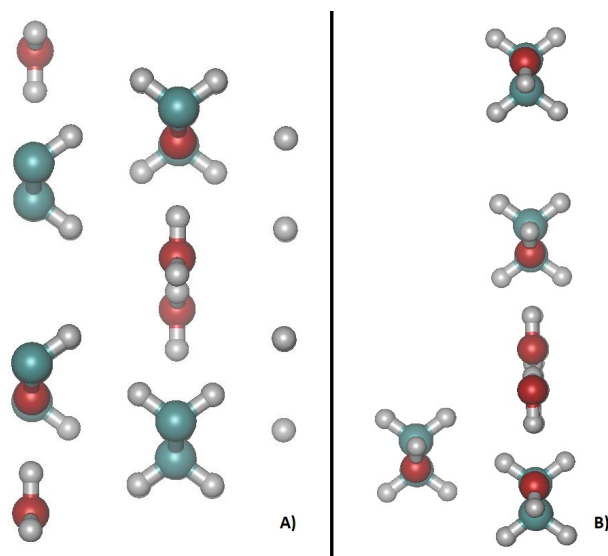
Figure 23: A) Periodic unit cell of the POCB Hydrate B) Full cluster model of the POCB Hydrate
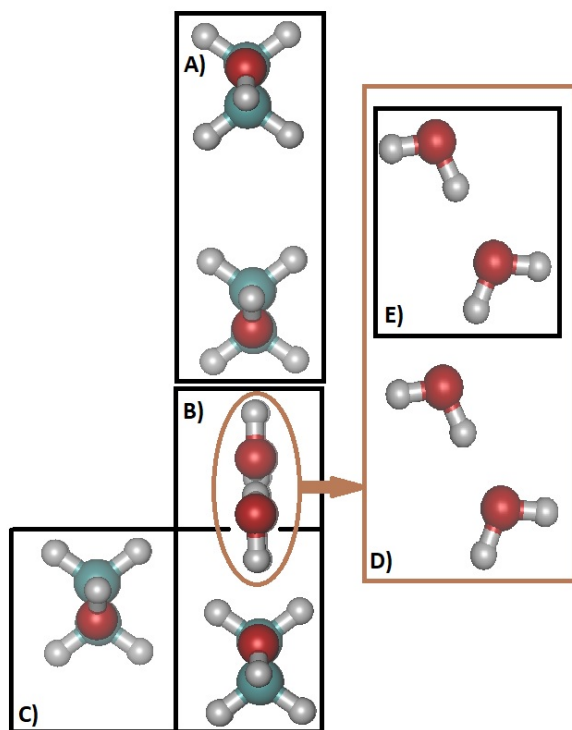
Figure 24: Further breakdown of the full cluster to smaller clusters that were examined. A) POCB-POCB vertically stacked interactions, B) POCB chains interacting with a water chain, C) POCB-POCB interacting in a different orientation, D) A zoomed in view of the water chain, E) Water molecules interacting with each other within the water chain

4.0   Energy Decomposition Analysis (EDA)

4.1   Background on EDA

Understanding chemical bonding properties is a fundamental descriptor that provides insight into plausible models that predict chemical behavior. Early EDA methods were developed by Morokuma[62] and by Ziegler and Rauk[63], and these methods allow for the investigation of the nature of the chemical bond. EDA decomposes the interaction energy ΔE_{int} between two fragments, A and B, in a molecule into different meaningful terms. These terms include:

1. The quasi-classical electrostatic interaction energy between the charge densities of the fragments, ΔE_{elstat}.
2. The exchange repulsion between the fragments due to Pauli's principle, ΔE_{Pauli}.
3. The energy gain due to orbital mixing of the fragments, ΔE_{Orb}.

This original EDA method considers the formation of molecule A-B with the wave function Ψ_{AB} and energy E_{AB} based on the interactions between its fragments, A^0 and B^0 with the corresponding energies E_A^0 and E_B^0 in their electronic and geometric ground states Ψ_A^0 and Ψ_B^0. The energies are subdivided into several steps. In the first step, A^0 and B^0 are distorted from equilibrium geometries and wave functions to new geometries and electronic states $\Psi_!$ and Ψ_B with their corresponding energies in the molecule A-B. The energy needed to excite and distort the fragments in the preparation energy ΔE_{prep} (Eq. 4.1) [64].

$$\Delta E_{prep} = E_A - E_A^0 + E_B - E_B^0 \tag{4.1}$$

The ΔE_{int} is the primary focus of EDA and is calculated based on the energy of the molecule and the energies of the excited fragments (Eq. 4.2).

$$\Delta E_{int} = E_{AB} - E_A - E_B \tag{4.2}$$

The sum of these two energy values is then used to calculate the bond dissociation energy D_e (Eq. 4.3).

$$-D_e = \Delta E_{int} + \Delta E_{prep} \tag{4.3}$$

In the first step, the ΔE_{elstat} is calculated by freezing the charge densities of the excited fragments. A sum is taken over space as the fragments are brought from positions of infinite separation to their respective positions within the molecule. At the equilibrium geometries, the interaction between the frozen charge densities gives the ΔE_{elstat} (Eq. 4.4. This state, known as the promolecule, also provides the product wave function $\Psi_A \Psi_B$ and the corresponding energy of E_{AB}^0 [64].

$$\Delta E_{elstat} = \Sigma_{\alpha \epsilon A} \Sigma_{\beta \epsilon B} \frac{Z_\alpha Z_\beta}{R_{\alpha\beta}} + \int dr V_B(r)\rho_A(r) + \int dr V_A(r) + \rho_B(r) + \int \int dr_1 dr_1 \frac{\rho_A(r_1)\rho_B(r_2)}{r_{12}} \tag{4.4}$$

In step two of the EDA, the product wave function is antisymmetrized and renormalized to give an intermediate state Ψ^0 (Eq. 4.5) with the corresponding energy E^0. The difference between the energy of the intermediate state and the promolecule state is the ΔE_{Pauli} term (Eq. 4.6) [64].

$$\Psi^0 = N\hat{A}\Psi_A \Psi_B \tag{4.5}$$

$$\Delta E_{Pauli} = E_{AB}^0 - E^0 \tag{4.6}$$

In the third step Ψ^0 is relaxed to find the final state of the molecule Ψ_{AB} with the energy E_{AB}. Due to orbital mixing, the energy lowers which can be identified as the covalent contributions to the chemical bond as ΔE_{Orb} (Eq. 4.7) [64].

$$\Delta E_{Orb} = E_{AB} - E_{AB}^0 \tag{4.7}$$

All three of these interactions can then be summed together to find the total interaction energy ΔE_{int} (Eq. 4.8).

$$\Delta E_{int} = \Delta E_{elstat} + \Delta E_{Pauli} + \Delta E_{Orb} \tag{4.8}$$

Note that ΔE_{Orb} can be further decomposed into the contributions from orbitals that belong to differing irreducible representations, but this is beyond the scope of this thesis.

4.2 Popular Methods

Other methods of EDA have been developed since. One popular method is the Absolute Localized Molecular Orbital (ALMO) method. This method avoids spin contamination, which is found in the original method due to overlapping regions of the frozen wave functions. ALMO also evaluates energy lowering due to polarization whilst prohibiting charge transfer and can separate forward and back donation in the charge transfer energy, both of which make ALMO ideal for determining interaction in metal complexes[65].

Another popular method is Symmetry Adapted Perturbation Theory (SAPT). SAPT provides a means of directly computing noncovalent interaction energy between two molecules without computing the total energy of the monomers or dimers. SAPT treats interaction energy as a perturbation on the isolated fragments which is based on the wave functions of the monomers. This allows SAPT to obtain accurate interaction energies in terms of electrostatic, induction, dispersion, and exchange-repulsion terms. SAPT also works best for weakly interacting monomers[66]. DFT-SAPT can be used to apply SAPT to larger systems, and empirical dispersion corrections and exchange-dispersion terms have been proposed to lower the cost of this method for very large systems [67].

The final method that will be discussed in this thesis is Local Energy Decomposition (LED) analysis. However, this method will be discussed at greater length and detail in Chapter 5.

4.3 Manual EDA and Testing Functionals

4.3.1 Methodology

This analysis can also be done manually, although not to the same degree. Using the POCB cluster model discussed in Chapter 3, single point energy calculations were done to find the energy interactions between fragments using three different functionals as preliminary analysis prior to using other methods. For this section, Figure 24 will be used as a reference and the models range in size from two to six monomer units in length. The energy of the following structures was found and used for analysis:

- **POCB Chain**: A single chain of POCB in space, half of section A in Figure 24
- **POCB-POCB**: Two POCB chains interacting with the chains being directly side by side, full section A in Figure 24
- **POCB Stacked**: Two POCB chains interaction but the chains are staggered in the Z dimension, full section C in Figure 24
- **POCB-Water**: A chain of POCB interacting with a chain of water molecules, full section B in Figure 24
- **POCB-Water-POCB**: A chain of water molecules running between two parallel POCB chains, a combination of the bottom half of section A and the full section B in Figure 24
- **Water Chain**: A chain of water molecules alone in space, section D and E in Figure 24
- **System**: The full cluster model

The energies were also analyzed to determine the following interactions defined by equations 4.9 - 4.11:

- **Water HBonds**: The hydrogen bonding occurring between water molecules in the water chain (Eq. 4.9)
- **HBonds**: The hydrogen bonding between one POCB chain and one water chain (Eq. 4.10)
- **Dispersion**: The forces between two POCB chains (Eq. 4.11)

$$E_{WaterHBonds} = E_{WaterChain} - E_{WaterMolecule} * n \qquad (4.9)$$

$$E_{HBonds} = E_{Water-POCB} - E_{WaterMolecule} * n - E_{POCB} - E_{WaterHBonds} \qquad (4.10)$$

$$E_{Disp} = E_{POCB-POCB} - 2 * E_{POCB} \qquad (4.11)$$

Where n is the number of water molecules present in the chain.

The functionals chosen for testing were B3LYP, ωB97X, and DLPNO-CCSD(T). B3LYP was chosen due to its wide use and was hypothesized to be a good overall starting point to capture and model the general trends of the intermolecular forces in these hydrates[68]. ωB97X was chosen for its ability to capture long range interactions. Theoretically, ωB97X would capture any interactions B3LYP missed, and a significant difference in results would suggest the existence of long range interactions[69]. The final functional chosen is due to its importance in the EDA method of choice, Local Energy Decomposition (LED). DLPNO-CCSD(T) is an approximation of CCSD(T), which is often considered the gold standard of quantum chemistry calculations [70]. Since it is an approximation, benchmarking DLPNO against other common methods was done to build confidence that the LED calculations would be accurate.

4.3.2 B3LYP

In Figure 25, the total energy of each structure per monomer unit is shown. All energies seem to be converging as the number of monomer units increase, and most of the structures follow the same trends. The raw data does not decompose the energy down to invidudally defined interactions, but it does demonstrate which fragments contain the most overall energy. In this case, the two fragments with the highest individual energies are that of the POCB Stacked and the POCB-Water-POCB conformations. This is an interesting result, considering the latter makes sense to be in this spot, but the former does not. It has the

most atoms of any fragment and captures most of the suspected intermolecular interactions. The POCB Stacked conformation, however, should be the same as its POCB-POCB counterpart due to the structure only differing in orientation. This result suggests that the Stacked fragment has more intermolecular interactions than that of side-by-side POCB.
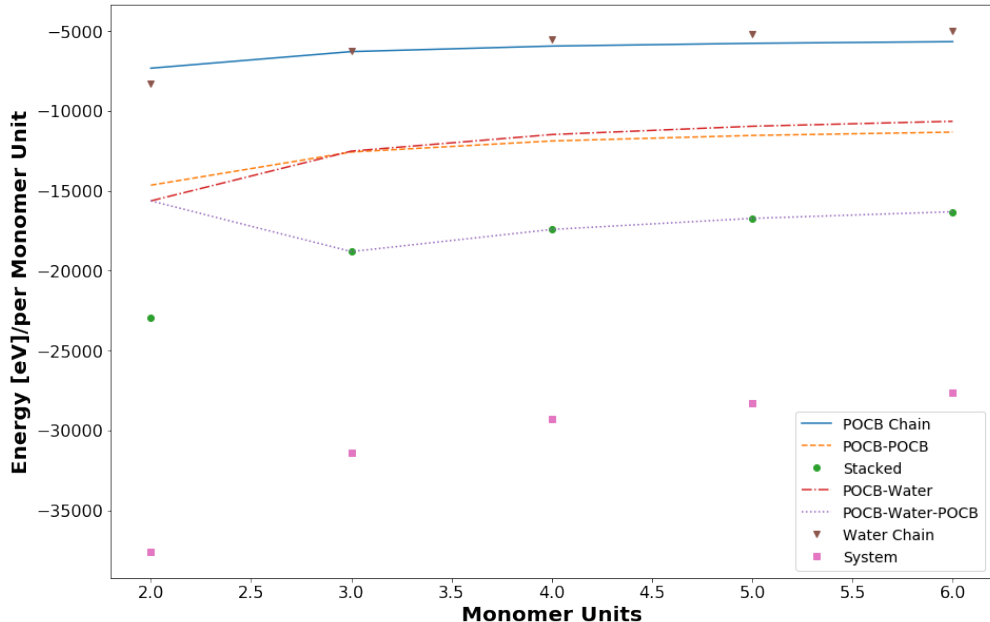
Figure 25: Single point energies of all structures as the number of monomer units increase using the B3LYP functional

Figure 26 shows the calculated interactions energies defined above. The data confirms the hypothesis that hydrogen bonding is the primary driving force in the formation of these hydrates. Dispersion forces play a much lower role than anticipated, having a seemingly negligible impact in holding the structure together. The hydrogen bonding is dominated by the hydrogen bonds formed between water molecules themselves. However bonding between water molecules and the neighboring polymers is not an insignificant interaction, still being approximately 33% the strength of the water-water interactions.

The B3LYP data suggests that dispersion forces have a negligible impact on the formation of POCB hydrates. It also suggests that hydrogen bonding between the water molecules and polymer chains plays a significant role in the formation of said hydrates, with the hydrogen bonding between two water molecules still being the dominant force. This is in

43

agreement with expectations for a clathrate hydrate, and therefore it seems reasonable that these hydrates would exhibit similar behavior.
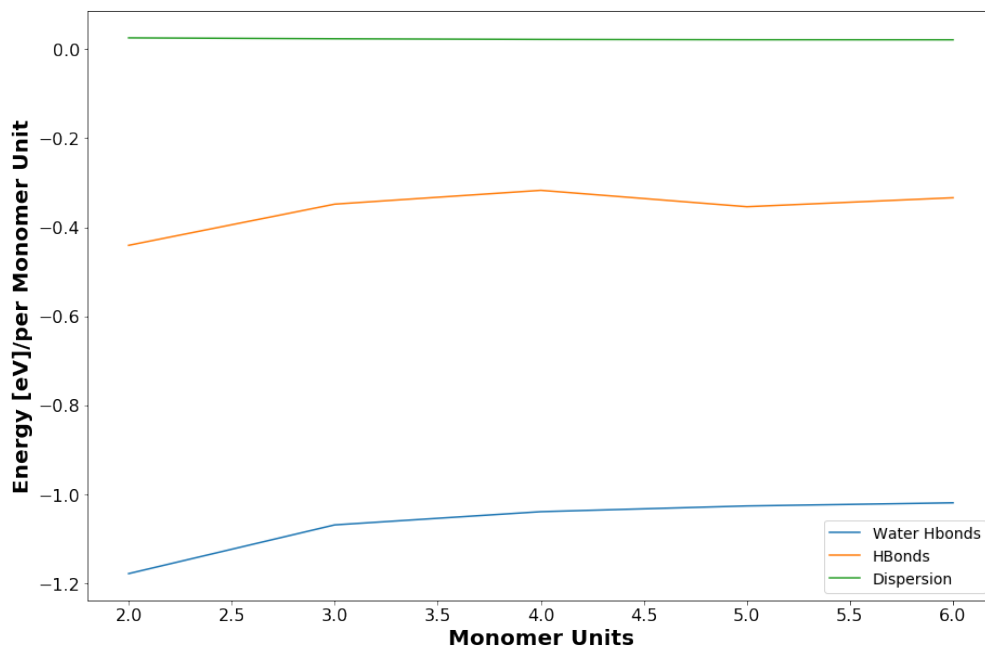
Figure 26: Calculated interaction energies of all structures as the number of monomer units increase using the B3LYP functional

4.3.3 ωB97X

Both the raw data and the calculated data show similar behavior to that of B3LYP. The raw data (which can be seen in Appendix B) is nearly identical to that of B3LYP, showing the same trends, similar values, and the same order of interactions from weakest to strongest. Figure 27 is also similar to that of its predecessor. Once again, the POCB-water hydrogen bonds are   33% the strength of water-water hydrogen bonds. Dispersion is still negligible in comparison, but it does demonstrate a trend of these forces getting stronger as monomer units increase. It is possible that ωB97X captured some long-range dispersion interactions not captured by B3LYP, and these interactions grow in size to be slightly more influential as the polymer length increases.
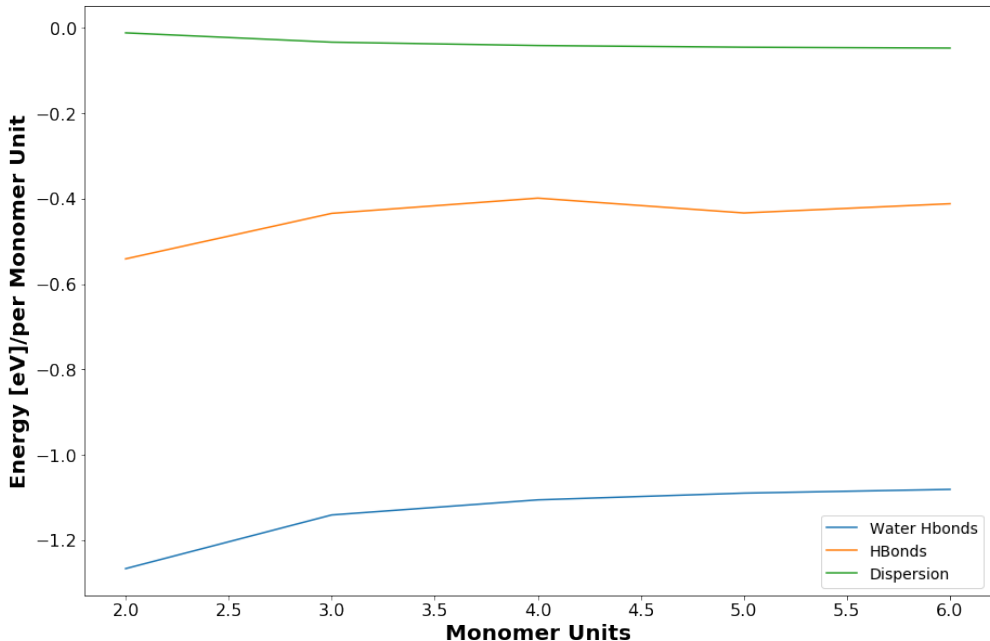
Figure 27: Calculated interaction energies of all structures as the number of monomer units increase using the ωB97X functional

4.3.4 DLPNO-CCSD(T)

DLPNO does not necessarily tell the same story. The raw data (Appendix B) looks similar to the previous functionals, but the calculated data in Figure 28 differs from the others. The trends are overall flatter, the energy not changing as significantly as the polymer length increases. The numerical energy values have also shifted towards zero, with the interactions being shown weaker. However, the ratios of these interactions remain similar to the other functionals. While DLPNO is the only dissenting data of the three functionals, its ability to still capture the ratios of the interactions correctly indicates it is accurate for the purposes of this thesis, and there is confidence in the LED results.
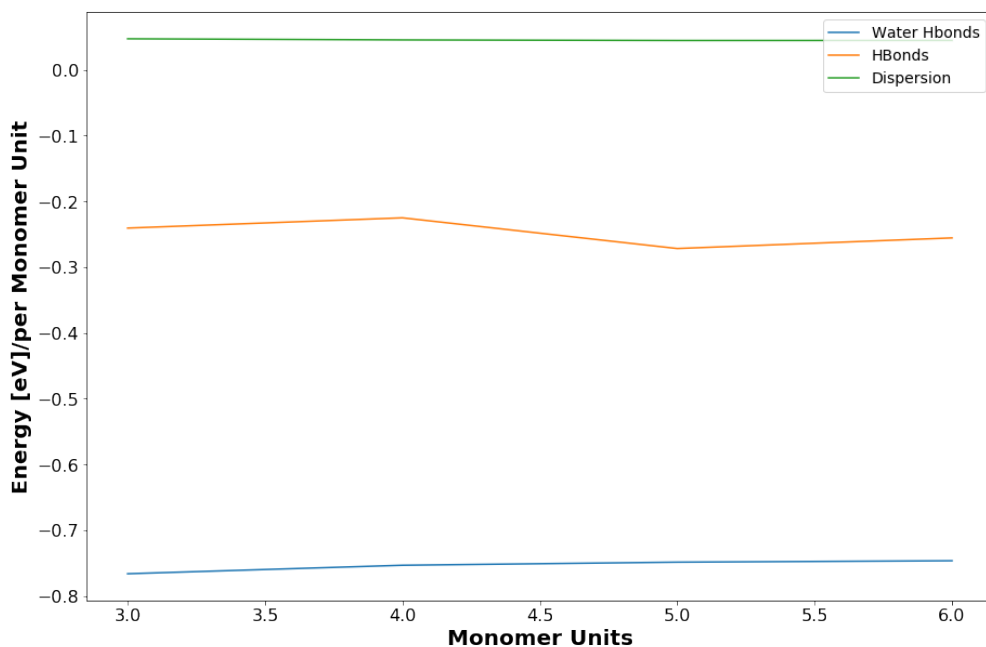
Figure 28: Calculated interaction energies of all structures as the number of monomer units increase using the DLPNO-CCSD(T) functional

5.0   Local Energy Decomposition (LED)

5.1   The Theory Behind LED

LED is a method that allows for analysis of decomposed domain-based local pair natural orbitals (DLPNO) energies into physically meaningful contributions such as electrostatic interaction, interfragment exchange, and dispersion forces.

In order to fully understand LED, DLPNO-CCD(T) must be briefly touched on. In this approach, the occupied orbital of the reference Hartree-Fock (HF) determinant are initially localized. Then the correlation energy (E_C) is expressed as a sum of electron pair correlation energies. These are represented by ϵ_{ij} where i and j are the occupied HF orbitals, which can be seen in Eq. 5.1.

$$E_C = 2\Sigma_{i,a_{ij}} F_{i,a_{ij}} t_{a_{ij}}^i + \Sigma_{i>j}\epsilon_{ij} + E^{(T)} \tag{5.1}$$

where the first term includes contributions from single excitation and vanishes assuming Brillouin's theorem is satisfied. The second term is the pair natural orbital (PNO) approximation, where ϵ_{ij} can be further expressed as Eq. 5.2.

$$\epsilon_{ij} = \Sigma_{a_{ij},b_{ij}}(ia_{ij}|jb_{ij})\tau_{a_{ij},b_{ij}}^{ij} \tag{5.2}$$

In which a and b are PNOs that belong to pair ij, the first term is the two electron integral in Mulliken notation, and τ is the cluster amplitudes in the PNO basis. τ can be further broken down into coupled cluster equations and different amplitudes, but that is beyond the scope of this thesis.

It can be shown that pair correlation energies decay very quickly with distance R_{ij} between the centers of i and j. This allows large amounts of weak pairs that have negligible contributions to the correlation energy to be ignored in the CCSD calculations. Instead,

rather, these pairs are treated with second order perturbation theory, where their overall contribution to the correlation energy is found as $E_C - WP$. The remaining pairs, or strong pairs, are treated according to the CCSD method, with their overall correlation energy denoted as $E_C - SP$[71].

Having understood this, LED can now be described. LED uses a supermolecular approach in which the D_e of two interacting molecules (A and B) is computed as the difference between the total energy of system AB and the sum of the energy between an infinitely separated A and B. The counterpoise corrections of Boys and Bernardi are used to account for the shortcomings of a finite basis set. Combining all of this, Eq. 5.3 expresses D_e.

$$D_e = E_{AB}^{AB}(AB) - [E_A^A(A) + E_B^B(B)] - [E_A^{AB}(AB) - E_A^{AB}(A) + E_B^{AB}(AB) - E_B^{AB}(B)] \quad (5.3)$$

In which the notation $E_X^Y(Z)$ shows the energy of X calculated at the equilibrium geometry of Y with the basis set of system Z. The first term denotes the uncorrected D_e and features the optimized geometries of the isolated molecules. The second term is the counterpoise correction for basis set superposition error, where the monomers are calculated at dimer equilibrium geometry with the dimer basis set. These energy terms can be rearranged into monomer and dimer calculations, allowing the D_e to be reduced to:

$$D_e = \Delta E_{int} + \Delta E_{geo-prep} \quad (5.4)$$

where the first term is the dimer calculations and the second term is the monomer calculation. Through this rearrangement, the counterpoise corrected D_e decomposes into an electronic interaction part, ΔE_{int} and a geometric preparation part, $\Delta E_{geo-prep}$. The latter is the energy contributions from the geometrical distortion of A and B from their optimal monomer geometries to the geometry during the interaction.

The electronic interaction term can be further decomposed into:

$$\Delta E_{int} = \Delta E_{int}^{HF} + \Delta E_{int}^C \quad (5.5)$$

48

where the first term accounts for the electrostatic interaction between monomers, polarization effects, and donor-acceptor interactions. The second term corrects the above components and accounts for disperse attraction resulting from dipole-dipole interactions. The first term can be even further partitioned into electrostatic and exchange interactions directly, as seen in Eq. 5.6 and Eq. 5.7[71].

$$\Delta E_{elstat}^{(A,B)} = P_{A\leftrightarrow B}[\Sigma_{X_A>Y_B} \frac{Z_X^{(A)} Z_Y^{(B)}}{|R_X^{(A)} - R_Y^{(B)}|} - 2\Sigma_{i_A, X_B} \langle i_A| \frac{Z_X^{(B)}}{|r_i^{(A)} - R_X^B|} |i_A\rangle + 4\Sigma_{i_A>i_B}(i_A i_A|j_B j_B)]$$

(5.6)

where the first and third terms are always repulsive, while the second term is always attractive.

$$\Delta E_{exch}^{(A,B)} = P_{A\leftrightarrow B}[-2\Sigma_{i_A>i_Y}(i_A j_B|i_A j_B)]$$

(5.7)

where the intermolecular exchange is always negative, representing a stabilizing component of the interaction that lowers repulsion between electrons of the same spin[72].

The previously mentioned weak and strong pair contributions are also accounted for in the decomposition and reported alongside the other contributions at the end of the simulations. LED also has further capabilities such as accounting for charge transfer, polarization, and other interactions[71]. However, this further theory is beyond the scope of this work.

5.2 Methodology

LED was used to breakdown the interaction energies in these hydrates, and as discussed in Chapter 3, cluster models had to be made to accomplish this. The cluster models, however, differ from those in Chapter 4, and each hydrate is broken into the following structures:

- **Polymer-Polymer**: interactions between two polymer chains
- **Polymer-Water**: interactions between one polymer chain and one water chain
- **Water-Water**: Interactions between water molecules in a chain

These more simplified structures capture the same information as before, with less overall calculations.

5.3   POCB Decomposition

For the purposes of this thesis, all acquired plots will be shown for POCB. For all other structures, raw data plots will be available in Appendix B, and the important final point will be referenced in tables within the text.

In POCB, Polymer-Polymer interactions were found to be negligible, as seen in Figure 29. No singular interaction was much stronger than the others, and trends were fairly flat. The energy contributions of the polymers interacting with one another are negligible.
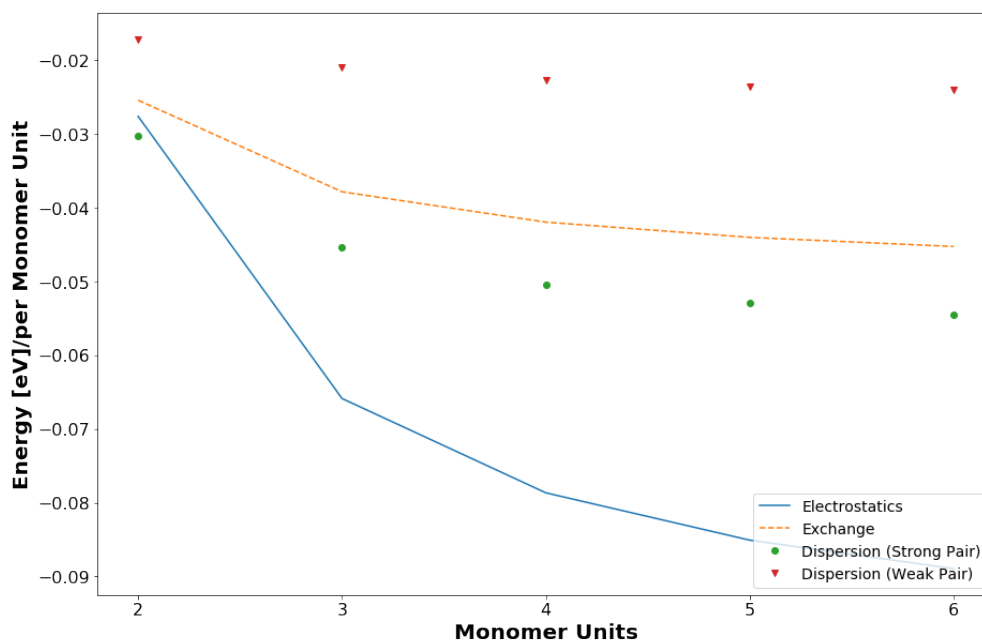
Figure 29: LED data of Polymer-Polymer interactions in POCB as the number of monomer units increase. Note the smaller scale

To directly compare this with the manual EDA results, Polymer-Polymer interactions were defined as dispersive interactions, and were found to be negligible, which is supported

by these results.

Figure 30 shows the POCB-Water interactions. Electrostatics, which contains the hydrogen bonding energy, is dominant over the other interactions. However the other interactions are not necessarily negligible, with the exchange energy standing out as about 18% of the electrostatic energy. The dispersion contributions are weaker, but also not entirely negligible. The fact that forces besides hydrogen bonding are significant in forming these hydrates is unexpected, as the manual EDA suggested hydrogen bonding to be the only force present.
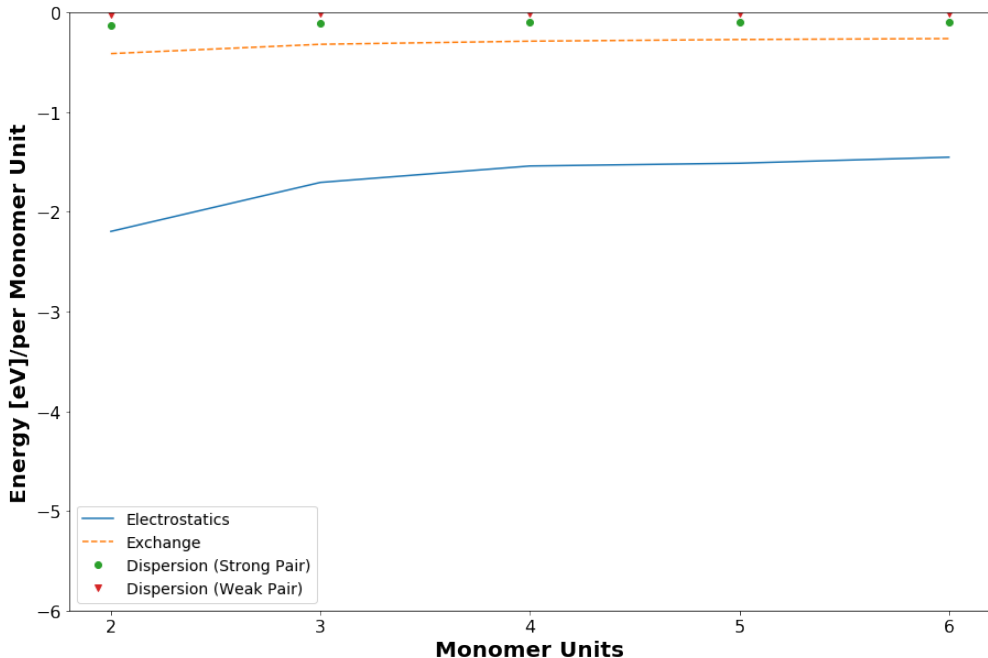
Figure 30: LED data of Water-Polymer interactions in POCB as the number of monomer units increase

The Water-Water interactions shown in Figure 31 tell a similar story. Hydrogen bonding is dominant, as expected. The dispersion forces are negligible however, but once again the exchange contribution is still present. Whilst it is much weaker, by the sixth monomer unit it is still $\sim 10\%$ the strength of the electrostatic interactions, and therefore cannot be discounted completely.

An unexpected development is that the POCB-Water electrostatics are much stronger
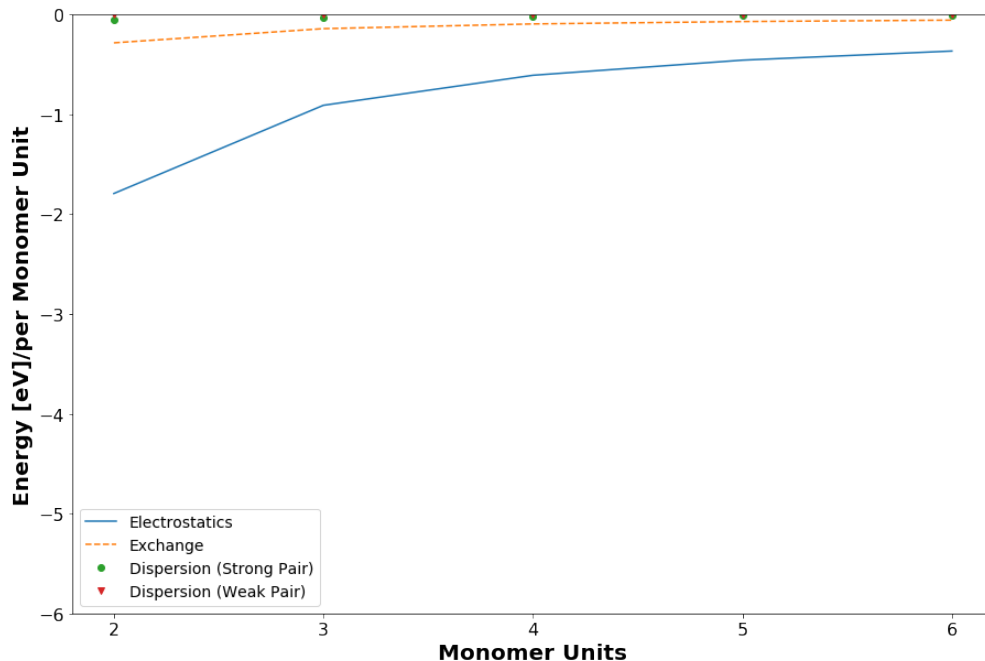
Figure 31: LED data of Water-Water interactions in POCB as the number of monomer units increase

than the Water-Water interactions. When directly compared in Figure 32, the POCB-Water interactions are always stronger than the Water-Water interactions, and the gap only widens as the polymer length increases. By the sixth monomer unit, the Water-Water interactions are $\sim 25\%$ the strength of the POCB-Water interactions, which directly contradicts the manual EDA, which suggests that the POCB-Water interactions are only $\sim 33\%$ as strong as the Water-Water interactions! This contradiction is interesting and raises questions about the manual EDA and if it actually captured all the possible interactions and the validity of those calculations. LED is predicting much stronger interactions than the manual EDA did as well.
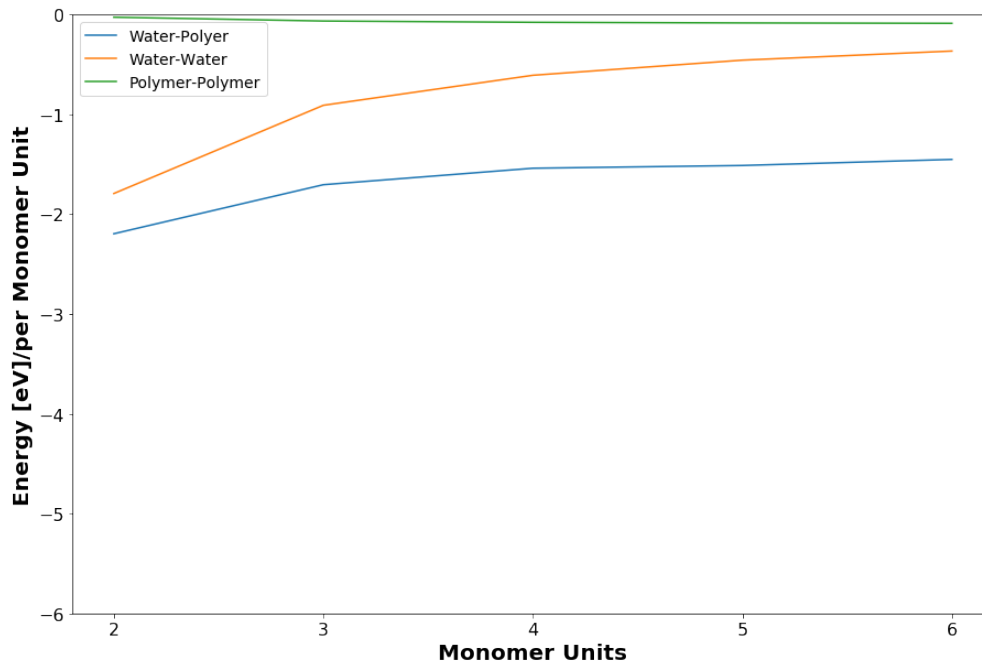
Figure 32: Electrostatic interactions in POCB from each source of interactions compared

Comparing the exchange energies in Figure 33 is also interesting. The interactions between POCB and water is still dominant, with the exchange energy of this fragment being seemingly non-size dependent. The exchange energies of the other fragments seem to get closer to zero as polymer length increases, but the steady exchange energy of the POCB-Water fragment suggest it does have a significant role in forming these hydrate structures, but only in that interaction. Exchange in the other two fragments seems to be negligible, especially as polymer length increases. Therefore it must be concluded the electrons between POCB and water have a relatively strong interaction that helps drive the formation of the hydrate crystal and hold it together.

Table 2 shows the numerical difference between each energy contribution of each structure. For the following structure, tables will be used rather than plots for the raw data shown in the first three figures of this section.
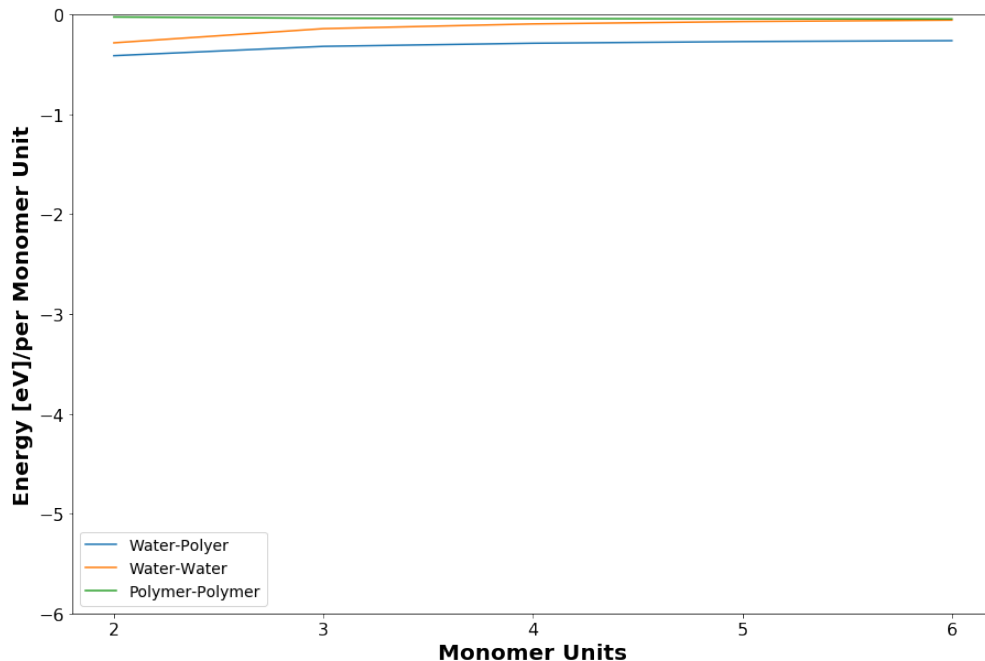
Figure 33: Exchange interactions in POCB from each source of interactions compared

Table 2: Calculated energies for each POCB fragment at a final length of six monomer units. All units are in eV

	Electro	Exch	Disp. WP	Disp. SP	Non-Disp.	Binding
POCB-POCB	-0.09	-0.05	-0.02	-0.05	-37.56	-0.04
POCB-Water	-1.45	-0.26	-0.01	-0.10	-32.82	-0.28
Water-Water	-0.37	-0.06	-0.01	0.00	-14.04	-0.63

5.4   PEI Decomposition

5.4.1   Hemihydrate

The hemihydrate is unique amongst these structures because it has no Water-Water in-teractions. This leaves the Polymer-Water and Polymer-Polymer interactions needing to be

stronger for this structure to form. Table 3 shows that the PEI-PEI interactions are still close to negligible. The PEI-Water interactions however are stronger, the electrostatics in particular are stronger than that of the POCB-Water electrostatics. The exchange contributions are also slightly higher in PEI-Water than its counterpart in POCB. Overall, the PEI-PEI interactions are also significantly weaker than that of the POCB-POCB interactions.

Table 3: Calculated energies for each hemihydrate fragment at a final length of five monomer units. All units are in eV

	Electro	Exch	Disp. WP	Disp. SP	Non-Disp.	Binding
PEI-PEI	-0.01	0.00	-0.02	-0.01	-26.95	-0.11
PEI-Water	-1.52	-0.30	-0.01	-0.08	-21.19	-0.37
Water-Water	0.00	0.00	0.00	0.00	–	0.00
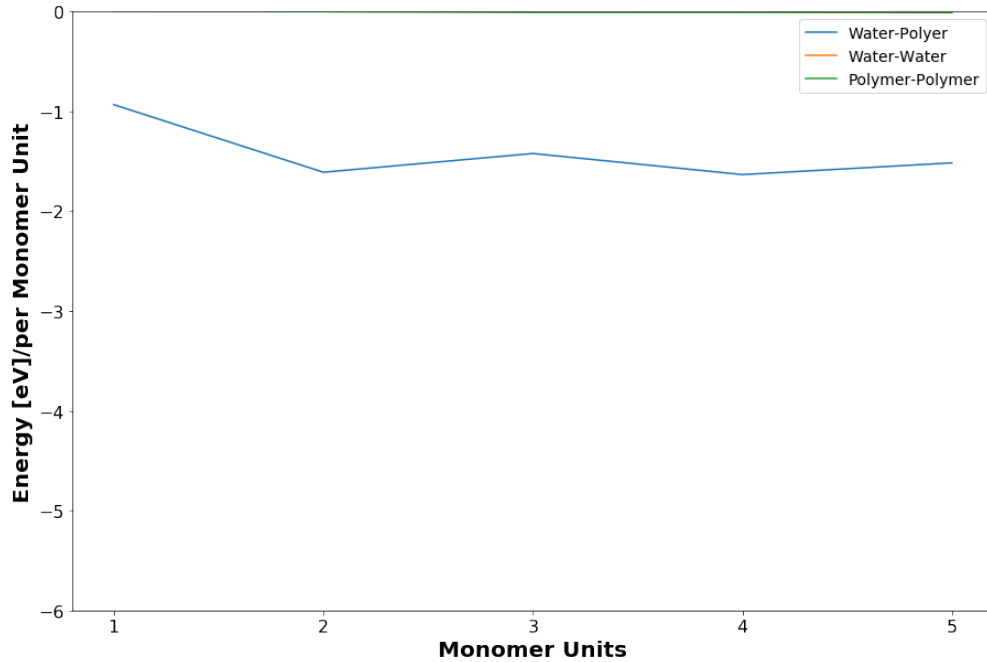
Figure 34: Electrostatic interactions in the hemihydrate from each source of interactions compared

This leaves the only strong interactions to occur in the PEI-Water fragment. As seen in Figure 34 the electrostatic contributions are only significant in PEI-Water interactions.

The PEI-PEI interactions are completely negligible, in this case leaving the majority of the contributions that form this hydrate to the hydrogen bonding between the polymer and the water.
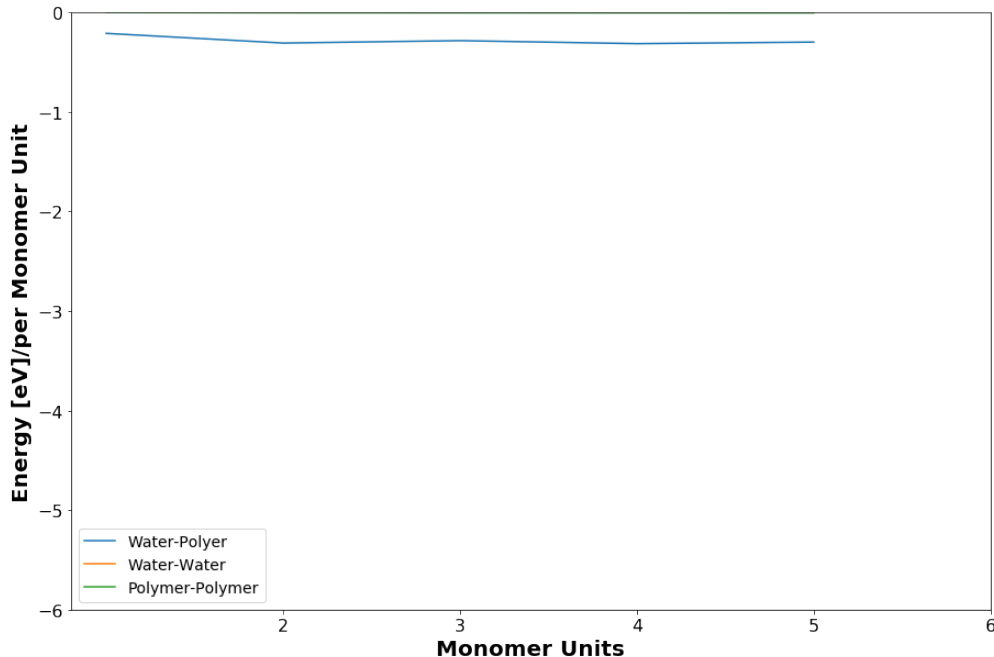
Figure 35: Exchange interactions in the hemihydrate from each source of interactions compared

Figure 35 tells the same story. The exchange interactions are only coming from the PEI-Water fragment, with the PEI-PEI fragment having negligible contributions. This confirms that in the hemihydrate, only the interactions between the PEI and water have any impact on the formation of the structure. More so, the exchange contribution is only $\sim 20\%$ the strength of the electrostatic interaction, demonstrating that in this case the hydrogen bonding between the PEI and the water molecules is the primary driving force for the formation of the crystal.

5.4.2 Sesquihydrate

The sesquihydrate is more similar to POCB than the hemihydrate. The sesquihydrate actually has the strongest interactions so far across all interaction types as seen in Table 4.

For instance, the PEI-PEI electrostatic interactions are nearly four times larger than that of the hemihydrate, and the PEI-Water electrostatic interactions are nearly five times higher than that of POCB or the hemihydrate! Water-Water electrostatics are similar to that of POCB, but still slightly stronger as well.

Table 4: Calculated energies for each sesquihydrate fragment at a final length of six monomer units. All units are in eV

	Electro	Exch	Disp. WP	Disp. SP	Non-Disp.	Binding
PEI-PEI	-0.04	-0.01	-0.02	-0.02	-26.71	-0.10
PEI-Water	-5.29	-0.96	-0.02	-0.22	-25.14	-0.32
Water-Water	-0.42	-0.06	0.00	-0.01	-11.79	-0.43
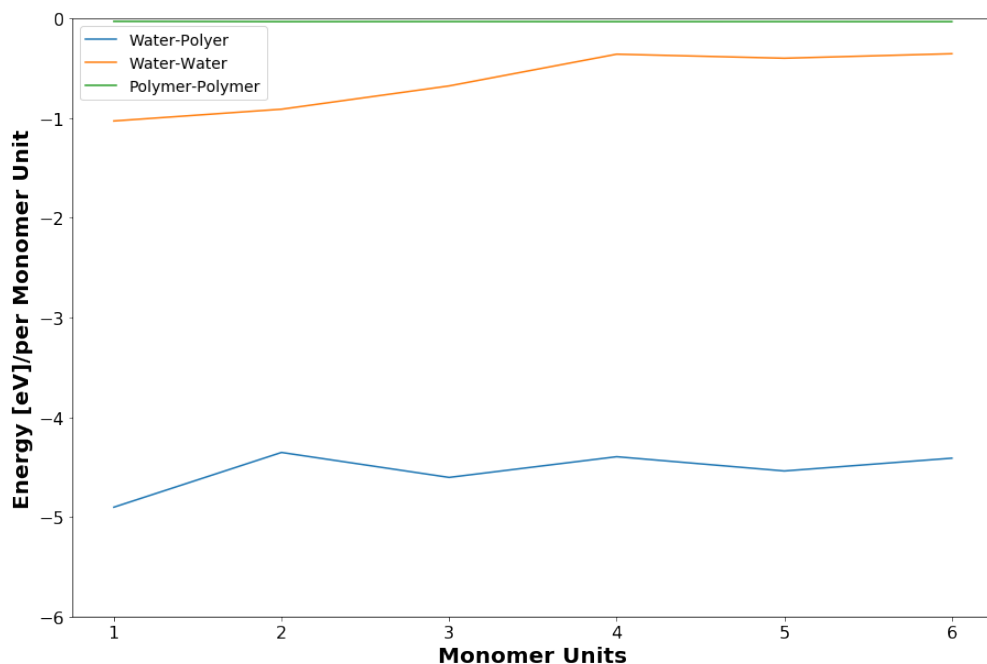
Figure 36: Electrostatic interactions in the sesquihydrate from each source of interactions compared

The same story is told by the exchange and dispersion contributions as well. Dispersion energies overall though are still negligible, with the primary forces once again falling to hy-

drogen bonding and exchange contributions.

Figure 36 shows just how strong the PEI-Water and Water-Water interactions are. Once again, the Polymer-Water interactions are much stronger than the Water-Water interactions, and the Water-Water interactions get weaker as polymer length increases. The Water-Water electrostatics are only $\sim 8\%$ the size of the PEI-Water interactions, which is much larger in POCB. In PEI, the Water-Water interactions seem to play much less of a role in the formation of the structure than they did in POCB.
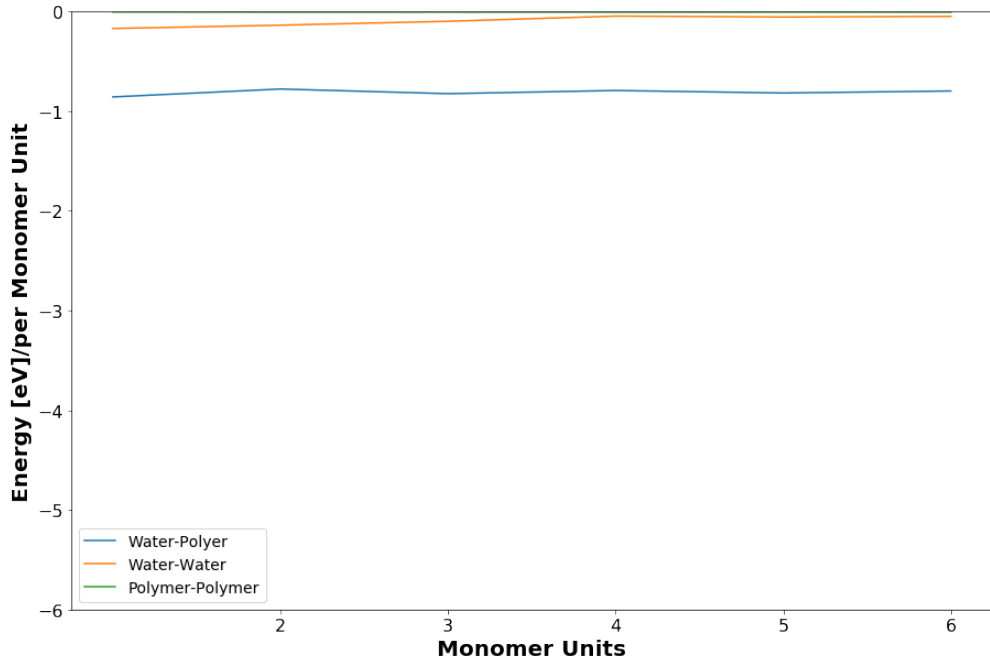
Figure 37: Exchange interactions in the sesquihydrate from each source of interactions compared

Figure 37 shows the same as Figure 33 shows for POCB. The Polymer-Water exchange energy is dominant, and not size dependent while the other exchange energies are nearly negligible at the final polymer length. The exchange contribution is $\sim 18\%$ as large as the electrostatic contribution, which is very similar to the ratios of the other structures. The ratio of exchange energy to electrostatic energy is a seemingly important trend across the structures.

5.4.3 Dihydrate

The dihydrate is most similar to the sesquihydrate because it has high interaction energies across the board, being the highest in everything except PEI-Water electrostatic interactions, as seen in Table 5. Its unique feature is that it has the highest Polymer-Polymer interaction energies.

Table 5: Calculated energies for each dihydrate fragment at a final length of six monomer units. All units are in eV

	Electro	Exch	Disp. WP	Disp. SP	Non-Disp.	Binding
PEI-PEI	-0.13	-0.06	-0.02	-0.06	-26.78	-0.07
PEI-Water	-5.23	-0.97	-0.04	-0.29	-40.38	-0.62
Water-Water	-0.82	-0.15	0.00	-0.03	-11.92	-0.10
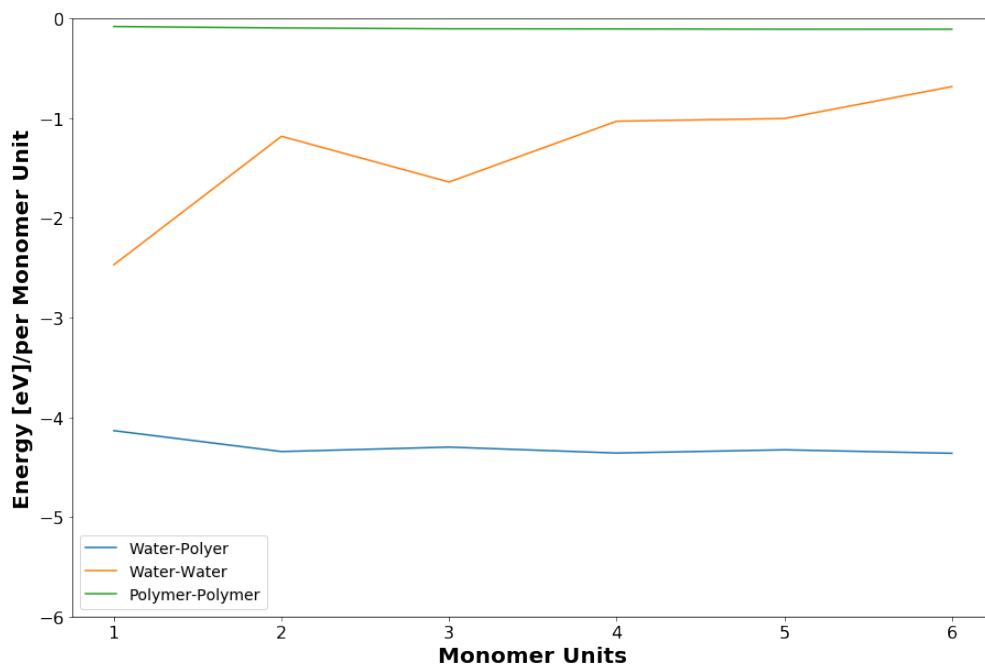
Figure 38: Electrostatic interactions in the dihydrate from each source of interactions compared

The electrostatic energy of the PEI-PEI fragment is no longer negligible, amounting to

about 1% of the PEI-Water interactions. The dispersion forces are still negligible as before across all fragments. Similarly, in Figure 38, the PEI-Water interactions are the highest, although in this system these interactions are seemingly not as size dependent. The Water-Water interactions do lower as the polymer increases in length, but in a much less smooth fashion as well. The largest difference is the presence of the PEI-PEI electrostatic energy that could perhaps have a small impact on how the structure forms.
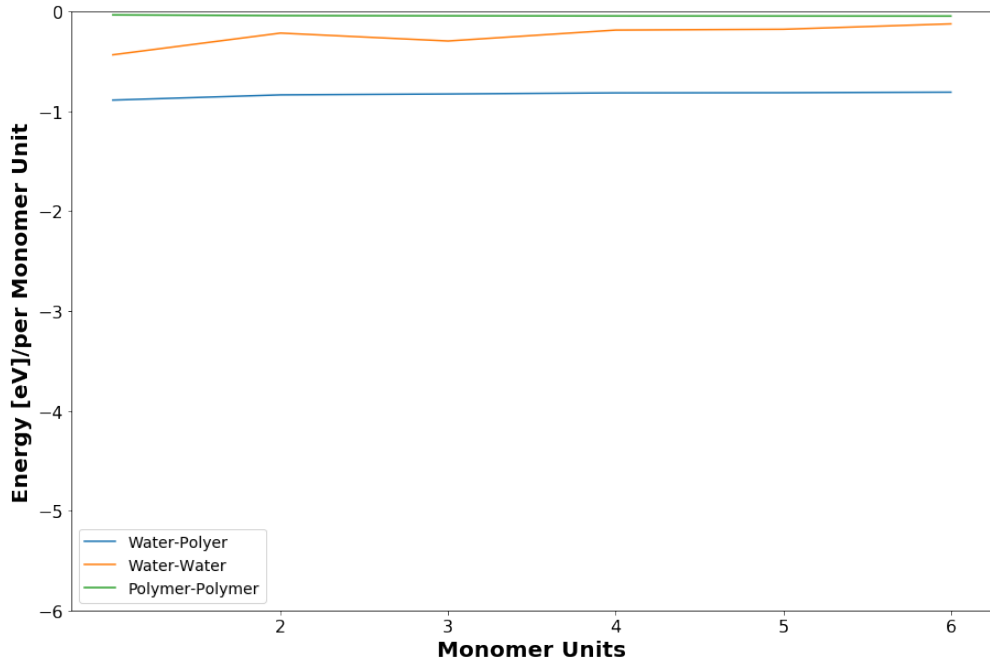
Figure 39: Exchange interactions in the dihydrate from each source of interactions compared

The dihydrate behaves similarly to the others in terms of exchange interactions, as seen in Figure 39. A non-size dependent interaction of Polymer-Water interaction, a weakening Water-Water interaction, but most importantly, a ratio of exchange contributions to electro-static contributions in the PEI-Water fragment of 18%. Across all four structures, that ratio has remained the same, and can possibly be seen as a descriptor of these hydrate structures that can be used to screen chemical space.

5.5 Atom Replacements

5.5.1 Oxygen Insertion

To better understand the formation of these structures, certain key atoms were replaced to examine the impact it would have on the energy and formation of the crystals. This was done for the hemi and sesquihydrates, where a single nitrogen atom in both structures was replaced with an oxygen atom in a singular chain, which are visible in Figures 40 and 41 respectively. The geometries were optimized as described in Chapter 3, made into cluster models, and analyzed via LED.
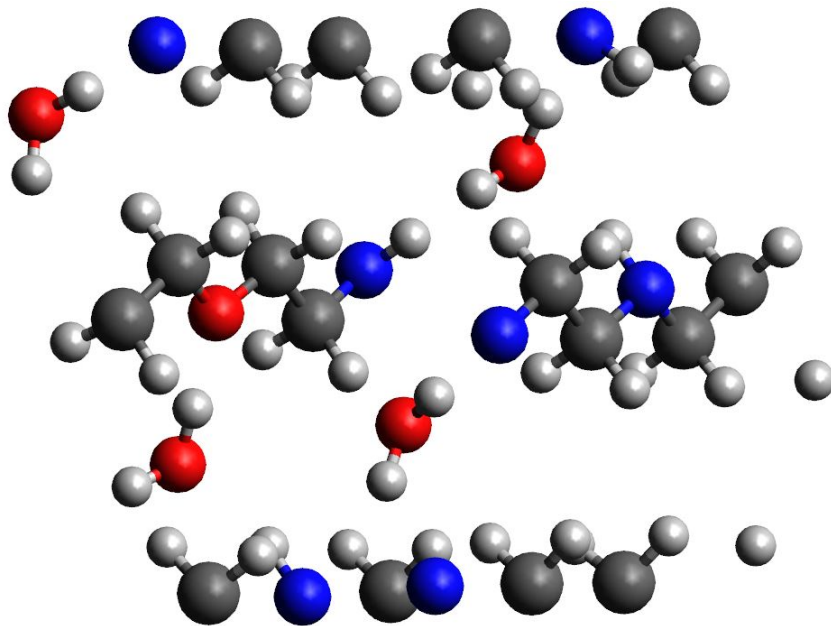
Figure 40: Periodic unit cell of the PEI hemihydrate doped with an oxygen atom in place of a nitrogen on one chain

For the hemihydrate the addition of the oxygen drastically increased the interactions of PEI-Water fragment. The electrostatic and exchange energies in particular increased in value significantly as seen in Table 6. This change implies that replacing a nitrogen with an oxygen improves the amount of interactions occurring in this fragment. This theoretical hydrate had an exchange to electrostatic interaction ratio of /sim19% which is the same as
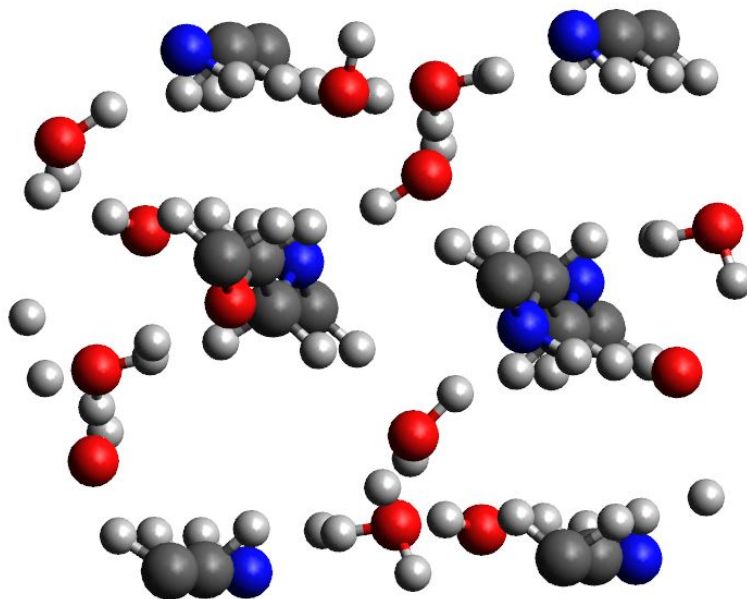
Figure 41: Periodic unit cell of the PEI sesquihydrate doped with an oxygen atom in place of a nitrogen on one chain

Table 6: Calculated energies for each oxygen doped hemihydrate fragment at a final length of six monomer units. All units are in eV.

	Electro	Exch	Disp. WP	Disp. SP	Non-Disp.	Binding
PEI-PEI	0.00	0.00	-0.02	-0.01	-26.75	–
PEI-Water	-2.10	-0.41	-0.01	-0.12	-19.27	–
Water-Water	0.00	0.00	0.00	0.00	–	–

the normal hemihydrate. This is an indicator that this hydrate is realistic and could possibly be synthesized.

The sesquihydrate experienced a very different effect from the addition. In Table 7 it can seen that the electrostatic interactions of the PEI-Water decreased by about 1.5 eV, and

the exchange energy dropped by about 0.2 eV. The PEI-PEI interactions however got much stronger. While the total interactions in PEI-PEI are still low comparatively, it is interesting that the oxygen had such an impact on the Polymer-Polymer interactions. This structure also has the most different ratio, with the exchange contributions of the PEI-Water fragment being $\sim 20\%$. The change to the ratio, as well as the much more dramatic impact on the PEI-PEI interactions makes this theoretical hydrate seem less realistic than its counterpart. However, it is still close and possible that this structure can exist, but it will be weaker than that of the other hydrates studied.

Table 7: Calculated energies for each oxygen doped sesquihydrate fragment at a final length of six monomer units. All units are in eV

	Electro	Exch	Disp. WP	Disp. SP	Non-Disp.	Binding
PEI-PEI	-0.26	-0.09	-0.02	-0.08	-26.82	–
PEI-Water	-3.46	-0.70	-0.02	-0.20	-29.24	–
Water-Water	-0.42	-0.06	0.00	-0.01	-11.79	–

5.5.2 Fluoridation

This time, rather than replacing a nitrogen, the polymers were fluoridated rather than hydrogenated, which is visible in in Figures 42 and 43. The same methods above were followed for this analysis, and once again done for the hemi and sesquihydrates.

Table 8 shows that the addition of fluorine to the system had a dramatic effect on the PEI-PEI interactions of the hemihydrate. Electrostatic and exchange interactions from this fragment are now much more present, although still fall being the electrostatic interactions of the PEI-Water fragment. This is the expected result, as the fluorine atoms are primarily interacting with one another and have closed the gap between polymer chains a bit. The ratio is also not the same, now being $\sim 25\%$.

Fluoridating the sesquihydrate had a similar effect to oxygenating it, but more extreme as seen in Table 9. The PEI-PEI interactions increased even more, and the PEI-Water interactions were weakened further. In this theoretical structure the PEI-PEI interactions
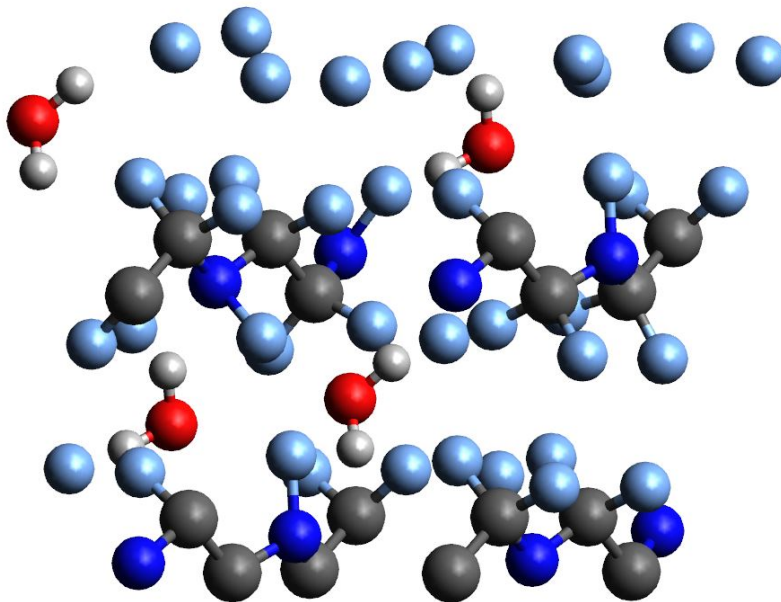
Figure 42: Periodic unit cell of the PEI hemihydrate after fluoridation

are just as important as the PEI-Water interactions, and while still not dominant, they are definitely now influencing the formation of the structure. The ratio for this structure is also 25%.

5.6 Binding Energy Calculations

5.6.1 Methodology

The binding energies were calculated using single point DLPNO-CCSD(T) calculations on the fragments in each cluster, as well as the full cluster. The energies are as follows:

- **Fragment Energy 1**: E_A
- **Fragment Energy 2**: E_B
- **Total Single Point Energy**: E_{tot}
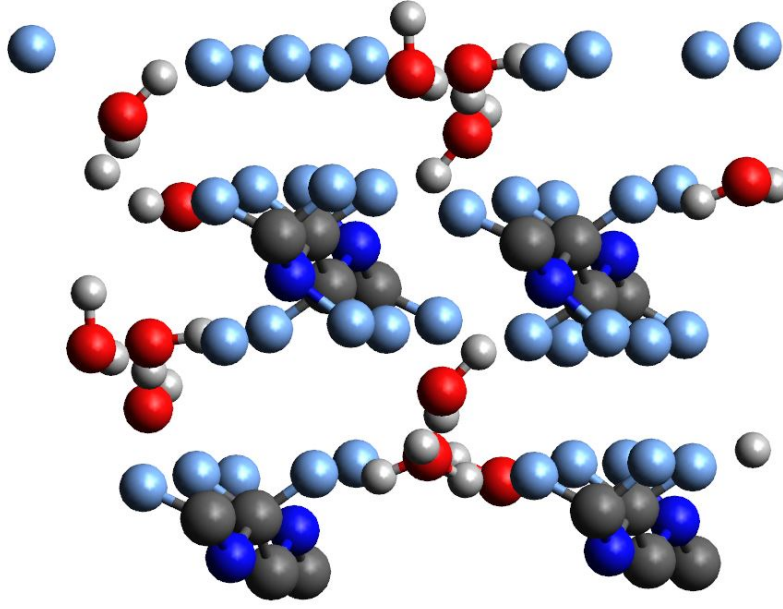
Figure 43: Periodic unit cell of the PEI sesquihydrate after fluoridation

Table 8: Calculated energies for each fluoridated hemihydrate fragment at a final length of five monomer units. All units are in eV.

	Electro	**Exch**	**Disp. WP**	**Disp. SP**	**Non-Disp.**	**Binding**
PEI-PEI	-0.74	-0.18	-0.05	-0.07	-78.42	-0.23
PEI-Water	-1.68	-0.43	-0.02	-0.12	-45.11	-0.07
Water-Water	0.00	0.00	0.00	0.00	–	0.00

The binding energy was calculated according to Eq. 5.8.

$$BE = E_{tot} - E_A - E_B \qquad (5.8)$$

Table 9: Calculated energies for each fluoridated sesquihydrate fragment at a final length of six monomer units. All units are in eV.

	Electro	Exch	Disp. WP	Disp. SP	Non-Disp.	Binding
PEI-PEI	-0.89	-0.21	-0.06	-0.07	-77.50	0.01
PEI-Water	-2.00	-0.50	-0.05	-0.18	-56.66	0.09
Water-Water	-0.42	-0.06	0.00	-0.01	-11.79	-0.43

5.6.2   Comparisons

The Polymer-Polymer fragment binding energies (BE), seen in Figure 44, are not entirely surprising. The BEs for all PEI hydrates are all around each other, with the POCB energy being only slightly weaker. The other two standouts are both the fluorine substituted fragments, with the fluoridated hemihydrate having the largest energy, but the fluoridated sesquihyrate has the weakest BE.

For the Polymer-Water fragment in Figure 45, a similar yet different story is told. The fluorine substituted structures still have the two weakest BEs. POCB is the next weakest, followed closely by the hemihydrate, then the sesquihydrate, and finally the dihydrate. These results are expected, due to the dihydrate and sesquihydrate having the most water molecules, having the most interactions is sensible. POCB having less interactions that the hemihydrate is suspect however, due the hemihydrate having a limited number of waters comparatively to POCB.

As seen in Table 11, the PEI hydrates increase in BE in the same order that hydrates in melting temperature. This data does suggest a correlation between BE and the melting temperature with the the Polymer-Polymer data helping to confirm that the correlation is dependent on the base polymer. Meaning that a higher BE does mean a higher melting point. The opposite is true for three of the four structures when total BEs are compared,

with the hemihydrate standing out as seen in Figure 46. This significant change is thought to be due to the lack of water-water interactions, but it does break the pattern established by the other crystals.

Table 10: Binding energies at the final polymer length compared to the experimental melting points for the Polymer-Polymer fragment

	Melting Temperature (C)	Binding Energy (eV)
POCB	14	–
POCB Hydrate	37	-0.04
PEI	75	–
Hemihydrate	60	-0.11
Sesquihydrate	80	-0.10
Dihydrate	110	-0.07
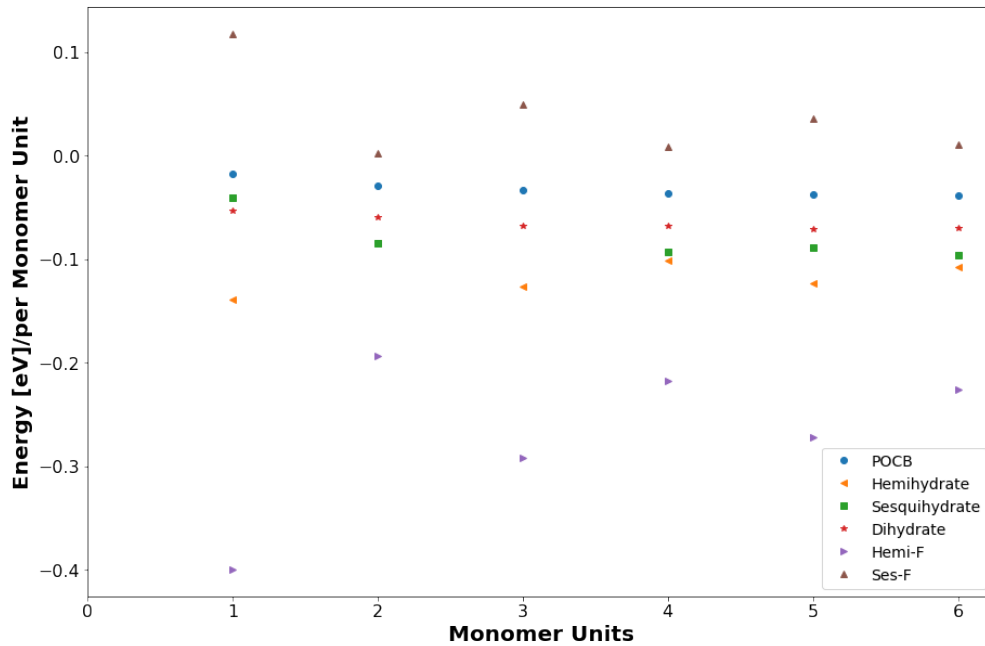
Figure 44: Binding Energies of all the hydrates as the number of monomer units increase for the Polymer-Polymer fragment

Table 11: Binding energies at the final polymer length compared to the experimental melting points for the Polymer-Water fragment

	Melting Temperature (C)	Binding Energy (eV)
POCB	14	–
POCB Hydrate	37	-0.28
PEI	75	–
Hemihydrate	60	-0.37
Sesquihydrate	80	-0.42
Dihydrate	110	-0.62
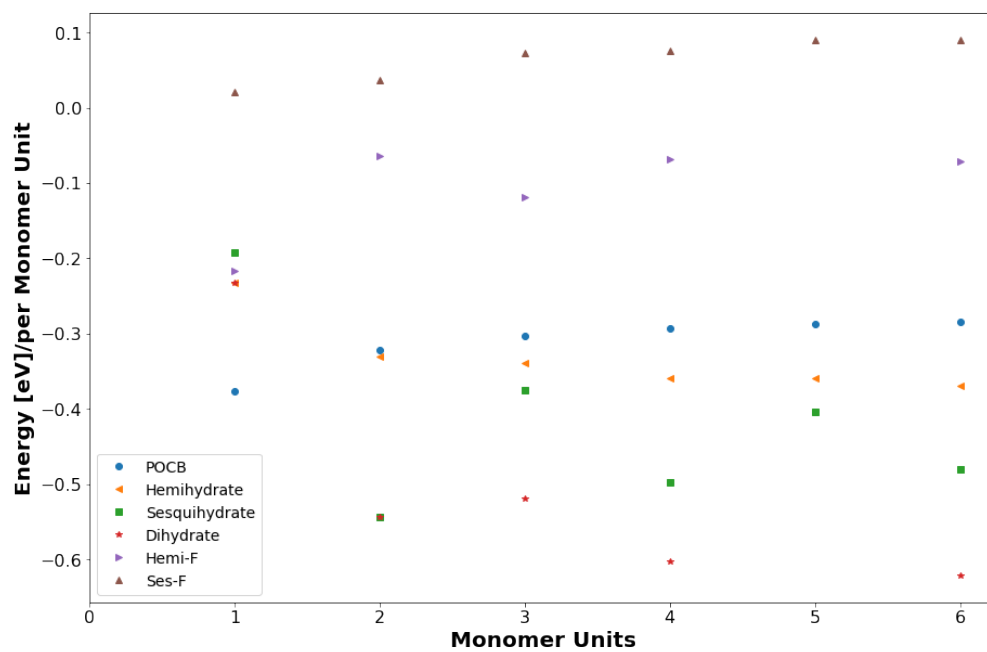
Figure 45: Binding Energies of all the hydrates as the number of monomer units increase for the Polymer-Water fragment
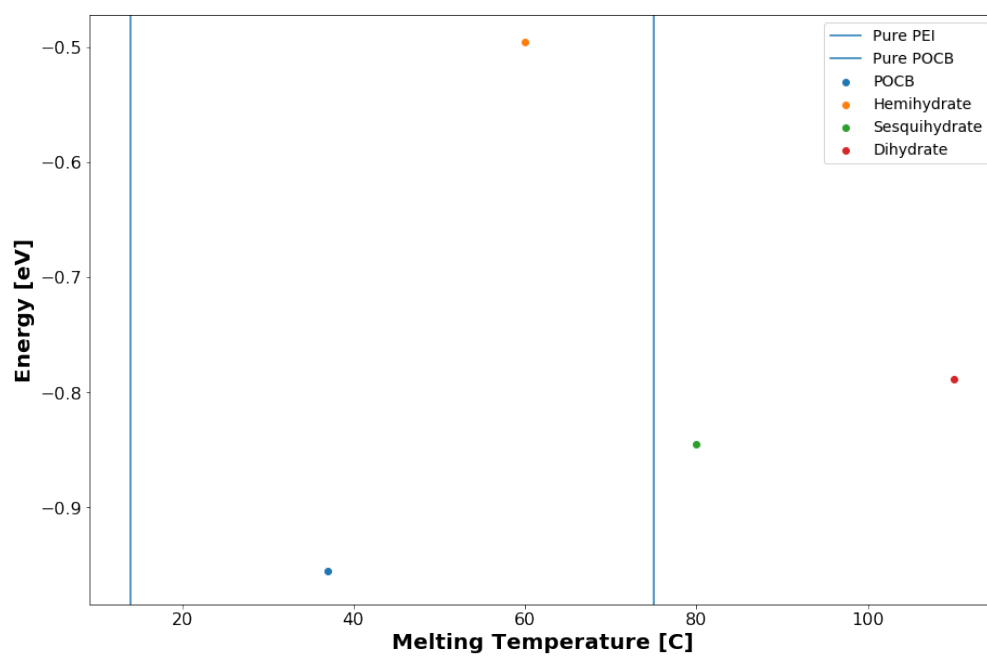
Figure 46: Total binding energies at the final polymer length compared to the experimental melting points

6.0 Conclusions

In this work polymer hydrates were investigated using a variety of computational techniques. Molecular dynamics models were used in attempt to model physical properties of these hydrates such as melting point. These models failed to predict the melting point due to their infinite size. As a result, a prototype tool to developed to provide better finite models.

Manual EDA was done with a variety of functionals for preliminary data to help guide LED simulations. The data between the three functionals was very similar, the biggest difference being the DLPNO data compared with the other two. All three functionals captured the same trends, with the actual energy values only differing slightly. When compared to the LED results, the numerical values and trends were also similar. Therefore, it can be concluded that the LED and manual EDA are in relative agreement, and the LED calculations can be trusted.

Local energy decomposition was done across four different hydrates in order to investigate the intermolecular forces that are allowing said hydrates to form. It was determined that the hydrates are being held together predominantly by electrostatic and exchange interactions. The electrostatic interactions are primarily hydrogen bonding, therefore the authors conclude that the dominant force allowing these systems to form is hydrogen bonding. When compared against one another, exchange interactions were always 1/5 the size of electrostatic interactions in all cases, which is a possible descriptor for other hydrates of this type.

Theoretical hydrates were constructed by doping in oxygen atoms or fluoridating the hemi and sesquihydrates. The oxygen doping made no significant difference to the intermolecular forces of the base hydrates. The fluoridation did cause changes to the structure of the hydrate, as well as significantly increasing the Polymer-Polymer interactions in the hemihydrate.

The binding energies of all the models was also calculated. A pattern between decreasing total binding energy correlated with increasing melting temperature, with the hemihydrate being an outlier. The oxygen doped PEI hemihydrate structure did not have a significantly different binding energy than their original counterpart, but the fluoridated structure demonstrated a much lower total binding energy. These binding energies suggest the existence of more hydrates, with the fluoridated structures particularly suggesting hydrates with a much higher melting point that may be able to handle ion capture.

Several possible paths forward are available for this work. First and foremost, more work should be done with consideration to atom replacements in polymer hydrates. Experimental work needs to be completed to test if the theoretical fluoridated polymers actually exist and are stable in nature. Other atom replacements should also be done on POCB and the PEI dihydrate as well to screen for more possible hydrates. Thermodynamic studies on these theoretical hydrates would also help better define the relationship between melting temperature and binding energy. Writing up the information in this thesis for publications is also a clear path. Outside of publications on the data gathered over the course of this work, a review article concerning hydrates of this type is a good way to remind the community about these unique and largely under-investigated substances, which is a necessity for the continued progress in this field.

Appendix A Structures

Table 12: Atomic coordinates of the POCB hydrate. O_W is the oxygen of the water molecule.

Atom	x/a	y/b	z/c
O	0.270	0.0	0.250
C_1	0.339	0.0	0.492
C_2	0.265	0.0	0.750
C_3	0.339	0.0	0.008
O_W	0.050	0.0	0.250

Table 13: Atomic coordinates of the PEI hemihydrate. O_W is the oxygen of the water molecule.

Atom	x/a	y/b	z/c
C_1	0.235	0.550	0.360
C_2	0.231	0.550	0.694
N	0.233	0.458	0.527
O_W	0.500	0.278	0.750

Table 14: Atomic coordinates of the PEI sesquihydrate. O_W is the oxygen of the water molecule.

Atom	x/a	y/b	z/c
C_1	0.210	-0.044	0.163
C_2	0.210	-0.044	0.491
N	0.210	0.041	0.327
O_W	0.036	0.374	0.577

Table 15: Atomic coordinates of the PEI dihydrate. O_W is the oxygen of the water molecule.

Atom	x/a	y/b	z/c
C	0.000	-0.095	0.086
N	0.000	0.086	0.250
O_W	0.215	0.276	0.319
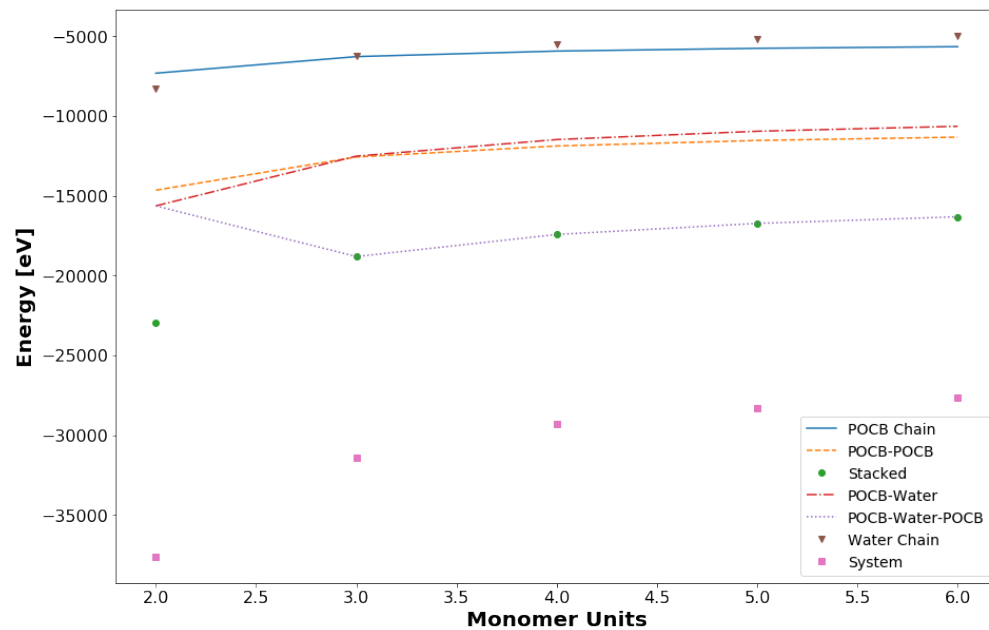
Figure 47: Single point energies of all structures as the number of monomer units increase using the ωB97X functional
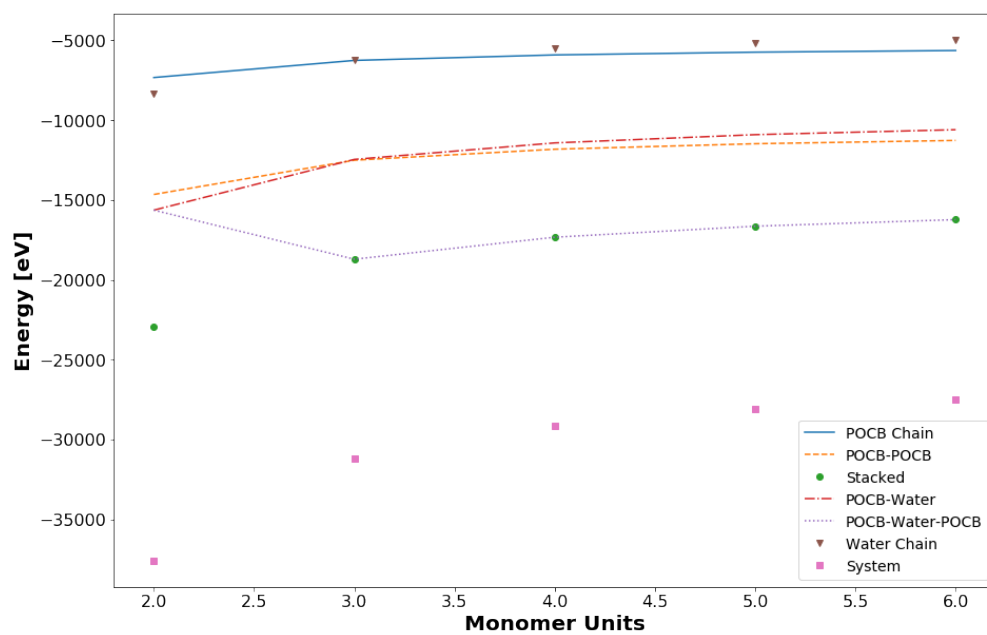
Figure 48: Single point energies of all structures as the number of monomer units increase using the DLPNO-CCSD(T) functional
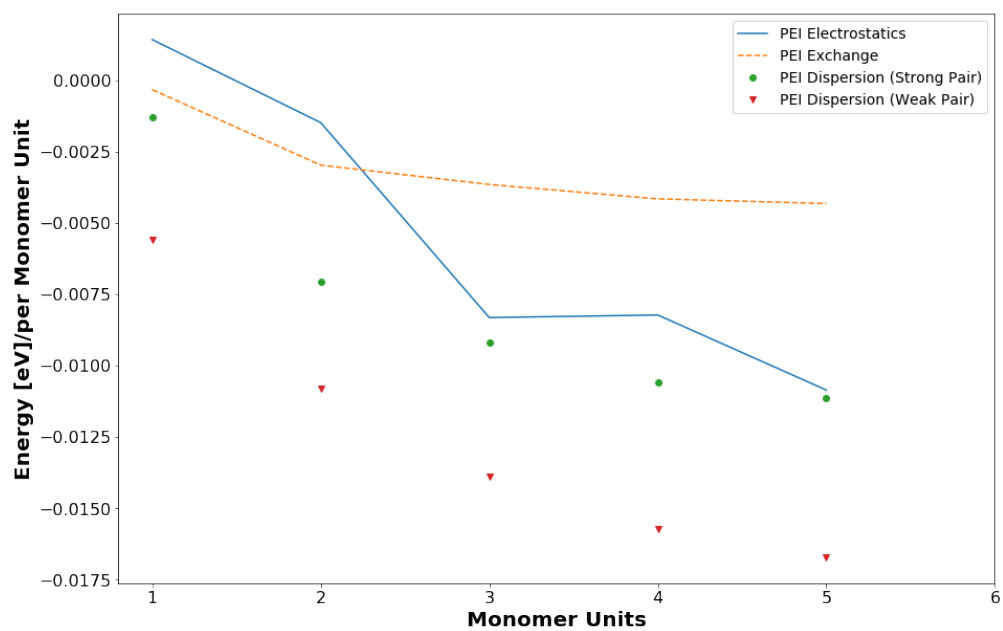
Figure 49: LED data of Polymer-Polymer interactions in the hemihydrate as the number of monomer units increase
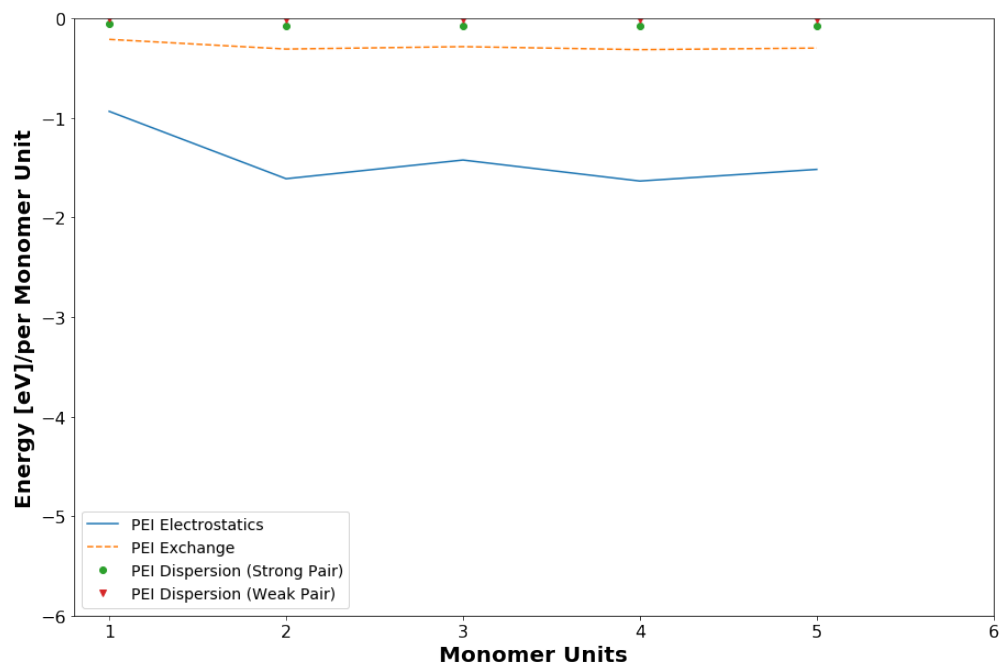
Figure 50: LED data of Water-Polymer interactions in the hemihydrate as the number of monomer units increase
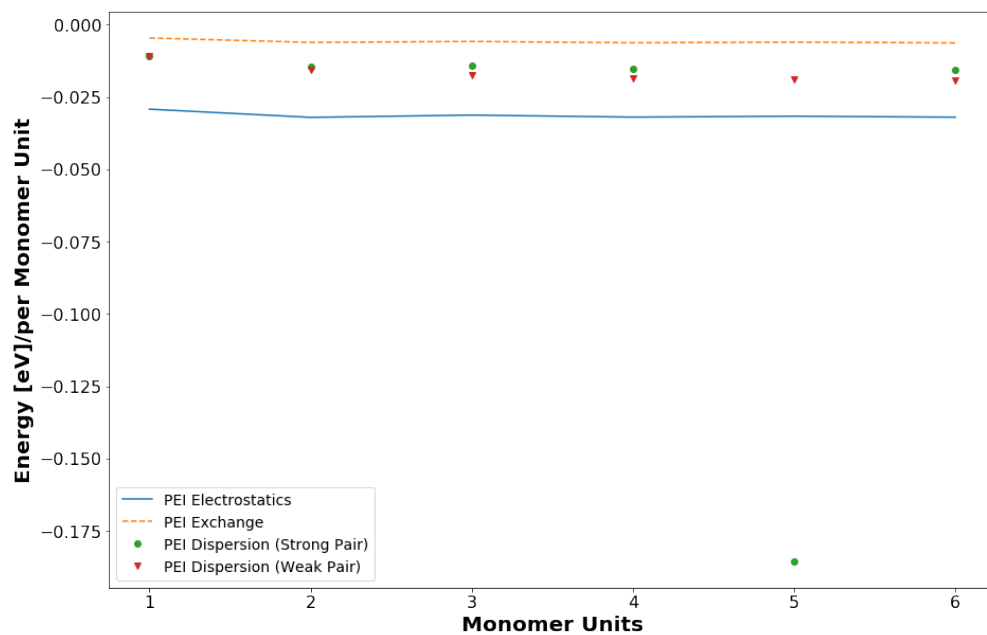
Figure 51: LED data of Polymer-Polymer interactions in the sesquihydrate as the number of monomer units increase
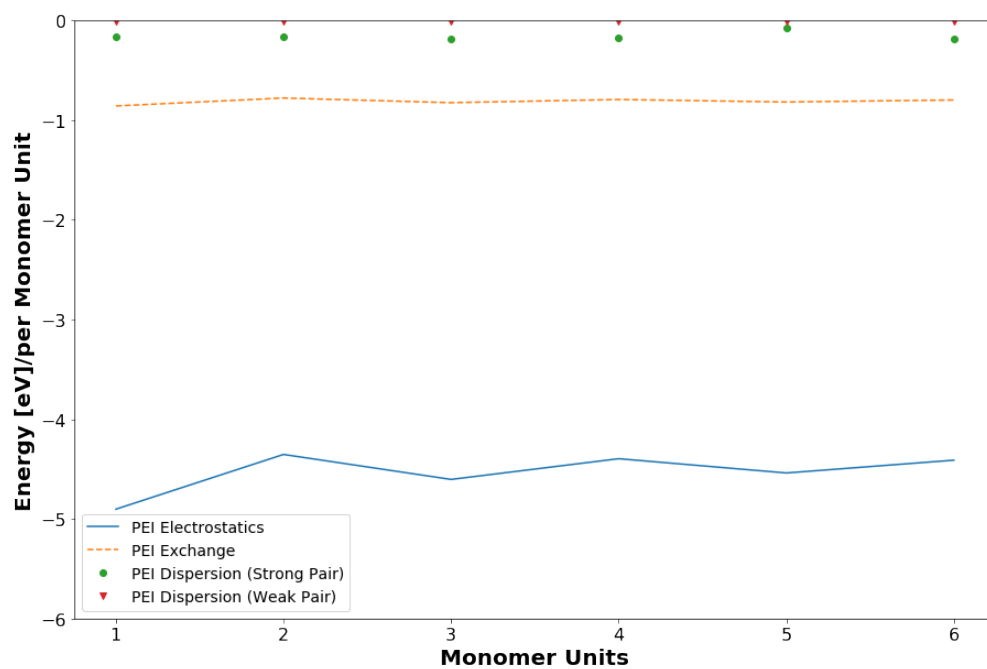
Figure 52: LED data of Water-Polymer interactions in the sesquihydrate as the number of monomer units increase
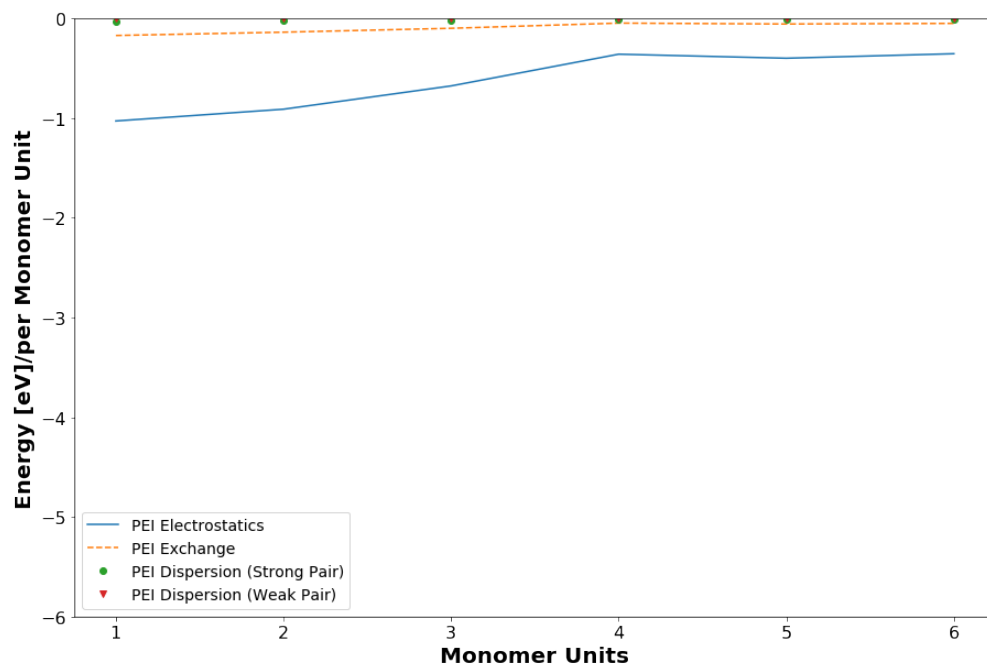
Figure 53: LED data of Water-Water interactions in the sesquihydrate as the number of monomer units increase
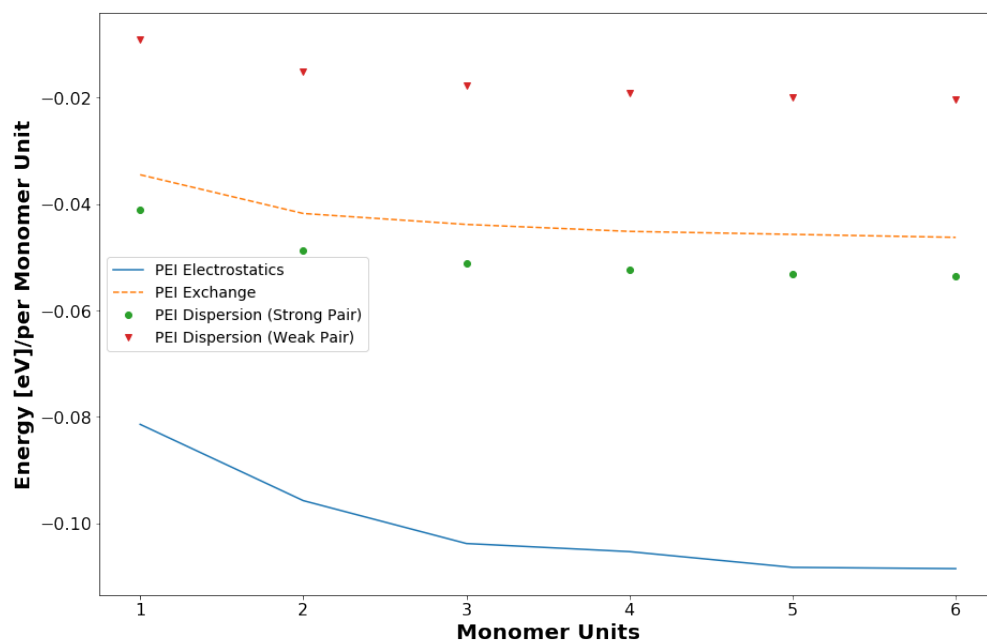
Figure 54: LED data of Polymer-Polymer interactions in the dihydrate as the number of monomer units increase
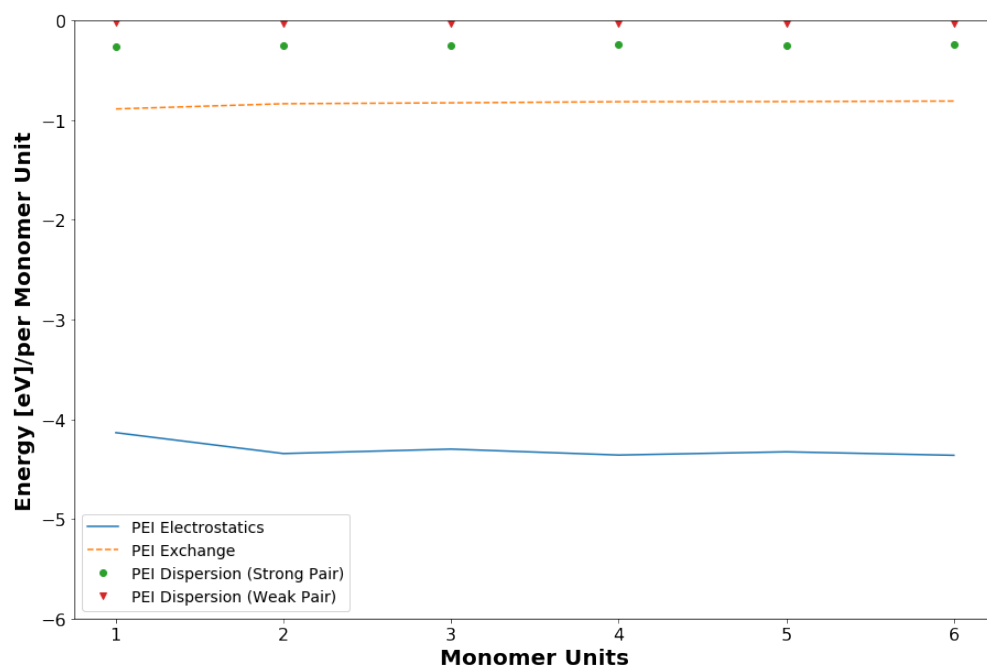
Figure 55: LED data of Water-Polymer interactions in the dihydrate as the number of monomer units increase
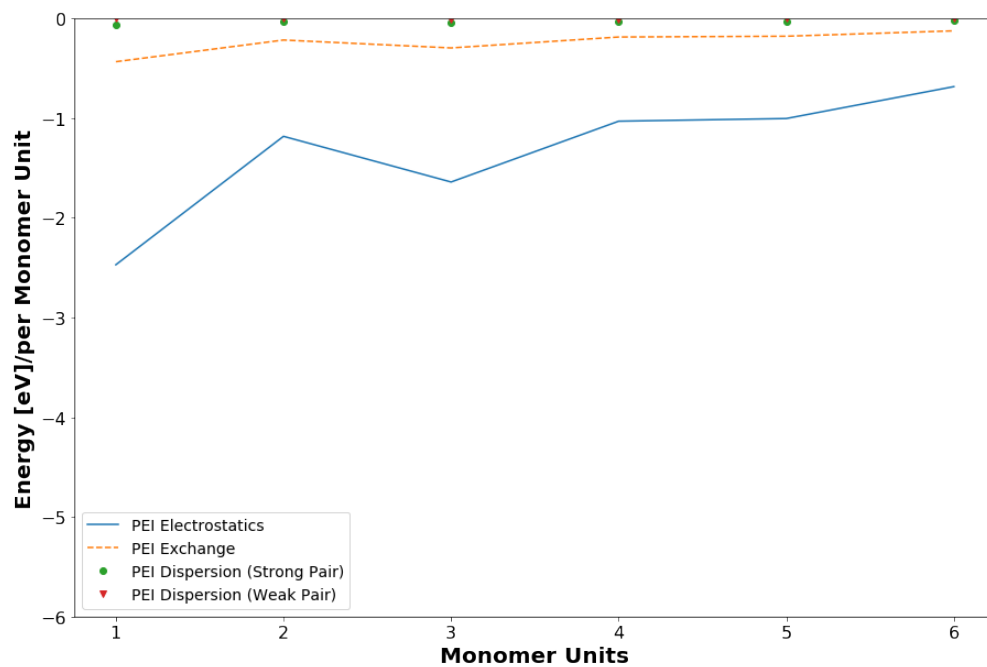
Figure 56: LED data of Water-Water interactions in the dihydrate as the number of monomer units increase

Appendix C Finite Polymer Code

```python
1  import numpy as np
2  import pandas as pd
3  import itertools
4  from random import randrange
5
6  df = pd.read_csv('POSCAR', delim_whitespace = True, skiprows = 8, names =
       ["X","Y","Z"])
7
8  with open("POSCAR") as file:
9      lines=[]
10     for line in file:
11         lines.append(line)
12     name = lines[0]
13     line2 = lines[1]
14     UnitCell1 = lines[2]
15     UnitCell2 = lines[3]
16     UnitCell3 = lines[4]
17     Atoms = lines[5]
18     AtomAmt = lines[6]
19     AtomAmt2 = np.array([int(i) for i in AtomAmt.split() if i.isdigit()])
20     Coords = lines[7]
21 file.close()
22
23 X = df["X"]
24 Y = df["Y"]
25 Z = df["Z"]
26
27 CC_BL = 1.53
28 CO_BL = 1.43
29 CH_BL = 1.09
30 OH_BL = 0.96
31
32 OCC_BA = 110
33
34 for i in range(len(X)):
35     Atom1 = np.array([X[0:AtomAmt2[0]], Y[0:AtomAmt2[0]], Z[0:AtomAmt2
       [0]]])
36     Atom2 = np.array([X[AtomAmt2[0]:AtomAmt2[0]+AtomAmt2[1]], Y[AtomAmt2
       [0]:AtomAmt2[0]+AtomAmt2[1]], Z[AtomAmt2[0]:AtomAmt2[0]+AtomAmt2[1]]])
37     Atom3 = np.array([X[(AtomAmt2[0]+AtomAmt2[1]):], Y[(AtomAmt2[0]+
       AtomAmt2[1]):], Z[(AtomAmt2[0]+AtomAmt2[1]):]])
38
39 Oxygen = Atom1[:,Atom1[2].argsort()]
40 Carbon = Atom2[:,Atom2[2].argsort()]
41 Hydrogen =  Atom3[:,Atom3[2].argsort()]
42
43
44 def FindBonds(Atom1, Atom1Name, Atom2, Atom2Name, BondType):
```

85

```
45      Bonded = []
46      for i in range(len(Atom1[0])):
47          for j in range(len(Atom2[0])):
48              Bond = np.array([Atom1[0,i], Atom1[1,i], Atom1[2,i]]) - np.
    array([Atom2[0,j], Atom2[1,j], Atom2[2,j]])
49              Bond = abs((Bond[0]**2 + Bond[1]**2 + Bond[2]**2)**(1/2))
50              Bond = float(str(round(Bond,4)))
51              #print(Bond)
52              if Bond <= BondType + 0.05 and Bond >= BondType - 0.05:
53              #if Bond == BondType:
54                  Bonded.append([Atom1Name,Atom1[0,i], Atom1[1,i], Atom1[2,i
    ]])
55                  Bonded.append([Atom2Name,Atom2[0,j], Atom2[1,j], Atom2[2,j
    ]])
56      return Bonded
57
58 CO_Bonds = FindBonds(Carbon, "Carbon", Oxygen, "Oxygen", CO_BL)
59 CC_Bonds = FindBonds(Carbon, "Carbon", Carbon, "Carbon", CC_BL)
60 CH_Bonds = FindBonds(Carbon, "Carbon", Hydrogen, "Hydrogen", CH_BL)
61 OH_Bonds = FindBonds(Oxygen, "Oxygen", Hydrogen, "Hydrogen", OH_BL)
62
63 def RemoveDupes(k):
64     new_k = []
65     for elem in k:
66         if elem not in new_k:
67             new_k.append(elem)
68     k = new_k
69     return k
70
71 CO_Bonds = RemoveDupes(CO_Bonds)
72 CC_Bonds = RemoveDupes(CC_Bonds)
73 CH_Bonds = RemoveDupes(CH_Bonds)
74 OH_Bonds = RemoveDupes(OH_Bonds)
75
76 def splitbyDistance(Bond, BondType, AtomName):
77     Atom1 = []
78     Atom2 = []
79     Break = []
80     Bond = np.array([list(i) for i in Bond])
81     #print(Bond)
82     for i in range(len(Bond)):
83         if Bond[i,0] == AtomName:
84             Atom1.append([Bond[i,0], Bond[i,1], Bond[i,2], Bond[i,3]])
85         else:
86             Atom2.append([Bond[i,0], Bond[i,1], Bond[i,2], Bond[i,3]])
87     #print(Atom1)
88     Atom1 = np.array([list(i) for i in Atom1])
89     Atom2 = np.array([list(i) for i in Atom2])
90     Atom = randrange(len(Atom1))
91     AtomSelect = np.array([Atom1[Atom,0], float(Atom1[Atom,1]), float(
    Atom1[Atom, 2]), float(Atom1[Atom, 3])])
92     for i in range(len(Atom2)):
93         Bonded = np.array([float(Atom2[i,1]), float(Atom2[i,2]), float(
    Atom2[i,3])]) - np.array([float(AtomSelect[1]), float(AtomSelect[2]),
```

```python
                float(AtomSelect[3])])
            Bonded = abs((Bonded[0]**2 + Bonded[1]**2 + Bonded[2]**2)**(1/2))
            Bonded = float(str(round(Bonded,4)))
            if Bonded <= BondType + 0.01 and Bonded >= BondType - 0.01:
                Break.append([Atom2[i,0], Atom2[i,1], Atom2[i,2], Atom2[i,3]])
        Break.append([AtomSelect[0], AtomSelect[1], AtomSelect[2], AtomSelect
    [3]])
    return Break


BrokenBonds = splitbyDistance(CO_Bonds, CO_BL, "Oxygen")
#print(BrokenBonds)

def findOtherBonds(Bond, Atom, BondType):
    Remove = []
    Bond = np.array([list(i) for i in Bond])
    Atom = np.array([list(i) for i in Atom])
    for i in range(len(Bond)):
        for j in range(len(Atom)):
            Bonded = np.array([float(Bond[i,1]), float(Bond[i,2]), float(
    Bond[i,3])]) - np.array([float(Atom[j,1]), float(Atom[j,2]), float(Atom
    [j,3])])
            Bonded = abs((Bonded[0]**2 + Bonded[1]**2 + Bonded[2]**2)
    **(1/2))
            Bonded = float(str(round(Bonded,4)))
            #print(Bonded)
            if Bonded <= BondType + 0.05 and Bonded >= BondType - 0.05:
                Remove.append([Atom[j,0], Atom[j,1], Atom[j,2], Atom[j
    ,3]])
        Remove.append([Bond[i,0], Bond[i,1], Bond[i,2], Bond[i,3]])
    return Remove


BrokenBonds = findOtherBonds(BrokenBonds, CC_Bonds, CC_BL)
BrokenBonds = findOtherBonds(BrokenBonds, CH_Bonds, CH_BL)

Break = np.array([list(i) for i in BrokenBonds])
#print(Break)
AtomsRemove = []
for i in range(len(Break)):
    if Break[i,0] == "Carbon" or Break[i,0] == "Hydrogen":
        if float(Break[i,3]) > float(Break[-1,3]):
            AtomsRemove.append([Break[i,0], Break[i,1], Break[i,2], Break[
    i,3]])


Broke = np.array([list(i) for i in AtomsRemove])
O_Count = 0
H_Count = 0
C_Count = 0
for i in range(len(Broke)):
    if Broke[i,0] == "Oxygen":
        O_Count += 1
    elif Broke[i,0] == "Hydrogen":
        if float(Broke[i,3]) > 1.5:
            H_Count += 1
```

```
141        elif Broke[i,0] == "Carbon":
142            if float(Broke[i,3]) > 1.5:
143                C_Count += 1
144
145 C_Replace = []
146 H_Replace = []
147 Broke = np.array([list(i) for i in Broke])
148 for i in range(len(Broke)):
149     if Broke[i,0] == "Carbon":
150         C_Replace.append([Broke[i,0], Broke[i,1], Broke[i,2], Broke[i,3]])
151     else:
152          H_Replace.append([Broke[i,0], Broke[i,1], Broke[i,2], Broke[i
    ,3]])
153
154 C_Replace = np.array([list(i) for i in C_Replace])
155 C_df = pd.DataFrame(C_Replace)
156 C_df.columns = ["element","X", "Y", "Z"]
157 C_df = C_df.sort_values(by = ['Z'])
158
159 H_Replace2 = C_df.iloc[:,1:]
160 H_Replace2 = H_Replace2.to_numpy()
161 H_Count -= 1
162 #print(H_Replace2)
163
164 #print(C_df)
165
166
167 H_Replace = [*H_Replace, *H_Replace2]
168 BrokenBonds = [*C_Replace, *H_Replace]
169
170 H_Replace2 = pd.DataFrame(H_Replace2)
171 H_Replace2.columns = ["X", "Y", "Z"]
172 print(BrokenBonds)
173
174 AtomAmt2 = np.array([int(AtomAmt2[0]), int(AtomAmt2[1]) - int(C_Count),
    int(AtomAmt2[2]) - int(H_Count)])
175
176
177 df_remove = pd.DataFrame(BrokenBonds)
178 #print(df_remove)
179 df_remove.columns = ["element","X", "Y", "Z"]
180 df_remove = df_remove.drop(df_remove.index[df_remove["element"] == "Oxygen
    "])
181 df_remove = df_remove.iloc[:,1:]
182 df_remove = df_remove.astype(float)
183 #df_remove = df_remove.sort_values(by = ['Z'])
184 #df_remove = df_remove.drop(df_remove[df_remove.Z < 1.5].index)
185
186
187
188
189 #print(df_remove)
190 #print(df)
191
```

```python
192 df3 = df.merge(df_remove, on=df.columns.tolist(), how='left', indicator=
        True)
193 df3 = df3[df3['_merge'] == 'left_only'].drop(columns='_merge')
194 df3 = df3.append(H_Replace2)
195
196 #print(df3)
197 dfAsString = df3.to_string(header=False, index=False)
198
199 with open("New_POSCAR","w") as f:
200     f.write(name )
201     f.write(line2 )
202     f.write(UnitCell1)
203     f.write(UnitCell2)
204     f.write(UnitCell3)
205     f.write(Atoms)
206     f.write("{} ".format(AtomAmt2[0]))
207     f.write("{} ".format(AtomAmt2[1]))
208     f.write("{}\n".format(AtomAmt2[2]))
209     f.write(Coords)
210     f.write(dfAsString)
211     f.close()
```

Bibliography

[1] Rana A. Fine and Frank J. Millero. Compressibility of water as a function of temperature and pressure. *J. Chem. Phys.*, 59(10):5529–5536, November 1973. Publisher: American Institute of Physics.

[2] Ralf Ludwig. Water: From Clusters to the Bulk. *Angewandte Chemie International Edition*, 40(10):1808–1827, 2001. _eprint: https://onlinelibrary.wiley.com/doi/pdf/10.1002/1521-3773%2820010518%2940%3A10%3C1808%3A%3AAID-ANIE1808%3E3.0.CO%3B2-1.

[3] Paul Loubeyre, René LeToullec, Elodie Wolanin, Michel Hanfland, and Daniel Hausermann. Modulated phases and proton centring in ice observed by X-ray diffraction up to 170?GPa. *Nature*, 397(6719):503–506, February 1999. Number: 6719 Publisher: Nature Publishing Group.

[4] Linus Pauling and Richard E. Marsh. The Structure of Chlorine Hydrate. *Proc. Natl. Acad. Sci. U.S.A.*, 38(2):112–118, February 1952.

[5] Bruce A. Buffett. Clathrate Hydrates. *Annual Review of Earth and Planetary Sciences*, 28(1):477–507, 2000. _eprint: https://doi.org/10.1146/annurev.earth.28.1.477.

[6] Subhadip Das, Kavya Mrudula Tadepalli, Sudip Roy, and Rajnish Kumar. A review of clathrate hydrate nucleation, growth and decomposition studied using molecular dynamics simulation. *Journal of Molecular Liquids*, 348:118025, February 2022.

[7] Andrzej Falenty, Thomas C. Hansen, and Werner F. Kuhs. Formation and properties of ice XVI obtained by emptying a type sII clathrate hydrate. *Nature*, 516(7530):231–233, December 2014.

[8] Satoshi Takeya, Akira Hori, Tsutomu Uchida, and Ryo Ohmura. Crystal Lattice Size and Stability of Type H Clathrate Hydrates with Various Large-Molecule Guest Substances. *J. Phys. Chem. B*, 110(26):12943–12947, July 2006. Publisher: American Chemical Society.

[9] Wendy L. Mao, Ho-kwang Mao, Alexander F. Goncharov, Viktor V. Struzhkin, Quanzhong Guo, Jingzhu Hu, Jinfu Shu, Russell J. Hemley, Maddury Somayazulu,

and Yusheng Zhao. Hydrogen Clusters in Clathrate Hydrate. *Science*, 297(5590):2247–2249, September 2002.

[10]   Werner F. Kuhs, Thomas C. Hansen, and Andrzej Falenty. Filling Ices with Helium and the Formation of Helium Clathrate Hydrate. *J. Phys. Chem. Lett.*, 9(12):3194–3198, June 2018. Publisher: American Chemical Society.

[11]   Jinlong Zhu, Shiyu Du, Xiaohui Yu, Jianzhong Zhang, Hongwu Xu, Sven C. Vogel, Timothy C. Germann, Joseph S. Francisco, Fujio Izumi, Koichi Momma, Yukihiko Kawamura, Changqing Jin, and Yusheng Zhao. Encapsulation kinetics and dynamics of carbon monoxide in clathrate hydrate. *Nat Commun*, 5(1):4128, September 2014.

[12]   Bertrand Chazallon and Werner F. Kuhs. *In situ* structural properties of N2-, O2-, and air-clathrates by neutron diffraction. *The Journal of Chemical Physics*, 117(1):308–320, July 2002.

[13]   Ray Boswell and Timothy S. Collett. Current perspectives on gas hydrate resources. *Energy Environ. Sci.*, 4(4):1206–1215, March 2011. Publisher: The Royal Society of Chemistry.

[14]   Keith   A.   Kvenvolden.   Methane   hydrates   and   global   climate.   *Global   Biogeochemical   Cycles*,   2(3):221–229,   1988.   _eprint: https://onlinelibrary.wiley.com/doi/pdf/10.1029/GB002i003p00221.

[15]   Guang-Jun Guo, Yi-Gang Zhang, and Hua Liu. Effect of Methane Adsorption on the Lifetime of a Dodecahedral Water Cluster Immersed in Liquid Water: A Molecular Dynamics Study on the Hydrate Nucleation Mechanisms. *J. Phys. Chem. C*, 111(6):2595–2606, February 2007. Publisher: American Chemical Society.

[16]   Keith A. Kvenvolden. A review of the geochemistry of methane in natural gas hydrate. *Organic Geochemistry*, 23(11):997–1008, November 1995.

[17]   Carolyn D. Ruppel and John D. Kessler.   The interaction of climate change and methane hydrates.   *Reviews of Geophysics*, 55(1):126–168, 2017.   _eprint: https://onlinelibrary.wiley.com/doi/pdf/10.1002/2016RG000534.

[18]   John Bohannon. Weighing the Climate Risks of an Untapped Fossil Fuel. *Science*, 319(5871):1753–1753, March 2008. Publisher: American Association for the Advancement of Science.

[19]   Gordon J. MacDonald. Role of methane clathrates in past and future climates. *Climatic Change*, 16(3):247–281, June 1990.

[20]   Gail Whiteman, Chris Hope, and Peter Wadhams. Vast costs of Arctic change. *Nature*, 499(7459):401–403, July 2013. Number: 7459 Publisher: Nature Publishing Group.

[21]   Yu-Taek Seo, Huen Lee, and Ji-Ho Yoon. Hydrate Phase Equilibria of the Carbon Dioxide, Methane, and Water System. *J. Chem. Eng. Data*, 46(2):381–384, March 2001. Publisher: American Chemical Society.

[22]   Gerald D. Holder, Anthony V. Cugini, and Robert P. Warzinski. Modeling Clathrate Hydrate Formation during Carbon Dioxide Injection into the Ocean. *Environ. Sci. Technol.*, 29(1):276–278, January 1995. Publisher: American Chemical Society.

[23]   D. W. Davidson. Clathrate Hydrates. In Felix Franks, editor, *Water in Crystalline Hydrates Aqueous Solutions of Simple Nonelectrolytes*, Water, pages 115–234. Springer US, Boston, MA, 1973.

[24]   Jón S Gudmundsson and Oscar F Graff. HYDRATE NON-PIPELINE TECHNOLOGY FOR TRANSPORT OF NATURAL GAS. page 5.

[25]   S. Bachu and J. J. Adams. Sequestration of CO2 in geological media in response to climate change: capacity of deep saline aquifers to sequester CO2 in solution. *Energy Conversion and Management*, 44(20):3151–3175, December 2003.

[26]   R. Kojima, K. Yamane, and I. Aya. - Dual Nature of CO2 Solubility in Hydrate Forming Region. In J. Gale and Y. Kaya, editors, *Greenhouse Gas Control Technologies - 6th International Conference*, pages 825–830. Pergamon, Oxford, January 2003.

[27]   C. R. Liro, E. E. Adams, and H. J. Herzog. Modeling the release of CO2 in the deep ocean. *Energy Conversion and Management*, 33(5):667–674, May 1992.

[28]   Sangyong Lee, Liyuan Liang, David Riestenberg, Olivia R. West, Costas Tsouris, and Eric Adams. CO2 hydrate composite for ocean carbon sequestration. *Environ Sci Technol*, 37(16):3701–3708, August 2003.

[29]   Imen Chatti, Anthony Delahaye, Laurence Fournaison, and Jean-Pierre Petitet. Benefits and drawbacks of clathrate hydrates: a review of their areas of interest. *Energy Conversion and Management*, 46(9):1333–1343, June 2005.

[30]   C. W. Bunn and D. R. Holmes. Chain configurations in crystals of simple linear polymers. *Discuss. Faraday Soc.*, 25(0):95–103, January 1958. Publisher: The Royal Society of Chemistry.

[31]   Hiroyuki Tadokoro, Yasuhiro Takahashi, Yôzô Chatani, and Hideto Kakida. Structural studies of polyethers, [(CH2)mO]n. V. Polyoxacyclobutane. *Die Makromolekulare Chemie*, 109(1):96–111, 1967. _eprint: https://onlinelibrary.wiley.com/doi/pdf/10.1002/macp.1967.021090110.

[32]   Hiroyuki Tadokoro. Structure of crystalline polyethers. *Journal of Polymer Science: Macromolecular Reviews*, 1(1):119–172, 1967. _eprint: https://onlinelibrary.wiley.com/doi/pdf/10.1002/pol.1967.230010105.

[33]   Shohei YosmnA, Minoru Sakiyama, and Syfizo Seki. Thermodynamic Studies of Solid Polyethers. I. Poly(Oxacyclobutane), [-(CH2) 30-]n and Its Hydrate. 1(5):9, 1970.

[34]   Joyita Banerjee, Peter Koronaios, Brittni Morganstein, Steven J. Geib, Robert M. Enick, John A. Keith, Eric J. Beckman, and Sachin S. Velankar. Liquids That Freeze When Mixed: Cocrystallization and Liquid–Liquid Equilibrium in Polyoxacyclobutane–Water Mixtures. *Macromolecules*, 51(8):3176–3183, April 2018.

[35]   Hideto Kakida and Hiroyuki Tadokorolb. Structural Studies of Polyethers [-(CH,)mO-jH. VIII. 3(5):10, 1970.

[36]   D S Zhuk, Petr A Gembitskii, and Valentin A Kargin. ADVANCES IN THE CHEMISTRY OF POLYETHYLENEIMINE (POLYAZIRIDINE). *Russ. Chem. Rev.*, 34(7):515–527, July 1965.

[37]   P. A. Gembitskii, A. I. Chmarin, N. A. Kleshcheva, and D. S. Zhuk. The polymerization of ethylenimine to give linear polyethylenimine. *Polymer Science U.S.S.R.*, 20(7):1695–1702, January 1978.

[38]   Ryuichi Tanaka, Isao Ueoka, Yasuhiro Takaki, Kazuya Kataoka, and Shogo Saito. High molecular weight linear polyethylenimine and poly(N-methylethylenimine). *Macromolecules*, 16(6):849–853, June 1983.

[39]   Yozo Chatani, Takushi Kobatake, and Hiroyuki Tadokoro. Structural studies of poly(ethylenimine). 3. Structural characterization of anhydrous and hydrous states and crystal structure of the hemihydrate. *Macromolecules*, 16(2):199–204, February 1983.

[40] Yozo Chatani, Hiroyuki Tadokoro, Takeo Saegusa, and Hiroharu Ikeda. Structural studies of poly(ethylenimine). 1. Structures of two hydrates of poly(ethylenimine): sesquihydrate and dihydrate. *Macromolecules*, 14(2):315–321, March 1981. Publisher: American Chemical Society.

[41] Tomoko Hashida, Kohji Tashiro, and Yoshiaki Inaki. Structural investigation of water-induced phase transitions of poly(ethylene imine). III. The thermal behavior of hydrates and the construction of a phase diagram. *Journal of Polymer Science Part B: Polymer Physics*, 41(22):2937–2948, 2003. _eprint: https://onlinelibrary.wiley.com/doi/pdf/10.1002/polb.10611.

[42] Linqiang Wu, Tao Zhang, Hongtao Zhang, Yuzhang Sui, Xinghe Yu, and Miao Miao. Economic evaluation of production capacity for natural gas hydrate industrial exploitation in the South China Sea. *Frontiers in Earth Science*, 10, 2022.

[43] Takashi Yamamoto. Molecular dynamics modeling of polymer crystallization from the melt. *Polymer*, 45(4):1357–1364, February 2004.

[44] Ali Gooneie, Stephan Schuschnigg, and Clemens Holzer. A Review of Multiscale Computational Methods in Polymeric Materials. *Polymers (Basel)*, 9(1):16, January 2017.

[45] Thomas E. Gartner and Arthi Jayaraman. Modeling and Simulations of Polymers: A Roadmap. *Macromolecules*, 52(3):755–786, February 2019. Publisher: American Chemical Society.

[46] Y. Mori, A. Yoshimura, T. Ukai, E. Lien, T. Espevik, and Y. Hara. Immunohistochemical localization of Toll-like receptors 2 and 4 in gingival tissue from patients with periodontitis. *Oral Microbiology and Immunology*, 18(1):54–58, 2003. _eprint: https://onlinelibrary.wiley.com/doi/pdf/10.1034/j.1399-302X.2003.180109.x.

[47] Wendy L. Mao and Ho-kwang Mao. Hydrogen storage in molecular compounds. *Proc Natl Acad Sci U S A*, 101(3):708–710, January 2004.

[48] Peter G. Brewer, Gernot Friederich, Edward T. Peltzer, and Franklin M. Orr. Direct Experiments on the Ocean Disposal of Fossil Fuel CO2. *Science*, 284(5416):943–945, May 1999. Publisher: American Association for the Advancement of Science.

[49]   Takuya Suginaka, Hiroki Sakamoto, Kento Iino, Satoshi Takeya, Masahiro Nakajima, and Ryo Ohmura. Thermodynamic properties of ionic semiclathrate hydrate formed with tetrabutylphosphonium bromide. *Fluid Phase Equilibria*, 317:25–28, March 2012.

[50]   Yen-Tien Tung, Li-Jen Chen, Yan-Ping Chen, and Shiang-Tai Lin. The Growth of Structure I Methane Hydrate from Molecular Dynamics Simulations. *J. Phys. Chem. B*, 114(33):10804–10813, August 2010. Publisher: American Chemical Society.

[51]   Byeong Soo Shin, Eun Sung Kim, Sang Kyu Kwak, Jong Sung Lim, Ki-Sub Kim, and Jeong Won Kang. Thermodynamic inhibition effects of ionic liquids on the formation of condensed carbon dioxide hydrate. *Fluid Phase Equilibria*, 382:270–278, November 2014.

[52]   Parisa Naeiji, Tom K. Woo, Saman Alavi, and John A. Ripmeester. Molecular Dynamic Simulations of Clathrate Hydrate Anomalous Preservation: The Effect of Coating Clathrate Hydrate Phases. *J. Phys. Chem. C*, 123(47):28715–28725, November 2019. Publisher: American Chemical Society.

[53]   Soowon Cho, Sohdam Jeong, Jun Mo Kim, and Chunggi Baig. Molecular dynamics for linear polymer melts in bulk and confined systems under shear flow. *Sci Rep*, 7(1):9004, August 2017. Number: 1 Publisher: Nature Publishing Group.

[54]   Junmei Wang, Romain M. Wolf, James W. Caldwell, Peter A. Kollman, and David A. Case. Development and testing of a general amber force field. *Journal of Computational Chemistry*, 25(9):1157–1174, 2004. _eprint: https://onlinelibrary.wiley.com/doi/pdf/10.1002/jcc.20035.

[55]   Stephen L. Mayo, Barry D. Olafson, and William A. Goddard. DREIDING: a generic force field for molecular simulations. *J. Phys. Chem.*, 94(26):8897–8909, December 1990. Publisher: American Chemical Society.

[56]   Shalini J. Rukmani, Grit Kupgan, Dylan M. Anstine, and Coray M. Colina. A molecular dynamics study of water-soluble polymers: analysis of force fields from atomistic simulations. *Molecular Simulation*, 45(4-5):310–321, March 2019.

[57]   Aidan P. Thompson, H. Metin Aktulga, Richard Berger, Dan S. Bolintineanu, W. Michael Brown, Paul S. Crozier, Pieter J. in 't Veld, Axel Kohlmeyer, Stan G. Moore, Trung Dac Nguyen, Ray Shan, Mark J. Stevens, Julien Tranchida, Christian Trott, and Steven J. Plimpton. LAMMPS - a flexible simulation tool for particle-based materials modeling at the atomic, meso, and continuum scales. *Computer Physics Communications*, 271:108171, February 2022.

[58] Ole Kr. Forrisdahl. Methane clathrate hydrates: melting, supercooling and phase separation from molecular dynamics computer simulations. *Molecular Physics*, 89(3):819–834, October 1996.

[59] Yozo Chatani, Takushi Kobatake, Hiroyuki Tadokoro, and Ryuichi Tanaka. Structural studies of poly(ethylenimine). 2. Double-stranded helical chains in the anhydrate. *Macromolecules*, 15(1):170–176, January 1982.

[60] Maija M. Kuklja, Frank J. Zerilli, and Peter Sushko. Embedded Cluster Model: Application to Molecular Crystals. *MRS Online Proceedings Library*, 800(1):15–26, December 2003.

[61] Kun V. Tian, Mustafa Z. Mahmoud, Paola Cozza, Silvia Licoccia, De-Cai Fang, Devis Di Tommaso, Gregory A. Chass, and G. Neville Greaves. Periodic vs. molecular cluster approaches to resolving glass structure and properties: Anorthite a case study. *Journal of Non-Crystalline Solids*, 451:138–145, November 2016.

[62] Keiji Morokuma. Molecular Orbital Studies of Hydrogen Bonds. III. C=O···H–O Hydrogen Bond in H2CO···H2O and H2CO···2H2O. *J. Chem. Phys.*, 55(3):1236–1244, August 1971. Publisher: American Institute of Physics.

[63] Tom Ziegler and Arvi Rauk. On the calculation of bonding energies by the Hartree Fock Slater method. *Theoret. Chim. Acta*, 46(1):1–10, October 1977.

[64] Lili Zhao, Moritz von Hopffgarten, Diego M. Andrada, and Gernot Frenking. Energy decomposition analysis. *WIREs Computational Molecular Science*, 8(3):e1345, 2018. _eprint: https://wires.onlinelibrary.wiley.com/doi/pdf/10.1002/wcms.1345.

[65] Rustam Z. Khaliullin, Erika A. Cobar, Rohini C. Lochan, Alexis T. Bell, and Martin Head-Gordon. Unravelling the Origin of Intermolecular Interactions Using Absolutely Localized Molecular Orbitals. *J. Phys. Chem. A*, 111(36):8753–8765, September 2007.

[66] Bogumil Jeziorski, Robert Moszynski, and Krzysztof Szalewicz. Perturbation Theory Approach to Intermolecular Potential Energy Surfaces of van der Waals Complexes. *Chem. Rev.*, 94(7):1887–1930, November 1994. Publisher: American Chemical Society.

[67] Olga A. Stasyuk, Robert Sedlak, Célia Fonseca Guerra, and Pavel Hobza. Comparison of the DFT-SAPT and Canonical EDA Schemes for the Energy Decomposition of Various Types of Noncovalent Interactions. *J. Chem. Theory Comput.*, 14(7):3440–3450, July 2018.

[68] Narbe Mardirossian and Martin Head-Gordon. Thirty years of density functional theory in computational chemistry: an overview and extensive assessment of 200 density functionals. *Molecular Physics*, 115(19):2315–2372, October 2017. Publisher: Taylor & Francis _eprint: https://doi.org/10.1080/00268976.2017.1333644.

[69] Jeng-Da Chai and Martin Head-Gordon. Systematic optimization of long-range corrected hybrid density functionals. *The Journal of Chemical Physics*, 128(8):084106, February 2008.

[70] Dimitrios G. Liakos, Manuel Sparta, Manoj K. Kesharwani, Jan M. L. Martin, and Frank Neese. Exploring the Accuracy Limits of Local Pair Natural Orbital Coupled-Cluster Theory. *J. Chem. Theory Comput.*, 11(4):1525–1539, April 2015. Publisher: American Chemical Society.

[71] Wolfgang B. Schneider, Giovanni Bistoni, Manuel Sparta, Masaaki Saitow, Christoph Riplinger, Alexander A. Auer, and Frank Neese. Decomposition of Intermolecular Interaction Energies within the Local Pair Natural Orbital Coupled Cluster Framework. *J. Chem. Theory Comput.*, 12(10):4778–4792, October 2016.

[72] Ahmet Altun, Masaaki Saitow, Frank Neese, and Giovanni Bistoni. Local Energy Decomposition of Open-Shell Molecular Systems in the Domain-Based Local Pair Natural Orbital Coupled Cluster Framework. *J. Chem. Theory Comput.*, 15(3):1616–1632, March 2019.